



Title	Concentration and Brightness Imaging for Fluorescent Molecules in Cells: Statistical Image Analysis by Empirical Bayes Method
Author(s)	福島, 綾介
Citation	北海道大学. 博士(生命科学) 甲第14607号
Issue Date	2021-06-30
DOI	10.14943/doctoral.k14607
Doc URL	http://hdl.handle.net/2115/86421
Type	theses (doctoral)
File Information	Ryosuke_Fukushima.pdf



[Instructions for use](#)

Doctoral Dissertation

**Concentration and Brightness Imaging
for Fluorescent Molecules in Cells:
Statistical Image Analysis by Empirical Bayes Method**

(細胞内蛍光分子の濃度と輝度分布定量：
経験ベイズ法による統計的画像解析)

Ryosuke Fukushima

Graduate School of Life Science, Hokkaido University

2021 June

ABSTRACT

Background: Fluorescence live cell imaging is useful for monitoring the localization and distribution of fluorescently labeled molecules in cells. However, monitoring the concentration and oligomeric state of these molecules is difficult. The concentration of molecules is strongly associated with the advancement of chemical reactions in cells, and these reactions regulate cellular functions. Furthermore, some proteins form oligomers during cell signaling, changing their oligomeric state. Thus, quantifying the concentration and oligomeric state would yield valuable information about the regulations and functions of cells. In this study, we have developed statistical methods for quantifying the concentration and oligomeric state of fluorescently labeled molecules in cells.

Problem and Solutions: Number and Brightness (N&B) analysis statistically determines the number and brightness of particles, which reflect the concentration and oligomeric state, respectively. N&B analysis is used to analyze the temporal fluctuation of fluorescence images obtained using confocal laser scanning microscopy (CLSM). However, because of low excitation and a limited number of images, the statistical accuracy and precision of this analysis are limited in actual experiments with fluorescent proteins. In one of our methods, we applied maximum a posteriori (MAP) estimation, along with the empirical Bayes (EB) method (referred to as EB-MAP). In EB-MAP, we constructed a statistical model for effectively using spatial information. We assumed that the number of particles at a pixel and that at the surrounding pixels are similar. The assumption of the similarity would be realistic because of the diffraction limit and overlap of confocal volume during sampling.

Results: We conducted simulations and experiments and compared results to evaluate the accuracy and precision of EB-MAP. The results showed that the precision of EB-MAP was greater by an order of magnitude in terms of the number of particles and 1.5 times higher in terms of the brightness of particles than conventional N&B analysis.

Conclusion: We have developed methods for monitoring the concentration and oligomeric state of fluorescently labeled molecules in cells. We have demonstrated that the developed methods are feasible and achieve high accuracy and precision. Our methods have a wide range of applications in the field of fluorescence live cell imaging. Furthermore, these methods would contribute to the understanding of the dynamic processes in protein oligomerization in cells.

LIST OF SCIENTIFIC PAPERS

Papers (Related to Doctoral Dissertation)

- I. **R. Fukushima**, J. Yamamoto, H. Ishikawa, M. Kinjo, Two-detector number and brightness analysis reveals spatio-temporal oligomerization of proteins in living cells, *Methods*. 140–141 (2018) 161–171. <https://doi.org/10.1016/j.ymeth.2018.03.007>.
- II. **R. Fukushima**, J. Yamamoto, M. Kinjo, Number and Brightness Analysis: Visualization of Protein Oligomeric State in Living Cells, in: Kim J.K., Kim J.K., Pack CG. (eds) *Advanced Imaging and Bio Techniques for Convergence Science. Advances in Experimental Medicine and Biology*, vol 1310. Springer, Singapore. (2021): pp. 31–58. https://doi.org/10.1007/978-981-33-6064-8_2.
- III. **R. Fukushima**, J. Yamamoto, M. Kinjo, Empirical Bayes Method Using Surrounding Pixel Information for Number and Brightness Analysis, *Biophys. J.* 120 (2021) 1–16. <https://doi.org/10.1016/j.bpj.2021.03.033>.

Papers (Other than the above)

M. Oura, J. Yamamoto, H. Ishikawa, S. Mikuni, **R. Fukushima**, M. Kinjo, Polarization-dependent fluorescence correlation spectroscopy for studying structural properties of proteins in living cell, *Sci. Rep.* 6 (2016) 31091. <https://doi.org/10.1038/srep31091>.

CONTENTS

Chapter 1 General Introduction.....	1
1.1 Why Quantifying Concentration in Living Cells Is Required.....	1
1.2 Quantifying Concentration Using Fluorescence Live Cell Imaging.....	1
1.3 Monitoring Oligomeric State by N&B Analysis.....	3
1.4 Basic Theory for N&B Analysis.....	3
1.5 References.....	5
Chapter 2 Problems in N&B Analysis and Solutions Provided by This Research.....	7
2.1 Organization of the Doctoral Dissertation.....	7
2.2 References.....	8
Chapter 3 Prerequisites for Quantitative N&B Analysis.....	9
3.1 Abstract.....	9
3.2 Introduction.....	9
3.2.1 Protein Oligomer.....	9
3.2.2 Fluorescence Fluctuation Spectroscopy (FFS).....	9
3.2.3 Brightness Analysis.....	11
3.2.4 Introduction for Number and Brightness Analysis.....	12
3.2.5 Organization of the article.....	12
3.3 Number and Brightness (N&B) Analysis.....	13
3.4 Notation used in N&B analysis.....	14
3.4.1 Optimal Sampling Time and Lag Time.....	15
3.4.2 Additional Photon Counts and Signal Fluctuations.....	16
3.4.3 Frame Number.....	20
3.4.4 Non-fluorescent State of Fluorescent Proteins.....	23
3.5 Comparison with other techniques.....	25
3.6 Software.....	26
3.7 Simulations.....	26
3.8 Conclusion.....	26
3.9 Supplementary Information 1.....	27
3.10 Supplementary Information 2.....	29
3.11 References.....	31

Chapter 4	Reduction of Dead Time Effect by Estimating Covariance	37
4.1	Abstract	37
4.2	Introduction	37
4.3	Methods	39
4.3.1	Two-detector number and brightness analysis (TD-N&B)	39
4.3.2	Simulation	43
4.3.3	Purification of EGFP	44
4.3.4	Preparation of EGFP tandem oligomer lysate	44
4.3.5	Preparation of EGFP tandem oligomer-transfected U2OS cells	44
4.3.6	Measurement of EGFP-GR translocation	44
4.3.7	Image acquisition for TD-N&B	45
4.3.8	FCS measurements	45
4.3.9	Analysis conditions	46
4.4	Results	47
4.4.1	Comparison by simulation	47
4.4.2	TD-N&B in solution	48
4.4.3	In vitro investigation of EGFP tandem oligomers using TD-N&B	48
4.4.4	Investigation of EGFP tandem oligomers in live cells	51
4.4.5	GR measurement	51
4.5	Discussion	53
4.6	Conclusion	55
4.7	References	55
4.8	Supplemental Information 1	58
4.9	Supplemental Information 2	61
4.10	Supplemental Information 3	62
Chapter 5	Application of ML and MAP Estimation Along With EB Method	63
5.1	Abstract	63
5.2	Introduction	63
5.3	Methods	66
5.3.1	Photon-counting model	66
5.3.2	Maximum likelihood estimation	69
5.3.3	Maximum a posteriori estimation	73
5.3.4	Empirical Bayes Method	75
5.4	Results	78
5.4.1	Comparison of different concentrations by simulation	78

5.4.2 Comparison of different laser powers or oligomeric states by simulation.....	80
5.4.3 Experimental comparison of different concentrations	82
5.4.4 Experimental comparison of different laser powers.....	83
5.4.5 Experimental comparison of EGFP tandem oligomers	85
5.5 Discussion.....	85
5.6 Conclusion	89
5.7 References.....	89
5.8 Supplemental Information	94
5.8.1 Theoretical derivations.....	95
5.8.2 Materials and methods	101
5.8.3 Supplemental data.....	106
Chapter 6 Conclusions and Future Perspectives	141

Chapter 1

General Introduction

1.1 Why Quantifying Concentration in Living Cells Is Required

In living cells, various chemical reactions occur through the interaction between molecules, maintaining cell activities. Characterizing chemical reactions in cells would contribute to the understanding of regulation in cell activities. Quantifying the concentrations of reactants and products during the chemical equilibrium of a chemical reaction characterizes the chemical reaction using an equilibrium constant. The equilibrium constant is a numerical value that depends on the temperature and chemical species of a reaction rather than the concentration. A high equilibrium constant indicates that a reaction proceeds smoothly and produces more products. Quantifying the concentration and equilibrium constant reveals how much a chemical reaction is downregulated or upregulated. Although the equilibrium constant can be quantified through experiments in a mixed solution (*in vitro* experiment), experiments in living cells (*in vivo* experiment) would yield more detailed information. This is because of competitive inhibition and macromolecular crowding. During competitive inhibition of a chemical reaction in living cells, other chemical species of interest may interrupt the reaction, reducing the equilibrium constant of the reaction. Macromolecular crowding increases the effective concentration locally because of the excluded volume effect. Therefore, quantifying the concentration in living cells is required. Moreover, the spatial distribution of concentration should be obtained. This is because the cell environment is spatially heterogeneous. Cells have many organelles partitioned by membranes, and organelles make the environment spatially heterogeneous. Macromolecular crowding also contributes to heterogeneity.

1.2 Quantifying Concentration Using Fluorescence Live Cell Imaging

Fluorescence live cell imaging is a highly sensitive tool for detecting fluorescently labeled molecules in living cells, and it is useful for monitoring the dynamic changes of these molecules in localization and distribution. Fluorescence microscopy quantifies the fluorescence emitted in measurement volume as fluorescence intensity. Absolute quantification of concentration could be achieved by single-molecule imaging. Single-molecule imaging can be conducted by reducing the number of fluorescent particles below one in the local illuminated field. In fluorescence imaging, diffraction limits a microscope from imaging the light emitted from a point light source; two neighboring point light sources could not be distinguished. However, the number of particles is countable if the number

of fluorescent particles below one in the local illuminated field. Typical methods for reducing the illuminated field are total internal reflection fluorescence microscopy and stimulated emission depletion microscopy. Absolute quantification of concentration would be difficult for measurements with high particle density.

In measurements with high particle density, fluorescence intensity is a relative quantification of concentration if the brightness of a fluorescent particle is the same for all particles. The brightness of a fluorescent particle depends on four factors: (A) measuring equipment, (B) measurement conditions, (C) photophysical properties of a fluorescent molecule, and (D) oligomeric state. First, a fluorescence microscope consists of several optical elements: objective lenses, dichroic mirrors, emission filters, and light detectors. Second, in measurements via CLSM, typical measurement conditions are excitation wavelength and power, pinhole position and size, sampling time for a pixel (pixel dwell time), and detector gain. Third, the photophysical properties are the excitation and emission spectrum, molar absorption coefficient, fluorescence quantum yield, and possible energy state. Fourth, in the dimerization of two fluorescently labeled monomers into a dimer, a dimer carries two fluorescent molecules; thus, the brightness of a single particle is twice that of a monomer. If it is uncertain that the above four factors are the same, the relative comparison of concentration will fail. However, the concentration and brightness of a single particle can be estimated by analyzing the fluctuation in fluorescence intensity. Especially, this estimation is useful to understand the oligomeric state of proteins in living cells. Through experiments, the first three factors are commonly known, but the fourth factor is unknown for oligomer-forming proteins.

Fluorescence fluctuation spectroscopy (FFS) (1–3) is a general term for methods that analyze the temporal and spatial fluctuations in fluorescence intensity. Fluorescence correlation spectroscopy (FCS) (4) is a well-known method. FCS analyzes temporally correlated fluctuations that originated from diffusing particles, and FCS can obtain concentration, oligomeric state, and rate of diffusion. Typically, FCS is implemented with CLSM. FCS is applied to a single-spot measurement, and spatial distribution information is not obtained. Another method for providing spatial distribution information that is implemented with CLSM is number and brightness (N&B) analysis (5).

N&B analysis is a statistical analysis for analyzing temporally independent fluctuations in photon-counting images, and N&B analysis provides two-dimensional images reflecting the concentration and brightness of a single particle. In N&B analysis, CLSM successively counts photons while sampling and records the counts as an image. Iterative scanning for an image produces an image series. The statistical analysis is based on the method of moments (MoM) approach for pixels at the same position in the image series; temporal fluctuation affects results at a pixel position, but spatial fluctuations do not affect results. N&B analysis is more advantageous for monitoring the spatial distribution in living cells than FCS.

1.3 Monitoring Oligomeric State by N&B Analysis

As a possible application of N&B analysis, the oligomeric state of proteins can be monitored. In signal transduction in cells, some receptor proteins assemble as oligomers via specific ligand stimulation and trigger downstream cellular functions. For example, a glucocorticoid receptor (GR) (6–8) is a possible target. GRs are nuclear receptors and localize in the cytoplasm as monomers before ligand stimulation. The stimulation activates GRs, and GRs translocate into the nucleus. Dimerized GRs bind to glucocorticoid response elements in the nucleus and act as transcriptional factors. In the downstream, metabolic pathways and anti-inflammatory responses are regulated. In GRs, the dynamic change of concentration and oligomeric state is related to the cellular response. Effective characterization of the oligomeric state can improve the understanding of response regulation in living cells.

1.4 Basic Theory for N&B Analysis

I describe a basic theory for estimation based on the MoM approach. The moments of a probability distribution are characteristic values of the probability distribution; the n -th raw moment for discrete probability distribution $P(X)$ is defined by an expectation of random variable X to the n -th power as follows:

$$E[X^n] := \sum_{X=0}^{\infty} X^n P(X). \quad (1.1)$$

In observing temporal fluctuations for photon counting, We make the following assumptions: (a) the number of fluorescent diffusing particles in a measurement volume during a sampling time does not change; (b) the number fluctuation of the particles follows a Poisson distribution; (c) photon emission fluctuation from a single particle and photoelectron cascade fluctuation in a light detector follow a Poisson distribution. Assumption (a) would be validated if the sampling time is sufficiently short compared with the residence time of diffusing particles in the measurement volume. Assumption (b) would be validated if the measurement volume is significantly smaller than the volume at which particles can diffuse freely. Poisson distribution is a model for rare events; the observation of particles would be rare if the above condition is satisfied. In an experiment implemented using CLSM for diffusing particles in a HeLa cell, the measurement volume is approximately 0.2 fL, and the volume of a HeLa cell is 3700 ± 1500 fL; approximately, the assumption would be validated. Under these assumptions, the probability distribution for observing X photons is given by a Neyman type A distribution as follows:

$$\text{Ney}(X|\nu, \varepsilon) := \sum_{Z=0}^{\infty} \text{Poi}(X|\varepsilon Z) \text{Poi}(Z|\nu), \quad (1.2)$$

where $\text{Poi}(Z|\nu)$ is a Poisson distribution given as follows:

$$\text{Poi}(Z|\nu) := \frac{\nu^Z}{Z!} \exp(-\nu), \quad (1.3)$$

where ν denotes the particle number, temporal mean of the number of particles in the measurement volume; Z represents a realized outcome of the Poisson distribution; and ε denotes the particle brightness, temporal mean of the number of photons emitted from a single particle. The probability-generating function of Neyman type A distribution is given as follows:

$$\begin{aligned} G(z) &:= \sum_{X=0}^{\infty} z^X P(X) \\ &= \exp[\nu\{\exp[\varepsilon(z-1)] - 1\}]. \end{aligned} \quad (1.4)$$

The i -th order derivative of the probability-generating function with respect to z is given as follows from mathematical induction ($i \geq 1$):

$$\frac{\partial^i G}{\partial z^i}(z) = \sum_{j=0}^{i-1} \binom{i-1}{j} \nu(\varepsilon)^{i-j} \exp[\varepsilon(z-1)] \frac{\partial^j G}{\partial z^j}(z). \quad (1.5)$$

Substituting $z = 1$ into the definition of the probability-generating function yields factorial moments as follows:

$$\frac{\partial^i G}{\partial z^i}(1) = E[X(X-1)(X-2) \dots (X-i+1)]. \quad (1.6)$$

Substituting $z = 1$ and Eq. 1.6 into Eq. 1.5 produces factorial moments recursively. The first and second factorial moments are given as follows:

$$E[X] = \nu\varepsilon, \quad (1.7)$$

$$E[X(X-1)] = \nu\varepsilon^2 + \nu^2\varepsilon^2. \quad (1.8)$$

Solving Eqs. 1.7 and 1.8 for ν and ε yields

$$\nu = \frac{E[X]^2}{E[X^2] - E[X]^2 - E[X]}, \quad (1.9)$$

$$\varepsilon = \frac{E[X^2]}{E[X]} - E[X] - 1. \quad (1.10)$$

The raw moments cannot be obtained experimentally, but they can be approximated through independent observations. Let us define an imaging duration as the period between the current sampling and the next sampling at a pixel position. Independent observations are possible if the imaging duration is sufficiently longer than the residence time of particles in the measurement volume. For sufficiently large M time-independent observations, the raw moments are approximated as follows, from the law of large numbers:

$$E[X] \approx \frac{1}{M} \sum_{m=1}^M x_m, \quad (1.11)$$

$$E[X^2] \approx \frac{1}{M} \sum_{m=1}^M x_m^2, \quad (1.12)$$

where x_m is m -th observed outcome for X ($m = 1, 2, \dots, M$). Therefore, the estimator for ν and ε are given as follows, with $\bar{x} := \frac{1}{M} \sum_{m=1}^M x_m$ and $\overline{x^2} := \frac{1}{M} \sum_{m=1}^M x_m^2$:

$$\nu = \frac{\bar{x}^2}{\overline{x^2} - \bar{x}^2 - \bar{x}}, \quad (1.13)$$

$$\varepsilon = \frac{\overline{x^2}}{\bar{x}} - \bar{x} - 1. \quad (1.14)$$

For sufficiently large M , the standard deviation of \bar{x} and $\overline{x^2}$ is proportional to $1/\sqrt{M}$ from the central limit theorem.

1.5 References

1. Youker, R.T., and H. Teng. 2014. Measuring protein dynamics in live cells: protocols and practical considerations for fluorescence fluctuation microscopy. *J. Biomed. Opt.* 19:090801.
2. Bag, N., and T. Wohland. 2014. Imaging Fluorescence Fluctuation Spectroscopy: New Tools for Quantitative Bioimaging. *Annu. Rev. Phys. Chem.* 65:225–248.

3. Migueles-Ramirez, R.A., A.G. Velasco-Feliz, R. Pinto-Camara, C.D. Wood, and A. Guerrero. 2017. Fluorescence fluctuation spectroscopy in living cells. *Microsc. imaging Sci. Pract. approaches to Appl. Res. Educ.* 138–151.
4. Elson, E.L., and D. Magde. 1974. Fluorescence correlation spectroscopy. I. Conceptual basis and theory. *Biopolymers.* 13:1–27.
5. Digman, M.A., R. Dalal, A.F. Horwitz, and E. Gratton. 2008. Mapping the Number of Molecules and Brightness in the Laser Scanning Microscope. *Biophys. J.* 94:2320–2332.
6. Oakley, R.H., and J.A. Cidlowski. 2013. The biology of the glucocorticoid receptor: New signaling mechanisms in health and disease. *J. Allergy Clin. Immunol.* 132:1033–1044.
7. Robertson, S., J.P. Hapgood, and A. Louw. 2013. Glucocorticoid receptor concentration and the ability to dimerize influence nuclear translocation and distribution. *Steroids.* 78:182–194.
8. Nicolaides, N.C., Z. Galata, T. Kino, G.P. Chrousos, and E. Charmandari. 2010. The human glucocorticoid receptor: molecular basis of biologic function. *Steroids.* 75:1–12.

Chapter 2

Problems in N&B Analysis and Solutions Provided by This Research

2.1 Organization of the Doctoral Dissertation

In N&B analysis, in 1990, Qian and Elson (1) reported a basic theory that applies to N&B analysis, and in 2008, Digman et al. (2) demonstrated the performance of N&B analysis implemented with laser scanning microscopy. N&B analysis could be used to monitor concentration and oligomeric state in living cells. However, in a practical experiment with fluorescent proteins, the conventional method estimates the particle number and particle brightness with low accuracy and precision. Therefore, we have developed methods for estimating these parameters accurately and precisely.

In Chapter 3, we describe the required conditions for quantitative N&B analysis. A sampling time and an imaging duration (lag time in Chapter 3) are needed for optimization during fluorescence image acquisition. Moreover, in fluorescence measurements, different possible light sources distort the estimated results. Additional fluorescence intensity and fluctuation that are not assumed in the theory result in a biased estimation. Possible light sources are background intensity, intensity drift by organelles, photobleaching, and dead time of a light detector. We describe how to minimize the effect of these sources. Furthermore, we evaluated the influence of the number of images on the particle brightness. To the best of our knowledge, the effect of the number of images on analysis has not been evaluated, and the decision is left to the discretion of analysts. The evaluation indicated that the particle brightness is underestimated in analysis with a small number of images and low fluorescence intensity.

In Chapter 4, we describe a simple method for reducing the dead time effect of a light detector. We refer to the method as two-detector number and brightness (TD-N&B) analysis. Dead time is a nonideal property of a photon detector that causes loss of photon count. Underestimation of the particle brightness has been reported (3, 4). TD-N&B analysis based on the MoM approach is similar to the conventional method, but its estimation is less biased than the conventional method. TD-N&B analysis is implemented with the following three steps: (i) splitting fluorescent light with a half mirror, (ii) detection with double light detectors, and (iii) covariance estimation for double fluorescence signals. We demonstrated the performance of the method via experiments with EGFP solution, EGFP tandem oligomers in lysates, and those in cells. Additionally, we applied the method to monitor the oligomerization state of GRs.

In Chapter 5, we describe a method based on maximum likelihood (ML) estimation and

maximum a posteriori (MAP) estimation, along with the empirical Bayes (EB) method, instead of the MoM approach. We refer to the methods as ML–N&B and EB–MAP–N&B analysis. In the conventional method and TD–N&B analysis, the estimated number and brightness of particles are sometimes negative, which reduces accuracy and precision. ML does not produce negative values for the particle number and particle brightness. Additionally, ML uses information for higher moments, whereas the MoM approach uses information for the first and second moments. Thus, we expected that ML will improve accuracy and precision. However, ML occasionally estimated the particle number as infinity and the particle brightness as 0. This result suggests that temporal information about images is insufficient for determining the parameters as a point estimate. To avoid such estimations, we used spatial information about images by applying MAP estimation and the EB method. In EB–MAP–N&B analysis, we assumed that the particle number at a pixel and that at the surrounding pixels are similar. Because of the diffraction limit and overlap of a measurement volume during samplings, the assumption of similarity would be reasonable. The EB method predicts the particle number at the center pixel using the information in the surrounding pixels, and MAP estimates the particle number and particle brightness based on the prediction. Furthermore, we derived an equation for correcting the dead time effect, which is useful in ML and MAP estimation. Bédard reported the probability distribution for dead time-affected photon count, but the correction with the distribution is not useful in numerical estimation. This is because the probability distribution has an incomplete gamma function and requires numerical integration. In the derived equation, the probability distribution for deadtime-affected photon count is simply represented by a linear combination. We demonstrated the performance of EB–MAP–N&B analysis by experiments with EGFP solution and EGFP tandem oligomers in cells.

2.2 References

1. Qian, H., and E.L. Elson. 1990. On the analysis of high order moments of fluorescence fluctuations. *Biophys. J.* 57:375–380.
2. Digman, M.A., R. Dalal, A.F. Horwitz, and E. Gratton. 2008. Mapping the Number of Molecules and Brightness in the Laser Scanning Microscope. *Biophys. J.* 94:2320–2332.
3. Hendrix, J., W. Schrimpf, M. Höller, and D.C. Lamb. 2013. Pulsed Interleaved Excitation Fluctuation Imaging. *Biophys. J.* 105:848–861.
4. Hillesheim, L.N., and J.D. Müller. 2003. The Photon Counting Histogram in Fluorescence Fluctuation Spectroscopy with Non-Ideal Photodetectors. *Biophys. J.* 85:1948–1958.

Chapter 3

Prerequisites for Quantitative N&B Analysis

3.1 Abstract

Number and brightness (N&B) analysis helps to visualize protein oligomer and its localization in a living cell. N&B analysis provides apparent brightness, which reflects the oligomeric state of a fluorescently labeled protein, by analyzing the temporal intensity fluctuation at each pixel. N&B analysis is useful in understanding the dynamic oligomerization in signal transduction and neurodegenerative diseases. Furthermore, it also helps in gaining useful insights regarding the controlling mechanisms in protein function. In this article, we describe the basic theory and notations of N&B analysis implemented with confocal laser scanning microscopy for quantitative analyses.

3.2 Introduction

3.2.1 *Protein Oligomer*

Brightness analysis (Macdonald et al. 2013) is used to monitor the protein oligomers in a living cell. The protein oligomers can be found in signal transduction and neurodegenerative diseases. In signal transduction, some receptor proteins assemble as oligomer by specific ligands stimulation and trigger the downstream cellular functions. Several researchers have reported that protein oligomerization and aggregation are related to neurodegenerative diseases (Kitamura and Kinjo 2018) (Fang et al. 2014). An effective characterization of the oligomeric state can enhance the understanding of protein functions in living cells. Oligomerization is a dynamic and transient state change, and it demonstrates spatial heterogeneity in a living cell. A technique focused on identifying this spatiotemporal heterogeneity of the oligomeric state is required for accurate understanding. In this chapter, we introduce number and brightness (N&B) analysis method based on fluorescence fluctuation spectroscopy (FFS). N&B method can provide a way to characterize the oligomeric state in a living cell.

3.2.2 *Fluorescence Fluctuation Spectroscopy (FFS)*

Brightness analysis can be performed by fluorescence microscopy coupled with fluorescence fluctuation spectroscopy (FFS) (Youker and Teng 2014). Fluorescence microscopy is utilized to monitor the spatial localization and temporal changes in a fluorescently labeled molecule. Objective lens of the microscope creates an open measurement volume (Fig. 1A) through which the labeled molecules diffuses (Fig. 1B). When these molecules are passing through the measurement volume, the

number of photons is counted within a sampling time (Fig. 1C). The intensity of the recorded photon count signal fluctuates in time and space. FFS is used to analyze this fluctuations, which can help in determining the parameters describing concentration, oligomeric state, or diffusion coefficient etc. Elson and Magde demonstrated FFS for the first time in 1974; they referred it to as fluorescence correlation spectroscopy (FCS) (Elson and Magde 1974). FCS involves the analysis of fluorescence signal by using an autocorrelation function, which provides information about the brightness and the diffusion time. Here, brightness stands for the emitted photon count from a single particle (counts per particle (CPP) or counts per molecule (CPM)), and the diffusion time implies characteristic residence time in measurement volume. Both these parameters can be used to detect oligomerization. However,

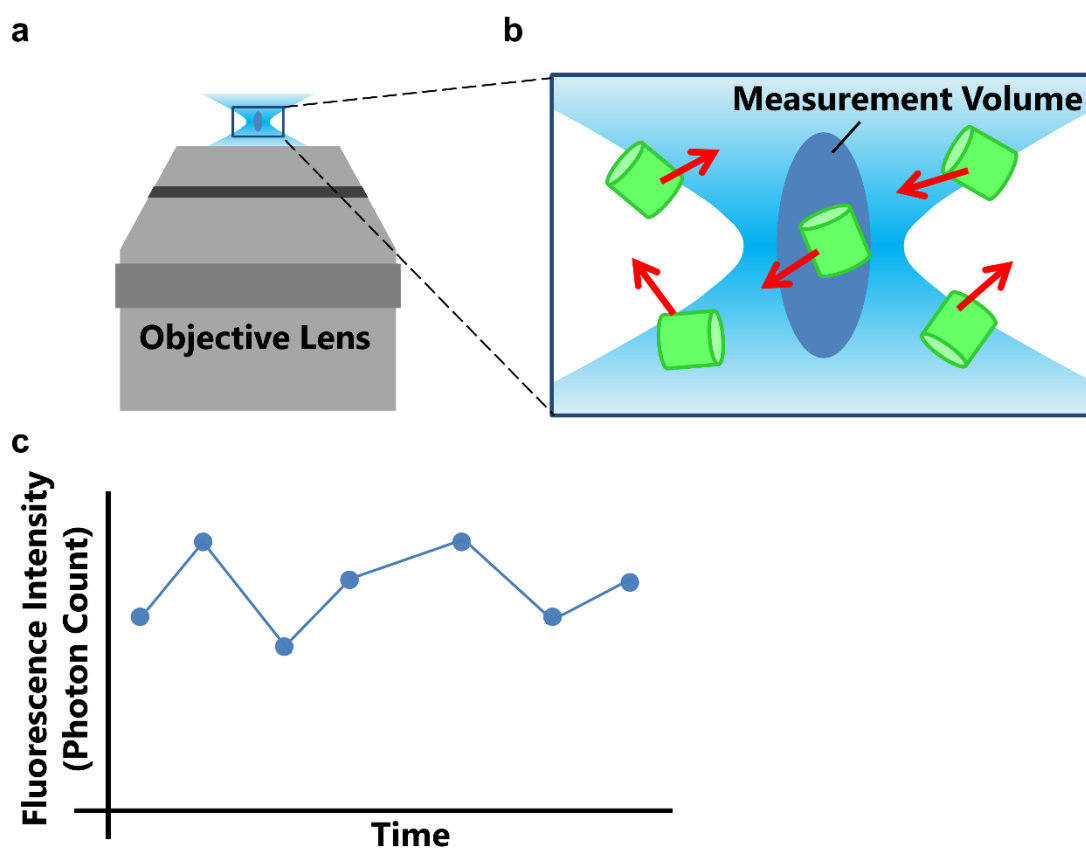


Fig. 1. Fluorescence fluctuation measurement using a confocal fluorescence microscope. (A) Objective lens creates an open measurement volume by excitation light (light blue). The dark blue ellipse is the measurement volume (confocal region). (B) Diffusion of fluorescent proteins (green cylinder) through the measurement volume. The red arrows indicate the direction of the diffusion. (C) Fluorescence intensity, i.e., the intensity of the photons emitted by the diffused proteins.

FCS is a single-spot measurement, and it is difficult to monitor changes as a two-dimensional image even though multiple point measurement are performed (Krmopot et al. 2015) (Yamamoto et al. 2018). In addition, diffusion time analysis of FCS is not sensitive enough to distinguish a small change in the oligomerization, e.g., monomer to dimer conversion. Here, we assume that monomer and dimer are spheres with molecular weights of M_w and $2M_w$, respectively. Considering the diffusion time of the monomer to be τ_D , Stokes-Einstein relation implies that the diffusion time of dimer is $\sqrt[3]{2}\tau_D$. It is difficult to detect this small ratio in FCS to distinguish monomer and dimers (Meseth et al. 1999). In contrast, brightness analysis can help to distinguish a small change in the oligomerization compared to diffusion time.

3.2.3 Brightness Analysis

Brightness analysis is based on a general assumption that the recorded photon count is a random variable following the product of two Poisson distribution (Qian and Elson 1990a). The first Poisson distribution originates from the number fluctuation of diffusing particles in a measurement volume. The second distribution originates from photon emission fluctuation from a single particle and photoelectron cascade fluctuation in the detector. For one-component system, brightness (details are

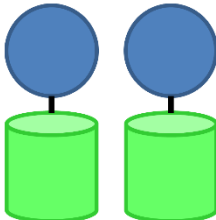
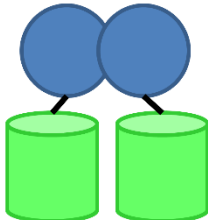
	Fluorescent Protein	Monomer	Dimer
			
Fluorescence Intensity	\bar{X}	$2\bar{X}$	$2\bar{X}$
Particle Number	1	2	1
Brightness	B	B	$2B$

Fig. 2. Reflection of oligomeric state by brightness. Brightness analysis of a fluorescent protein (green cylinder), fluorescently labeled two monomers (blue circle), and dimerized protein. This brightness is the fluorescence intensity from a single particle. If a fluorescent protein has an intensity of \bar{X} , the measured fluorescence intensities for the monomer and the dimer are $2\bar{X}$ and $2\bar{X}$, respectively. The particle number becomes half by the dimerization. The dimer carries two fluorescent proteins. Therefore, the brightness of the dimer is two times higher.

provided in Sec. 2) analysis can help to characterize the oligomeric state. We consider the brightness analysis for one-component system containing fluorescent protein, fluorescently labeled monomer, and dimer, respectively, as shown in Fig. 2. If the fluorescence intensity for monomers and a dimer is same ($2\bar{X}$ and $2\bar{X}$, respectively), the particle number for the dimer is a half of monomers. The dimer carries two fluorescent proteins; therefore, dimeric brightness is two times higher than monomeric brightness (B for monomer, $2B$ for dimer). The brightness of monomer normalized by brightness of fluorescent protein can give normalized brightness of 1, and that of dimer gives normalized brightness of 2. The ratio of the normalized brightness is larger than that of the diffusion time for monomer and dimer.

3.2.4 Introduction for Number and Brightness Analysis

Number and brightness (N&B) analysis (Digman et al. 2008)(Nolan et al. 2017b) can help to investigate the temporal fluctuations in fluorescence image series. It determines the apparent brightness across the whole image and generates a brightness map with pixel resolution. In contrast to FCS, it does not provide information about the characteristic residence time in the measurement volume. N&B analysis can help to resolve spatially heterogeneous oligomer distribution. It cannot resolve mixture of different brightness in same pixel (details are provided in Sec, 2). An advantage of this technique as compared to other analysis methods is that N&B analysis can be applied to fast-diffusing molecules, such as soluble proteins in a living cell. In Imaging FCS, the applicability is limited to slow-diffusing molecules, such as membrane binding protein (details are provided in Sec. 4).

N&B analysis has been used in various research areas including oligomeric receptors and aggregation forming proteins. Zamai et al. revealed that fibroblast growth factor-2 (FGF2) and neural cell adhesion molecule (NCAM) form dynamic and transient oligomer at cell membrane (Zamai et al. 2019). Ojosnegros et al. applied N&B analysis to demonstrate clustering models of Eph receptors (Ojosnegros et al. 2017) (Cutrale et al. 2019), and proposed a polymerization-condensation model. Ossato et al. monitored inclusion formation in huntingtin peptide (Ossato et al. 2010). Monitoring of protein transition into an oligomer is of paramount importance. As mentioned before, FCS fails to monitor the oligomerization because it is single-spot measurement. Therefore, N&B analysis could serve as a better way to monitor the oligomerization and its localization over time in a living cell.

3.2.5 Organization of the article

Section 3.3 of this article describes the basic theory of N&B analysis along with an investigation of various parameters. Section 3.4 describes the notations used in N&B analysis implemented with confocal laser scanning microscopy. Apparent brightness is prone to be a biased parameter. Various

factors, such as sampling time, additional intensity and fluctuations, frame number, and non-fluorescent state of labeled protein can lead to this bias. We have also derived equations to evaluate the influence on apparent brightness under a low frame number. Section 3.5 provides the comparison of N&B analysis and other FFS techniques.

3.3 Number and Brightness (N&B) Analysis

The basic theory of N&B analysis was first proposed in 1990 (Qian and Elson 1990a) (Qian and Elson 1990b) and it was demonstrated in a living cell in 2008 (Digman et al. 2008). N&B analysis estimates the apparent brightness and apparent number from the fluctuations in photon count. The analysis is conducted on every pixel of a fluorescence image and it produces an apparent brightness map with single pixel resolution. Digman et al. performed N&B analysis on fluorescence image series using a confocal laser scanning microscope (CLSM) equipped with two-photon excitation measurement and a photomultiplier tube (Digman et al. 2008). It was also demonstrated that it is possible to use images obtained from a detector operating in analog mode (Dalal et al. 2008) and total internal reflection fluorescence microscopy equipped with an electron-multiplied charge-coupled device (EMCCD) (Unruh and Gratton 2008).

We assume that the measurement sample is a freely diffusing fluorescent particle and measure the photon counts with a sampling time (pixel time) equal to T_{sampling} [s], and collect m images. Let X_i ($i = 1, 2, 3, \dots, m$) be the number of photon counts in the i^{th} image at a pixel. We define estimators as the ratio of factorial cumulants, and it can be written by sample raw moments as following: (Müller 2004):

$$B := \frac{\kappa_{[2]}}{\kappa_{[1]}} = \frac{\overline{X^2} - \overline{X}^2 - \overline{X}}{\overline{X}}, \quad (1)$$

$$N := \frac{\kappa_{[1]}^2}{\kappa_{[2]}} = \frac{\overline{X}^2}{\overline{X^2} - \overline{X}^2 - \overline{X}}, \quad (2)$$

where, B and N are the apparent brightness and apparent number, respectively. $\kappa_{[1]}$ and $\kappa_{[2]}$ are first and second order factorial cumulant, respectively. \overline{X} is sample mean (Eq. S1.1), and $\overline{X^2} - \overline{X}^2$ is sample variance (Eq. S1.2). The estimation of apparent brightness has been reported in various articles; however, information about apparent number and quantitative comparison is scarce. To our knowledge, apparent number has low precision and exhibits outliers in their map compared to apparent brightness.

The estimators can be expressed as function of particle brightness ε and particle number n ,

$$B = \frac{\gamma_2 \sum_{l=1}^c \varepsilon_l^2 n_l}{\sum_{l=1}^c \varepsilon_l n_l}, \quad (3)$$

$$N = \frac{(\sum_{l=1}^c \varepsilon_l n_l)^2}{\gamma_2 \sum_{l=1}^c \varepsilon_l^2 n_l}, \quad (4)$$

where, particle brightness (or molecular brightness) is the average photon count emitted from a single particle in sampling time, $\varepsilon_l/T_{\text{sampling}}$ is particle brightness in Hz [Hz/particle], particle number n_l is the average number of particle in measurement volume, the subscript l represents l^{th} component, and γ_2 is the γ -factor, which is a constant that depends on the shape of point spread function (Thompson 1991)(Chen et al. 1999) (Eq. S2.14).

If we assume that the measurement system is composed of a single component ($c = 1$), estimators B and N can be expressed as follows:

$$B = \gamma_2 \varepsilon_1, \quad (5)$$

$$N = \frac{1}{\gamma_2} n_1. \quad (6)$$

N&B analysis users should note that apparent brightness is just a weighted average of multiple particle brightness without any constraint on the number of components. N&B analysis cannot resolve different components. The users need to consider the appropriate constraint. If the system is composed of two components, the particle number ratio can be determined by independent reference measurements (Fukushima et al. 2018). For further investigation in multiple components system, higher order moment estimation is required.

Studies estimating higher order moments have been reported in the literature. With respect to FCS, Palmer and Thompson derived a higher order correlation function based on higher moments (Palmer and Thompson 1987) (Palmer and Thompson 1989a) (Palmer and Thompson 1989b). Melnykov and Hall improved the formulation based on cumulants (Melnykov and Hall 2009). This made the formulation simple and facilitated its application towards the characterization of chemical reactions. Abdollah-Nia et al. proposed methods to reduce the bias caused by detector dead time and after pulse by improving data collection and analysis (Abdollah-Nia et al. 2017a) (Abdollah-Nia et al. 2017b). The disadvantage of higher order moments and cumulants is that a larger number of sampling (frame number) is required to obtain a reliable estimated value. Furthermore, error analysis of the estimator (variance of estimator) is necessary to evaluate the reliability (uncertainty).

3.4 Notation used in N&B analysis

In this section, we describe necessary conditions for quantitative measurements. Apparent brightness

is easy to be biased (see Sec. 3.1-3.4), and normalized brightness does not always correspond to oligomeric state. We strongly recommend brightness calibration using monomer fluorescent label and tandem linked oligomers (dimer, trimer, tetramer, pentamer, etc.) (Pack et al. 2006) for every experiment (Macdonald et al. 2013)(Chen et al. 2010). Apparent brightness depends on the laser power and optical system, which is prone to day-to-day variations.

For later discussions, we assume that N&B analysis is implemented with confocal laser scanning microscopy (CLSM) and photon counting images unless otherwise noted. For the analog detector system, readers are referred to the following article describing additional factors (Dalal et al. 2008).

3.4.1 Optimal Sampling Time and Lag Time

In image acquisition, a pixel value is obtained within a sampling time, and a pixel size is the x and y length of a pixel in a CLSM image. The x length is a scanning distance in the sampling time, and the y length depends on the x length. An image is obtained by scanning measurement volume across a sample (Fig. 3A), and image series is obtained by repeating the image acquisition multiple times (Fig. 3B). Let us define the notations as follows. Sampling time (T_{sampling}) is defined as the time required to measure photon count that corresponds to a pixel value (pixel dwell time). T_{frame} is described as the time duration required to obtain an image, and T_{wait} is the waiting time between two frame acquisitions. T_{lag} is the lag time, i.e., the time between two continuous pixel acquisitions (Fig. 3C). T_{sampling} and T_{lag} are needed to be set appropriately for quantitative measurements. τ_D is the characteristic residence time in measurement volume for diffusing particles. T_{sampling} should be smaller than τ_D ($T_{\text{sampling}} \ll \tau_D$) (Digman et al. 2008). Furthermore, T_{lag} should to be larger than τ_D ($\tau_D \ll T_{\text{lag}}$) (Nolan et al. 2017b).

The photon count fluctuations are required to obtain the particle number fluctuations as hidden parameters. For pixel acquisition, if the sampling time is not small enough, the number of particles during this time would change by diffusion. In addition, N&B analysis does not assume data dependent sampling at each photon count. If the lag time is shorter than the characteristic residence time, the fluorescence particle would appear to be immobile (see Sec. 3.2.1). Therefore, a longer waiting time is required to avoid the data dependent sampling.

Optimization of sampling time is required for a precise estimation. Measurements with short sampling time lead to small photon counts, and reduced signal-to-noise ratio. However, as mentioned before, the sampling time is often restricted by a characteristic residence time. In FFS, Müller derived a theory to extend the sampling time in fluorescence cumulant analysis (FCA) (Müller 2004) and time-integrated fluorescence cumulant analysis (TIFCA) (Wu and Müller 2005). They evaluated the influence of sampling time on cumulants and corrected the diffusion effect during the sampling time. A similar theory is applied in mean-segmented Q (MSQ) analysis (Hur and Mueller 2015) and time-integrated multipoint moment analysis (TIMMA) (Oh et al. 2011) (see Sec. 4).

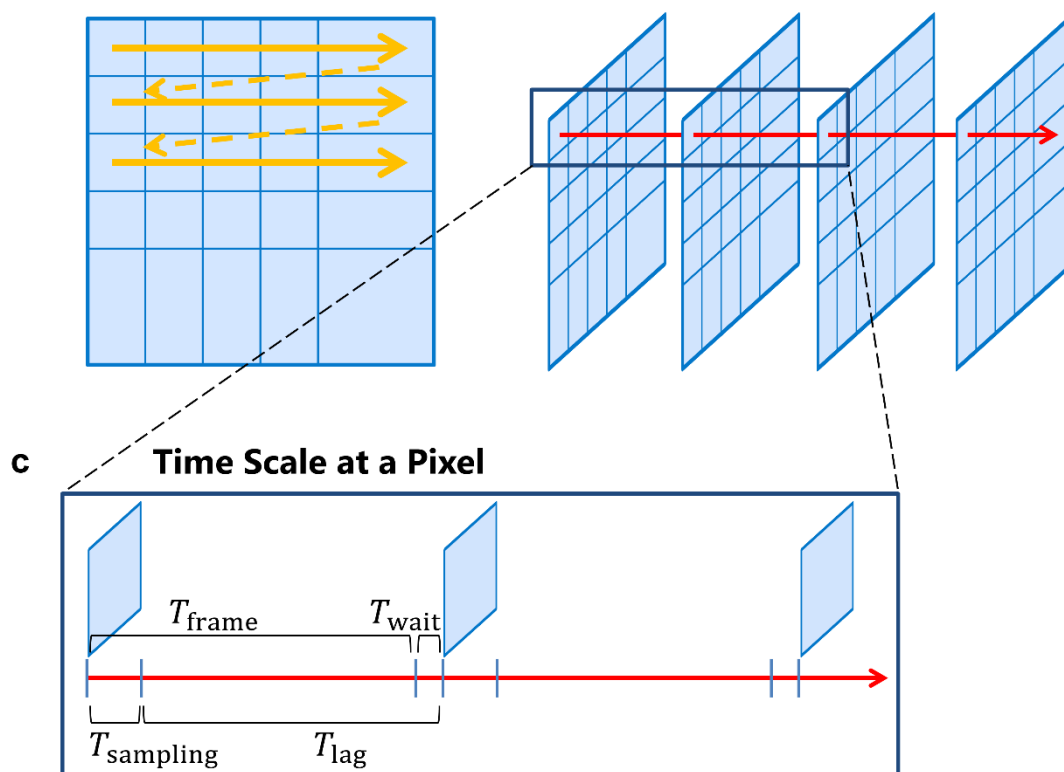
a Image Acquisition (scanning) b Image Acquisition over Time


Fig. 3. Image acquisition in laser scanning microscopy. (A) A pixel value is obtained within a sampling time, and an image is obtained by scanning the measurement volume. The solid and dotted arrows indicate the scanning and moving directions, respectively. (B) Image series is obtained by repeating the image acquisition. Red arrow indicates the passage of time. (C) Sampling time (T_{sampling}) is the duration required to obtain a pixel value. The frame time (T_{frame}) is the time required to obtain an image. The waiting time (T_{wait}) is the duration between two frame acquisitions. The lag time (T_{lag}) is time between a pixel acquisition and the next acquisition at the same pixel.

3.4.2 Additional Photon Counts and Signal Fluctuations

If the recorded photon counts and the signal fluctuations originate from diffusing fluorescent particles only under a stationary signal, the theory described previously works well. However, there are several additional sources of photon counts and signal fluctuation. In this section, we have described the influence of some of these factors, such as (1) background, (2) non-stationary signal (intensity drift and photobleaching), (3) detector dead time and afterpulse and (4) additional factors. These factors may introduce bias if they are not corrected or removed.

Background Intensity

In brightness analysis, background signal affects the estimated value. For example, dark count, stray light, autofluorescence, and immobile fraction contribute to the background signal. Some of these sources can be removed by modifying the condition of measurement. If the background signal is quite low as compared to the target fluorescence, the influence of the background would be negligible. Otherwise, appropriate correction is recommended.

Dark count is defined as the inherent photon count of detectors in the absence of incident light. Stray light originates from the optical system. The dark count and stray light can be corrected by subtracting the average photon count obtained by a reference measurement (Digman et al. 2008).

$$B_{\text{bgCorr}} := \frac{\overline{X^2} - \overline{X}^2 - \overline{X}}{\overline{X} - \overline{X}_{\text{bg}}}, \quad (7)$$

$$N_{\text{bgCorr}} := \frac{(\overline{X} - \overline{X}_{\text{bg}})^2}{\overline{X^2} - \overline{X}^2 - \overline{X}}, \quad (8)$$

where, B_{bgCorr} and N_{bgCorr} are the background corrected estimators for apparent brightness and apparent number, respectively. \overline{X}_{bg} is the average photon count of the background.

Autofluorescence correction is essentially difficult, as the autofluorescence intensity is different depending on cell and cellular components. It is recommended to confirm that the autofluorescence is quite low compared to target fluorescence intensity in all measurements.

N&B analysis determines the brightness of only diffusing particles. The basic theory described in Sec. 2 cannot determine brightness of immobile particles, such as particle binding to cellular structure. Qian and Elson evaluated the immobile fraction by introducing third moment for the system composed of a mobile and immobile fraction (Qian and Elson 1990a). In this evaluation, it was assumed that photobleaching is negligible for both fractions. However, immobile particles are continuously excited and easy to be photobleached. Skinner et al. evaluated the influence of immobile fraction on brightness in FFS under similar conditions (Skinner et al. 2008).

Non-stationary Signal (Intensity Drift and Photobleaching)

The brightness estimator gives apparent brightness accurately under stationary signal. However, various factors distort the signal. For example, in a measurement of fluorescently labeled soluble proteins in a living cell, presence of large organelles or vesicles coming in and out of measurement volume can cause a transient intensity drift. In addition, the cellular movements and focus drift can also contribute to the intensity drift. Another factor is photobleaching which can decrease the measured intensity over time. To obtain a robust estimate, the bias caused by the intensity drift can be reduced by a segmentation, and the bias caused by the photobleaching can be reduced by the segmentation

along with detrending with a line or a curve.

Segmentation divides a signal sequence into multiple segments in time direction, and apparent brightness values are estimated at each segment (Fig. 4A). If the intensity drifts are rare, only few segments would be biased. Therefore, the average of multiple segmented brightness values would be less biased as compared to their unsegmented counterparts (Chen et al. 2002)(Macdonald et al. 2013). This approach could also reduce the bias caused by mild photobleaching as described later. In FFS, an effective application of the segmentation can be found in mean-segmented Q (MSQ) analysis (Hur and Mueller 2015). Hur and Mueller used different length of the segmentation to obtain a robust estimate of brightness.

Boxcar filtering is a similar way to reduce the bias caused by the intensity drifts and mild photobleaching (Trullo et al. 2013). The difference is the presence or absence of the overlap in each segment. A boxcar filter divides a signal sequence into multiple segments by moving sliding window frame by frame (Fig. 4B). For example, if we consider a signal sequence consisting of 10 photon counts, segmentation with a length of 5 generates 2 segments. In contrast, boxcar filtering with a length of 5 generates 6 segments.

Photobleaching (photodepletion) is an irreversible process in which fluorescence molecules turn into non-fluorescent molecules. In contrast, the decrease could be alleviated by diffusing fluorescent molecule coming out of the measurement volume (Petrášek and Schwille 2008). The estimated brightness is overestimated under photobleaching (Hur et al. 2014). Generally, it is recommended to reduce excitation laser power. When photobleaching cannot be avoided, bias correction is

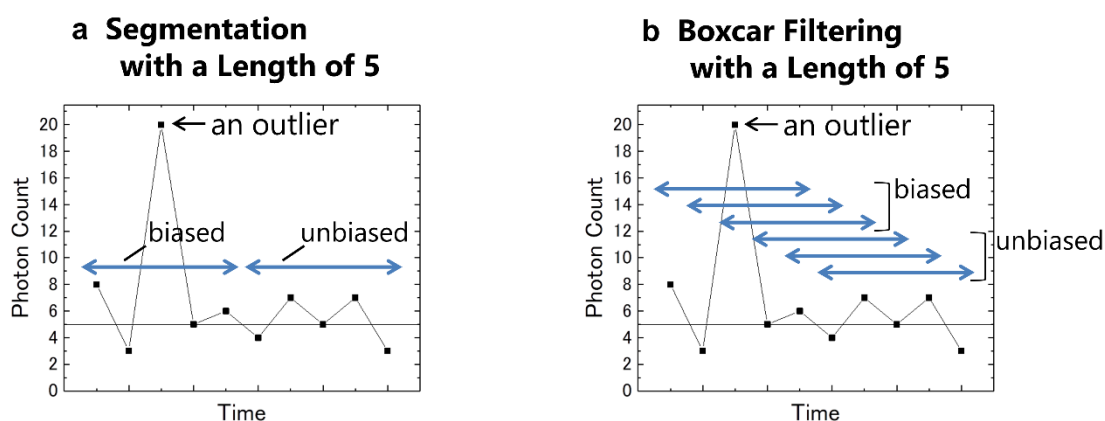


Fig. 4. Segmentation and boxcar filtering. The signal sequence has 10 photon counts which contain 1 outlier. Estimation with a length of 10 leads to biased brightness by the outlier. (A) Segmentation divides the signal sequence into multiple segments without overlap. Segmentation with a length of 5 divides the signal sequence into 2 segments. (B) Boxcar filtering divides the signal sequence with overlap. Boxcar filtering with a length of 5 divides the signal sequence into 6 segments.

recommended.

Caccia et al. removed the decreasing trend with sum of two exponential decay (Caccia et al. 2005). Hur et al. evaluated the estimation bias caused by photobleaching by assuming single exponential decay (Hur et al. 2014), and demonstrated that the bias depends on the initial number of molecules in measurement volume and “photodepletion fraction”. The photodepletion fraction is a decreasing function of the initial fluorescence intensity during the measurement. This indicates that segmentation is also effective to reduce the bias. Nolan et al. discussed the application of exponential filtering to remove the decreasing trend and automatic parameter selection for filtering (Nolan et al. 2017a).

In addition to brightness overestimation, another problem of photobleaching is the decrease in brightness of the oligomer. For example, in a dimer complex carrying 2 EGFPs, photobleaching on the half side of EGFP will produce another bright species, that is, dimer complex carrying single EGFP. Hur et al. derived an equation to obtain initial brightness under single exponential decay (Hur et al. 2014).

Detector Dead Time and Afterpulsing

Presence of detector dead time and afterpulse can lead to concentration-dependent brightness (Hillesheim and Müller 2003) (Hendrix et al. 2013). Dead time is the period after the detection of a photon in which detectors cannot detect another photon, leading to a loss of photon count (Fig. 5A). Afterpulse is a spurious pulse following a genuine pulse, which result in addition of photon counts sometimes (Fig. 5B). O’Donnell and Campbell evaluated photon count distribution affected by dead time (O’Donnell 1986) and afterpulsing (Campbell 1992). Hillesheim and Müller evaluated relative

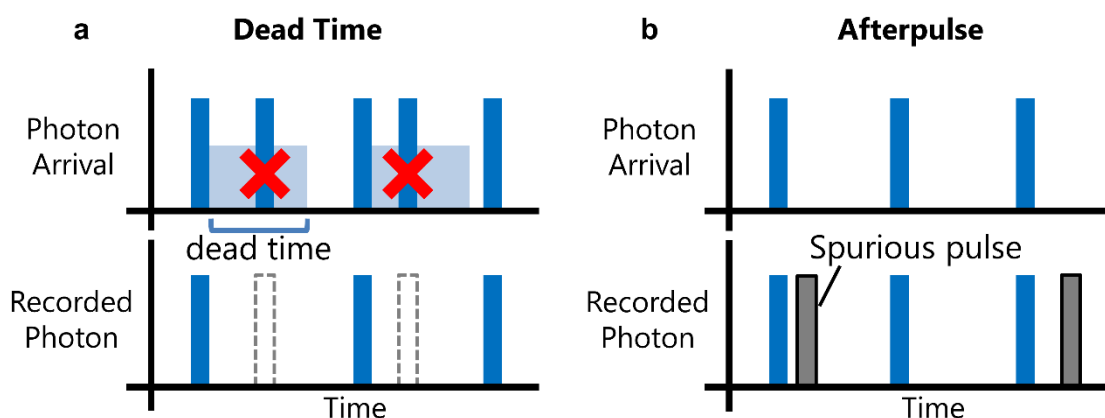


Fig. 5. Dead Time and afterpulsing. The blue bars show the arrival time of photon. (A) Dead time is the time period after photon detection in which detectors cannot detect any photon. The gray dashed bars are photon which are not recorded. (B) Afterpulse is a spurious pulse (gray bar) following a genuine pulse, which occasionally result in increase of photon count.

error of brightness estimator as Mandel's Q factor (Hillesheim and Müller 2003). They claimed that afterpulsing can be neglected in typical experiments equipped with avalanche photodiode (APD). Sanchez-Andres et al. reported that time-shifted covariance estimation is useful to reduce this effect (Sanchez-Andres et al. 2005). An application of time-shifted covariance is also found in N&B analysis with image series obtained by EMCCD (Unruh and Gratton 2008). However, the time-shifted covariance estimation cannot be applied to image series obtained by CLSM because the time-series data is independent. We previously reported that a useful way to reduce the effect of dead time and afterpulsing in N&B analysis is covariance estimation between two detectors (Fukushima et al. 2018). In two-detector system, a half mirror splits the fluorescence signal into two channels. Consequently, covariance estimation reduced the effect of dead time and afterpulsing.

Additional Factors

The geometry of excitation light can also lead to biased brightness. It has been reported that the use of oil-immersion objective can cause focal depth dependent bias (Macdonald et al. 2013). Photon count collection at deep positions into the sample can cause spherical aberration, leading to biased brightness. The use of water-immersion objective with well-adjusted correction collar allows focal depth independent estimation.

In addition, the geometry of sample can also lead to the biased brightness. Basic FFS theory assumes that the measurement volume completely overlaps with the sample. However this is not true for measurements at the peripheral regions of living cell. The measurement volume overlaps with the peripheral region as a thin layer. Macdonald et al. reported z-scan FFS to remove this bias (Macdonald et al. 2010). They suggested that the thin layer can be approximated by rectangular slab, and derived an equation to estimate the thickness of the slab by scanning along z direction. Consequently, they recovered unbiased brightness by correcting γ -factor.

Only the large-scale variations due to intensity drifts and photobleaching can be identified through signal intensity changes. However, a small signal fluctuation process leading to biased brightness was recently reported. Hennen and coworker reported that nuclear membrane undulation leads to biased brightness (Hennen et al. 2017). The nuclear membrane consisted of inner nuclear membrane and outer nuclear membrane. The membranes were separated by lumen. They found an additional exponential correlation term in signal fluctuation due to lumen localized protein.

3.4.3 Frame Number

Frame number is the number of frames in fluorescence image series for estimation. The time dependent change of parameters is not considered in N&B analysis. Low frame number increases the time resolution. Ojosnegros et al. applied boxcar filtering to increase the time resolution (Ojosnegros et al. 2017). However, low frame decreases precision as well as accuracy of measurement. To our

knowledge, very few reports are available on the effect of frame number. The determination of appropriate frame number depends on the judgement of users. We derived the following equation to evaluate the influence of frame number on accuracy. This is the approximate solution for expected apparent brightness and its relative error for one component system (see Supplementary Information 1 for derivation).

$$E[B] = \gamma_2 \varepsilon_1 - \frac{1}{m} (\gamma_2 \varepsilon_1 + 1) - \frac{1}{m} \frac{1}{\varepsilon_1 n_1} (\gamma_3 \varepsilon_1^2 - \gamma_2^2 \varepsilon_1^2 + \gamma_2 \varepsilon_1) + O\left(\left(\frac{1}{m}\right)^2\right), \quad (9)$$

$$\frac{E[B] - \gamma_2 \varepsilon_1}{\gamma_2 \varepsilon_1} = -\frac{1}{m} \frac{1}{\gamma_2 \varepsilon_1} \left\{ (\gamma_2 \varepsilon_1 + 1) + \frac{1}{\varepsilon_1 n_1} (\gamma_3 \varepsilon_1^2 - \gamma_2^2 \varepsilon_1^2 + \gamma_2 \varepsilon_1) \right\} + O\left(\left(\frac{1}{m}\right)^2\right), \quad (10)$$

where $E[B]$ is the expected value of B , m is the frame number, and $\varepsilon_1 n_1$ is average photon count in a sampling time. A similar approximation was previously reported in the ratio estimation (van Kempen and van Vliet 2000), autocorrelation function (Schätzel et al. 1988) (Saffarian and Elson 2003), and mean segmented Q (MSQ) analysis (Hur and Mueller 2015). Eq. (9) indicates that the estimator is asymptotically equal to the true value with enough frame number and average photon count, but the bias is not negligible when the frame number or average photon count is less. Eq. (10) indicates that the relative error becomes smaller for high particle brightness. Fig. 6A shows the dependence of frame number on the relative error with different particle brightness. Here, symbols correspond to simulated results, and the dashed lines represent the theoretical value expected by Eq. (10). A relative error of 0 implies that there is no deviation between the true and estimated values. The relative error approaches zero with increasing frame number. The estimated brightness was critically underestimated, especially for lower particle brightness. This suggests that reducing the excitation laser power to avoid photobleaching or decreasing the frame number to improve time resolution in a careless manner could cause bias. Fig. 6B shows the dependence of the average photon count (\bar{X}) on relative error. The relative error decreased for average photon count equal to 1, and it saturated when the average photon count exceeded 1. A simple solution to reduce the bias is correction. A less biased estimator B_{corr} can be defined as follows:

$$B_{\text{corr}} := B + \frac{1}{m} (B + 1), \quad (11)$$

$$E[B_{\text{corr}}] = \gamma_2 \varepsilon_1 - \frac{1}{m} \frac{1}{\varepsilon_1 n_1} (\gamma_3 \varepsilon_1^2 - \gamma_2^2 \varepsilon_1^2 + \gamma_2 \varepsilon_1) + O\left(\left(\frac{1}{m}\right)^2\right), \quad (12)$$

$$\frac{E[B_{\text{corr}}] - \gamma_2 \varepsilon_1}{\gamma_2 \varepsilon_1} = -\frac{1}{m} \frac{1}{\gamma_2 \varepsilon_1} \frac{1}{\varepsilon_1 n_1} (\gamma_3 \varepsilon_1^2 - \gamma_2^2 \varepsilon_1^2 + \gamma_2 \varepsilon_1) + O\left(\left(\frac{1}{m}\right)^2\right). \quad (13)$$

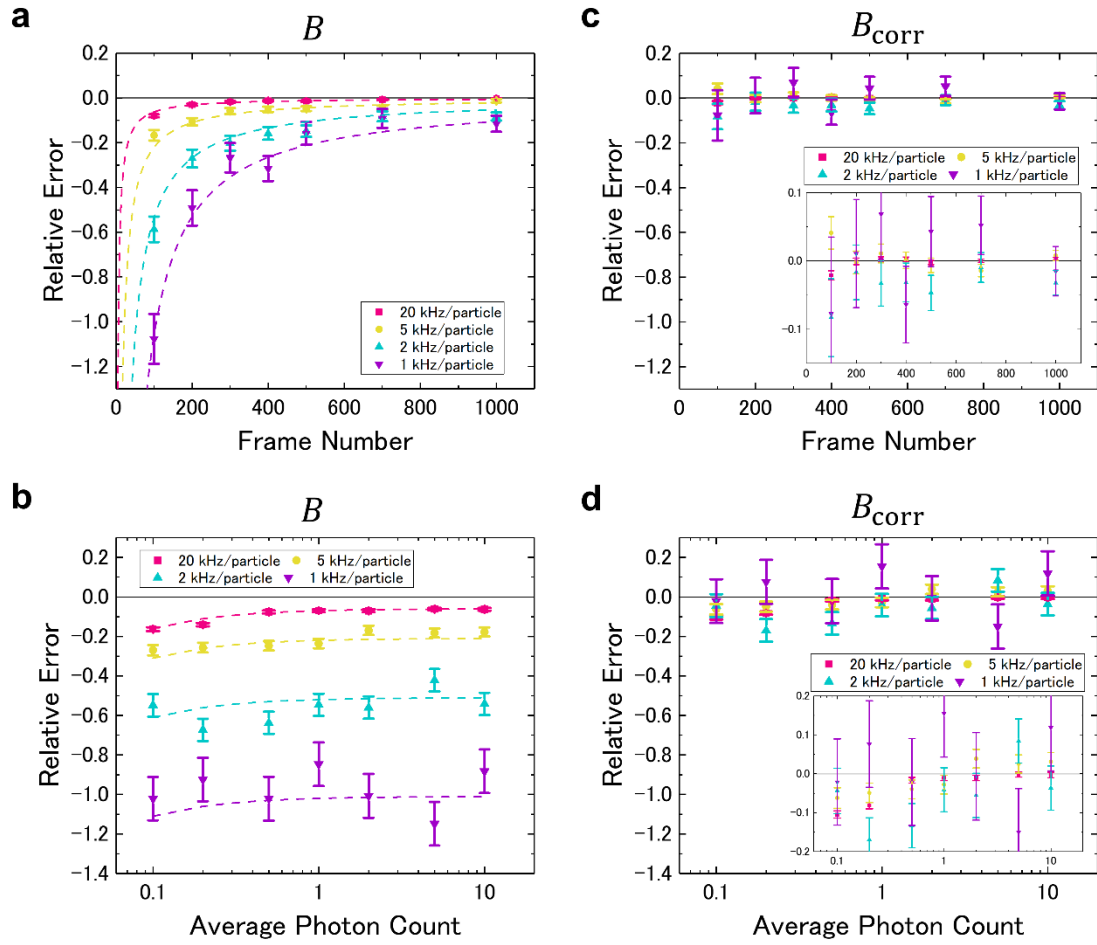


Fig. 6. Dependence of frame number and average photon count on accuracy. Average and standard error estimated from the simulations. The dotted line is the expected value. Dependence of frame number on the relative error with different particle brightness analyzed by (A) conventional estimator and (C) corrected estimator. Dependence of average photon count on the relative error with different particle brightness analyzed by (B) conventional estimator and (D) corrected estimator. Insets in (C) and (D) show the magnified plots.

B_{corr} is defined as the transposed and substituted equation of $E[B]$. The second term in Eq. (9) at right-hand side is transposed to the left-hand side, and estimator B is substituted into the transposed true value. In fact, B_{corr} is still a biased estimator, but it is less biased compared to B . Comparing Eqs. (9) and (12), the influence from the second term in Eq. (9) is vanished, but that from the third term still remains. Figs. 6C and 6D show the improvement by the correction. The bias in expected value is clearly reduced here. Further correction can be implemented to reduce the influence from the third term in Eq. (9). This influence is remarkable when the average photon count is less than 1. The bias in low average photon count has been reported even though the background intensity is low (Youker and Teng 2014) (Gambin et al. 2016) (Fukushima et al. 2018). However, the bias correction

needs to estimate third sample raw moment, which makes the precision low. N&B analysis users are suggested to confirm the optimal range of average photon count and frame number for quantitative measurements.

3.4.4 Non-fluorescent State of Fluorescent Proteins

Variation in Normalized Brightness of Tandem Dimer

Theoretically, the normalized brightness of the tandem dimer should be 2, but a variation in this value is also reported (1.5-2.0). A value below 2 suggests that some fluorescent proteins are in a non-

Table 1. Normalized Brightness Close to 2.0 (100% Fluorescent State)

Sample	Analysis Methods	Tandem monomer	Tandem dimer	Unit	Ratio	Reference
EGFP	PCH [1] and moment analysis	$4,000 \pm 300$	$7,800 \pm 508$	cpsm (counts per second per molecule)	-	(Chen et al. 2003)
EYFP	TIFCA	680 ± 50	1380 ± 80	cps	-	(Wu et al. 2009)
GPI-mEGFP	N&B analysis	0.103 ± 0.004	0.205 ± 0.006	counts/molecule \times dwell time	-	(Zamai et al. 2019)
GFP	PCH [1]	-	-	-	~ 2	(Slaughter et al. 2007)
mEGFP	PCH [1]	-	-	-	~ 2	(Huet et al. 2010)
EGFP	FCS	-	-	-	2	(Foo et al. 2012)

[1] Photon counting histogram (Chen et al. 1999).

Table 2. Normalized Brightness Lower than 2.0 (Presence of a non-fluorescence State)

Sample	Analysis Methods	Tandem monomer	Tandem dimer	Unit	Ratio	Reference
mEGFP	N&B analysis or FCS	-	-	-	1.69 ± 0.05	(Dunsing et al. 2018)
mEYFP	same as above	-	-	-	1.63 ± 0.05	Same as above
mCherry	same as above	-	-	-	1.41 ± 0.04	Same as above
EGFP	FCS	-	-	-	[1]	(Vámosi et al. 2016)
EGFP	FCS and N&B analysis	-	-	-	[2]	(Fukushima et al. 2018)

[1] Estimated fluorescent probabilities were lower than 1.0. Probability decreased with increasing laser power.

[2] Normalized brightness was lower than the number of subunits in EGFP oligomers *in vivo*.

fluorescent state. Let us define fluorescent probability as a probability for a fluorescent protein to be fluorescent. We have listed some articles that reported the normalized or monomeric brightness and dimeric brightness in Tables 1 and 2. Here, the brightness unit and the sample vary according to the source article.

Possible Explanations for Non-fluorescent State of Proteins

There are several possible explanations for the non-fluorescent state of proteins: (1) Photophysical and photochemical processes, such as long-lived dark states (Widengren et al. 1999), multiple brightness state (Wu et al. 2009), blinking or flickering (Hendrix et al. 2008), and photobleaching (Hur et al. 2014) (2) Chromophore formation (protein maturation, incorrect folding of fluorescent protein) (Balleza et al. 2018) and (3) Unlabeled endogenous proteins

It has been reported that photophysical processes resulting from one-photon or and two-photon excitation are different. Hendrix et al. reported the presence of blinking in mCherry due to one-photon excitation (Hendrix et al. 2008). However, Wu et al. reported the absence of blinking due to two-photon excitation (Wu et al. 2009). Regarding chromophore formation, Dunsing et al. reported that there is negligible differences in the brightness between HEK, A549, CHO, and HeLa cells, and between 23°C and 37°C (Dunsing et al. 2018). Foo et al. used FCS and reported that cycloheximide treatment increased the fluorescent probability in mCherry (Foo et al. 2012). This indicates that a fraction of mCherry had not matured. These reports suggest that the normalized brightness for tandem dimer is not always 2.

Subunit counting (Ulbrich and Isacoff 2007)(Das et al. 2007) is a method to estimate the number of subunits in a complex. It observes stepwise photobleaching and count the number of the steps. The photobleaching in each fluorescent protein occurs independently. Subunit counting indicate the following fluorescent probability: 79.5% for EGFP tagged CNG channel (Ulbrich and Isacoff 2007), 80% for Kv4.3-EGFP (Zhou et al. 2015), 78% for GFP-ASIC1a, and 77% for GFP-ASIC2a (Bartoi et al. 2014).

Correction for Non-fluorescent State of Proteins

If the fluorescent probability for a protein is assumed to be constant, a simple correction method can be used (Vámosi et al. 2016)(Dunsing et al. 2018). This method assumes two states of the protein; fluorescent state (on) and non-fluorescent state (off). It also assumes that the number of fluorescent subunits in an oligomer follows binomial distribution. Let p be the fluorescent probability, and B_s be the apparent brightness for one component system that is comprised of oligomers with s subunits (for example, B_1 is apparent brightness for monomer and B_2 is that for tandem dimer). The apparent brightness with non-fluorescent state can be written as following (Vámosi et al. 2016):

$$B_s = \{1 + (s - 1)p\}\gamma_2\varepsilon_1, \quad (14)$$

$$\frac{B_s}{B_1} = 1 + (s - 1)p, \quad (15)$$

where, ε_1 is particle brightness for a monomer subunit. $B_1 = \gamma_2\varepsilon_1$ and normalized brightness $B_s/B_1 = s$ for $p = 1.0$. Fig. 7 shows the dependence of number of subunits on the normalized brightness with different fluorescent probabilities. The normalized brightness increases linearly with the number of subunits, and the slope of the line is smaller in low fluorescent probability. The fluorescent probability can be determined from independent reference measurements for one-component system, and estimated number of subunits can be corrected (Dunsing et al. 2018). Vamosi et al. reported that fluorescent probability depends on pH and laser power (Vámosi et al. 2016). Dunsing et al. confirmed that corrected number of subunits provides better estimation by using dimeric and trimeric Influenza A virus HA protein variants and 12-meric E. Coli GlnA, respectively (Dunsing et al. 2018).

3.5 Comparison with other techniques

FCS coupled with fast frame rate camera, such as electron-multiplied charge-coupled device (EMCCD), is called Imaging FCS (Kannan et al. 2006) (Bag and Wohland 2014). This technique enables a spatially simultaneous measurement of fluorescence intensity over time. Imaging FCS determines not only concentration and brightness distribution but also the diffusion time by implementing autocorrelation analysis at each pixel. However, its applicability is limited to slow-diffusing molecules, such as membrane binding protein. A necessary condition for autocorrelation analysis is that frame time must be sufficiently smaller than the diffusion time. In EMCCD, frame time is restricted to milliseconds order. In contrast, the diffusion time of EGFP is several hundred microseconds. Therefore, it is difficult to apply this method to EGFP labeled soluble protein unless the diffusion time of the labeled protein is sufficiently long. An advantage of Imaging FCS technique as compared to N&B analysis is that the former facilitates the visualization of diffusion time distribution, and helps to distinguish diffusion modes on cellular membrane (Wawrezynieck et al. 2005). The FCS diffusion law calculates the dependence of spatial scale on diffusion coefficient, and estimates the contribution from the diffusion mode, free diffusion, raft partitioning, and meshwork.

Time-integrated multipoint moment analysis (TIMMA) (Oh et al. 2011) is an application of N&B analysis and TIFCA. TIMMA determines the distribution of concentration, brightness, and diffusion time. Oh et al. used a stationary spinning disk confocal microscope equipped with an EMCCD, an acousto-optic tunable filter (AOTF), and a 50/50 beam splitter. They used the beam splitter to divide the signal into two parts. In EMCCD, the frame time primarily consists of sampling time (exposure time) and readout time. They measured the fluorescence signal with different sampling times to

estimate the average and covariance. TIFCA facilitates the measurement of the fluorescence signal with a longer sampling time and determination of diffusion time. Oh et al. demonstrated that TIMMA enables the measurement of soluble EGFP. It is difficult to measure soluble EGFP in Imaging FCS implemented with an EMCCD. The long readout time of EMCCD hampers the application. On the contrary, a necessary condition to apply the basic N&B analysis theory is to reduce the sampling time as compared to the diffusion time (see Sec. 3.1). Consequently, it can be applied even if the readout time is long.

3.6 Software

Nolan et al. described software for N&B analysis in their article (Nolan et al. 2017b).

3.7 Simulations

Photon count images were numerically simulated by using Microsoft Visual Studio Community 2017 version 15.9.10 (Microsoft, USA). All programs were written in Visual C++. Here, we assumed that photon count is a random variable following the product of two Poisson distribution along with a uniform illumination ($\gamma_r = 1$). The photon counts were simulated with a sampling time of 10 μ s. The frame size of simulated images was 128 \times 128, and the brightness map was obtained in the same size. An average and a standard error of relative error were estimated from the brightness map. For Fig. 6A, photon count images were simulated with a fixed true particle number ($n = 20$) and different true particle brightness ($\epsilon = 20, 5, 2, \text{ and } 1$ kHz/particle), and they were analyzed with different frame numbers ($m = 100, 200, 300, 400, 500, 700, \text{ and } 1,000$). For Fig. 6B, photon count images were simulated with different average photon count ($\epsilon_1 n_1 = 0.1, 0.2, 0.4, 1, 2, 4$ and 10 counts/sampling time) and different true particle brightness ($\epsilon = 20, 5, 2, \text{ and } 1$ kHz/particle), and they were analyzed with fixed frame number ($m = 100$). In Figs. 6A and 6B, each plot is obtained from independent simulations. In Fig. 6C and 6D, photon count images for each plot in Fig. 6A and 6B are analyzed with Eq. (11).

3.8 Conclusion

N&B analysis facilitates the determination of apparent brightness per pixel using fluorescence image series. This brightness is defined as the emitted photon count from a single particle, and it reflects the dynamic oligomer formation of protein. Therefore, it helps in visualizing the spatially heterogeneous oligomeric state of diffusing particle over time in a living cell. However, N&B analysis does not resolve multiple brightness components. In addition, apparent brightness is easy to be biased by several factors, such as improper sampling and lag time, background intensity, non-stationary intensity, detector dead time and afterpulse, and insufficient frame number. Even if all these biases are removed,

normalized brightness does not reflect the oligomeric state (the number of subunits in complex) directly in the presence of non-fluorescent state. These facts suggest that brightness calibration must be performed for each experiment. Otherwise, the experimental results may not be reliable.

N&B analysis has the potential to enhance the understanding of the controlling mechanism in the protein function, especially in signal transduction and neurodegenerative diseases. Moreover, N&B analysis coupled with time-integrated fluorescence cumulant analysis (TIFCA) can help in determining the diffusion time by measurements at different sampling times. Future advancement may help in analyzing other kinetics that are slower than diffusion, such as quenching affected by circumstance.

3.9 Supplementary Information 1

We evaluate the dependence of relative error on frame number. Suppose that we obtain m images with a sampling time T_{sampling} by fluorescence microscopy. Let X_i ($i = 1, 2, 3, \dots, m$) be independent and identically distributed random variables with expected photon count value equal to μ for in i^{th} image at one pixel. We assume that the number of fluorescent particles in a measurement volume does not change during the sampling time. We define first sample raw moment \bar{X} (sample mean) and second sample raw moment \bar{X}^2 as follows:

$$\bar{X} := \frac{1}{m} \sum_{i=1}^m X_i, \quad (\text{S1.1})$$

$$\bar{X}^2 := \frac{1}{m} \sum_{i=1}^m X_i^2. \quad (\text{S1.2})$$

Sample variance can be expressed as follows:

$$\frac{1}{m} \sum_{i=1}^m (X_i - \bar{X})^2 = \bar{X}^2 - \bar{X}^2. \quad (\text{S1.3})$$

The photon count X_i can be written as the sum of first raw moment μ (population mean) and instantaneous fluctuation around the first raw moment ΔX_i , i.e.

$$X_i = \mu + \Delta X_i. \quad (\text{S1.4})$$

Since the expectation value of the photon count is similar to the first raw moment ($E[X] = \mu$), the expectation value of the instantaneous fluctuation becomes 0 ($E[\Delta X] = 0$). Substituting Eq. (S1.4) into Eqs. (S1.1) and (S1.2), we get

$$\bar{X} = \mu + \overline{\Delta X}, \quad (\text{S1.5})$$

$$\overline{X^2} = \mu^2 + 2\mu\overline{\Delta X} + \overline{\Delta X^2}, \quad (\text{S1.6})$$

where,

$$\overline{\Delta X} := \frac{1}{m} \sum_{i=1}^m \Delta X_i, \quad (\text{S1.7})$$

$$\overline{\Delta X^2} := \frac{1}{m} \sum_{i=1}^m \Delta X_i^2. \quad (\text{S1.8})$$

The average instantaneous fluctuation ($\overline{\Delta X}$) can be removed by considering large samples (m). In other words, the expectation value of $\overline{\Delta X}$ is 0 ($E[\overline{\Delta X}] = 0$). Next, we consider the brightness estimator, which can be defined from Eqs. (S1.5) and (S1.6) as follows:

$$\begin{aligned} B &:= \frac{\overline{X^2} - \bar{X}^2 - \bar{X}}{\bar{X}} \\ &= \frac{\overline{\Delta X^2} - \overline{\Delta X}^2}{\mu + \overline{\Delta X}} - 1 \\ &= \frac{1}{\mu} \frac{\overline{\Delta X^2} - \overline{\Delta X}^2}{1 + \frac{\overline{\Delta X}}{\mu}} - 1. \end{aligned} \quad (\text{S1.9})$$

Taylor series expansion of the denominator up to second order around 0 gives

$$\frac{1}{1 + \frac{\overline{\Delta X}}{\mu}} = 1 - \frac{\overline{\Delta X}}{\mu} + \left(\frac{\overline{\Delta X}}{\mu}\right)^2 - O\left(\left(\frac{\overline{\Delta X}}{\mu}\right)^3\right). \quad (\text{S1.10})$$

Therefore,

$$B = \frac{1}{\mu} (\overline{\Delta X^2} - \overline{\Delta X}^2) \left(1 - \frac{\overline{\Delta X}}{\mu} + \left(\frac{\overline{\Delta X}}{\mu}\right)^2 - O\left(\left(\frac{\overline{\Delta X}}{\mu}\right)^3\right) \right) - 1. \quad (\text{S1.11})$$

The expectation value of brightness estimator is

$$\begin{aligned}
E[B] &= \frac{1}{\mu} \left\{ \left(E[\overline{\Delta X^2}] - E[\overline{\Delta X^2}] \right) - \frac{1}{\mu} \left(E[\overline{\Delta X \Delta X^2}] - E[\overline{\Delta X^3}] \right) \right. \\
&\quad \left. + \frac{1}{\mu^2} \left(E[\overline{\Delta X^2 \Delta X^2}] - E[\overline{\Delta X^4}] \right) + \dots \right\} \\
&= \frac{1}{\mu} \left\{ \left(1 - \frac{1}{m} \right) E[\Delta X^2] - \frac{1}{\mu} \frac{1}{m} \left(1 - \frac{1}{m} \right) E[\Delta X^3] + \frac{1}{\mu^2} \frac{1}{m^2} \left(1 - \frac{1}{m} \right) E[\Delta X^4] \right. \\
&\quad \left. + \frac{1}{\mu^2} \frac{1}{m} \left(1 - \frac{1}{m} \right) (E[\Delta X^2])^2 + \dots \right\} - 1 \tag{S1.12} \\
&= \frac{E[\Delta X^2]}{\mu} - 1 - \frac{1}{m} \left\{ \frac{E[\Delta X^2]}{\mu} + \frac{1}{\mu} \left(\frac{E[\Delta X^3]}{\mu} - \left(\frac{E[\Delta X^2]}{\mu} \right)^2 \right) \right\} + o\left(\left(\frac{1}{m} \right)^2 \right) \\
&= \frac{\kappa_{[2]}}{\kappa_{[1]}} - \frac{1}{m} \left(\frac{\kappa_{[2]}}{\kappa_{[1]}} + 1 + \frac{1}{\kappa_{[1]}} \left(\frac{\kappa_{[3]}}{\kappa_{[1]}} - \left(\frac{\kappa_{[2]}}{\kappa_{[1]}} \right)^2 + \frac{\kappa_{[2]}}{\kappa_{[1]}} \right) \right) + o\left(\left(\frac{1}{m} \right)^2 \right).
\end{aligned}$$

where, we used the solution obtained in Supplementary Information 2 shown below. For one component system, the expectation value of brightness estimator is

$$E[B] = \gamma_2 \varepsilon_1 - \frac{1}{m} (\gamma_2 \varepsilon_1 + 1) - \frac{1}{m} \frac{1}{\varepsilon_1 n_1} (\gamma_3 \varepsilon_1^2 - \gamma_2^2 \varepsilon_1^2 + \gamma_2 \varepsilon_1) + o\left(\left(\frac{1}{m} \right)^2 \right) \tag{S1.13}$$

3.10 Supplementary Information 2

We consider the expected values in the first row of Eq. (S1.12). The expected values are written in terms of central moments ($E[\Delta X]$, $E[\Delta X^2]$, $E[\Delta X^3]$, $E[\Delta X^4]$) as follows:

$$\begin{aligned}
E[\overline{\Delta X^2}] &= \frac{1}{m} E \left[\sum_{i=1}^m \Delta X_i^2 \right] = \frac{1}{m} \sum_{i=1}^m E[\Delta X_i^2] \\
&= E[\Delta X^2], \tag{S2.1}
\end{aligned}$$

$$\begin{aligned}
E[\overline{\Delta X^2}] &= \frac{1}{m^2} E \left[\left(\sum_{i=1}^m \Delta X_i \right)^2 \right] = \frac{1}{m^2} E \left[\left(\sum_{i=1}^m \Delta X_i \right) \left(\sum_{j=1}^m \Delta X_j \right) \right] \\
&= \frac{1}{m^2} E \left[\sum_{i=1}^m \sum_{j=1}^m \Delta X_i \Delta X_j \right] \tag{S2.2}
\end{aligned}$$

$$\begin{aligned}
 &= \frac{1}{m^2} E \left[\sum_{i=1}^m \Delta X_i^2 + 2 \sum_{i=1}^m \sum_{j=1 < i}^m \Delta X_i \Delta X_j \right] \\
 &= \frac{1}{m^2} \sum_{i=1}^m E[\Delta X_i^2] + \frac{2}{m^2} \sum_{i=1}^m \sum_{j=1 < i}^m E[\Delta X_i \Delta X_j] \\
 &= \frac{1}{m} E[\Delta X^2] + \frac{2}{m^2} \frac{m^2 - m}{2} E[\Delta X]^2 = \frac{1}{m} E[\Delta X^2],
 \end{aligned}$$

where, we used the following facts: (1) We considered that $A_i B_j$ is the element of $m \times m$ matrix, and $\sum_{i=1}^m \sum_{j=1}^m A_i B_j$ is the summation of all matrix elements. The summation of matrix elements is separated into summation of diagonal and non-diagonal elements. (2) We assume that C and D are independent random variables, $E[CD] = E[C]E[D]$. (3) $E[\Delta X] = 0$.

Similarly, we have

$$E[\overline{\Delta X} \overline{\Delta X^2}] = \frac{1}{m} E[\Delta X^3], \quad (\text{S2.3})$$

$$E[\overline{\Delta X^3}] = \frac{1}{m^2} E[\Delta X^3], \quad (\text{S2.4})$$

$$E[\overline{\Delta X^2} \overline{\Delta X^2}] = \frac{1}{m^2} E[\Delta X^4] + \frac{1}{m} \left(1 - \frac{1}{m}\right) (E[\Delta X^2])^2, \quad (\text{S2.5})$$

$$E[\overline{\Delta X^4}] = \frac{1}{m^3} E[\Delta X^4] + \frac{1}{m^2} \left(1 - \frac{1}{m}\right) (E[\Delta X^2])^2. \quad (\text{S2.6})$$

The expectation value of X and central moment are written in terms of cumulants as follows (Abdollah-Nia 2016):

$$E[X] = \mu = \kappa_1, \quad (\text{S2.7})$$

$$E[\Delta X^2] = \kappa_2, \quad (\text{S2.8})$$

$$E[\Delta X^3] = \kappa_3. \quad (\text{S2.9})$$

In addition, cumulants are written in terms of factorial cumulants as follows:

$$\kappa_1 = \kappa_{[1]}, \quad (\text{S2.10})$$

$$\kappa_2 = \kappa_{[2]} + \kappa_{[1]}, \quad (\text{S2.11})$$

$$\kappa_3 = \kappa_{[3]} + 3\kappa_{[2]} + \kappa_{[1]}. \quad (\text{S2.12})$$

k^{th} factorial cumulants of photon count is expressed in terms of particle brightness ε , particle number n , and γ -factor as follows (Müller 2004):

$$\kappa_{[k]} = \gamma_k \sum_{l=1}^c \varepsilon_l^k n_l, \quad (\text{S2.13})$$

where,

$$\gamma_k := \frac{\int_V (\overline{\text{PSF}}(\vec{r}))^k d\vec{r}}{\int_V \overline{\text{PSF}}(\vec{r}) d\vec{r}}, \quad (\text{S2.14})$$

$\overline{\text{PSF}}(\vec{r})$ is normalized point spread function at position \vec{r} with $\overline{\text{PSF}}(0) = 1$, V is measurement volume.

3.11 References

- Abdollah-Nia, F. (2016) Cumulant-based formulation of higher-order fluorescence correlation spectroscopy. arXiv.org e-Print Arch.
- Abdollah-Nia, F., Gelfand, M.P., Van Orden, A. (2017a) Artifact-Free and Detection-Profile-Independent Higher-Order Fluorescence Correlation Spectroscopy for Microsecond-Resolved Kinetics. 1. Multidetector and Sub-Binning Approach. *J. Phys. Chem. B* 121:2373–2387. <https://doi.org/10.1021/acs.jpcc.7b00407>
- Abdollah-Nia, F., Gelfand, M.P., Van Orden, A. (2017b) Artifact-Free and Detection-Profile-Independent Higher-Order Fluorescence Correlation Spectroscopy for Microsecond-Resolved Kinetics. 2. Mixtures and Reactions. *J. Phys. Chem. B* 121:2388–2399. <https://doi.org/10.1021/acs.jpcc.7b00408>
- Bag, N., Wohland, T. (2014) Imaging Fluorescence Fluctuation Spectroscopy: New Tools for Quantitative Bioimaging. *Annu. Rev. Phys. Chem.* 65:225–248. <https://doi.org/10.1146/annurev-physchem-040513-103641>
- Balleza, E., Kim, J.M., Cluzel, P. (2018) Systematic characterization of maturation time of fluorescent proteins in living cells. *Nat. Methods* 15:47–51. <https://doi.org/10.1038/nmeth.4509>
- Bartoi, T., Augustinowski, K., Polleichtner, G., Grunder, S., Ulbrich, M.H. (2014) Acid-sensing ion channel (ASIC) 1a/2a heteromers have a flexible 2:1/1:2 stoichiometry. *Proc. Natl. Acad. Sci.* 111:8281–8286. <https://doi.org/10.1073/pnas.1324060111>
- Caccia, M., Camozzi, E., Collini, M., Zaccolo, M., Chirico, G. (2005) Photon Moment Analysis in Cells in the Presence of Photo-Bleaching. *Appl. Spectrosc.* 59:227–236. <https://doi.org/10.1366/0003702053084981>

- Campbell, L. (1992) Afterpulse measurement and correction. *Rev. Sci. Instrum.* 63:5794–5798.
<https://doi.org/10.1063/1.1143365>
- Chen, Y., Johnson, J., Macdonald, P., Wu, B., Mueller, J.D. (2010) Observing Protein Interactions and Their Stoichiometry in Living Cells by Brightness Analysis of Fluorescence Fluctuation Experiments. In: *Single Molecule Tools: Fluorescence Based Approaches, Part A*. Elsevier Inc., pp. 345–363
- Chen, Y., Müller, J.D., Ruan, Q., Gratton, E. (2002) Molecular Brightness Characterization of EGFP In Vivo by Fluorescence Fluctuation Spectroscopy. *Biophys. J.* 82:133–144.
[https://doi.org/10.1016/S0006-3495\(02\)75380-0](https://doi.org/10.1016/S0006-3495(02)75380-0)
- Chen, Y., Müller, J.D., So, P.T.C., Gratton, E. (1999) The Photon Counting Histogram in Fluorescence Fluctuation Spectroscopy. *Biophys. J.* 77:553–567. [https://doi.org/10.1016/S0006-3495\(99\)76912-2](https://doi.org/10.1016/S0006-3495(99)76912-2)
- Chen, Y., Wei, L.-N., Muller, J.D. (2003) Probing protein oligomerization in living cells with fluorescence fluctuation spectroscopy. *Proc. Natl. Acad. Sci.* 100:15492–15497.
<https://doi.org/10.1073/pnas.2533045100>
- Cutrale, F., Rodriguez, D., Hortigüela, V., Chiu, C.-L., Otterstrom, J., Mieruszynski, S., Seriola, A., Larrañaga, E., Raya, A., Lakadamyali, M., Fraser, S.E., Martinez, E., Ojosnegros, S. (2019) Using enhanced number and brightness to measure protein oligomerization dynamics in live cells. *Nat. Protoc.* 14:616–638. <https://doi.org/10.1038/s41596-018-0111-9>
- Dalal, R.B., Digman, M.A., Horwitz, A.F., Vetri, V., Gratton, E. (2008) Determination of particle number and brightness using a laser scanning confocal microscope operating in the analog mode. *Microsc. Res. Tech.* 71:69–81. <https://doi.org/10.1002/jemt.20526>
- Das, S.K., Darshi, M., Cheley, S., Wallace, M.I., Bayley, H. (2007) Membrane Protein Stoichiometry Determined from the Step-Wise Photobleaching of Dye-Labelled Subunits. *ChemBioChem* 8:994–999. <https://doi.org/10.1002/cbic.200600474>
- Digman, M.A., Dalal, R., Horwitz, A.F., Gratton, E. (2008) Mapping the Number of Molecules and Brightness in the Laser Scanning Microscope. *Biophys. J.* 94:2320–2332.
<https://doi.org/10.1529/biophysj.107.114645>
- Dusing, V., Luckner, M., Zühlke, B., Petazzi, R.A., Herrmann, A., Chiantia, S. (2018) Optimal fluorescent protein tags for quantifying protein oligomerization in living cells. *Sci. Rep.* 8:10634.
<https://doi.org/10.1038/s41598-018-28858-0>
- Elson, E.L., Magde, D. (1974) Fluorescence correlation spectroscopy. I. Conceptual basis and theory. *Biopolymers* 13:1–27. <https://doi.org/10.1002/bip.1974.360130102>
- Fang, Y.-S., Tsai, K.-J., Chang, Y.-J., Kao, P., Woods, R., Kuo, P.-H., Wu, C.-C., Liao, J.-Y., Chou, S.-C., Lin, V., Jin, L.-W., Yuan, H.S., Cheng, I.H., Tu, P.-H., Chen, Y.-R. (2014) Full-length TDP-43 forms toxic amyloid oligomers that are present in frontotemporal lobar dementia-TDP patients. *Nat. Commun.* 5:4824. <https://doi.org/10.1038/ncomms5824>

- Foo, Y.H., Naredi-Rainer, N., Lamb, D.C., Ahmed, S., Wohland, T. (2012) Factors affecting the quantification of biomolecular interactions by fluorescence cross-correlation spectroscopy. *Biophys. J.* 102:1174–1183. <https://doi.org/10.1016/j.bpj.2012.01.040>
- Fukushima, R., Yamamoto, J., Ishikawa, H., Kinjo, M. (2018) Two-detector number and brightness analysis reveals spatio-temporal oligomerization of proteins in living cells. *Methods* 140–141:161–171. <https://doi.org/10.1016/j.ymeth.2018.03.007>
- Gambin, Y., Polinkovsky, M., Francois, B., Giles, N., Bhumkar, A., Sieracki, E. (2016) Confocal Spectroscopy to Study Dimerization, Oligomerization and Aggregation of Proteins: A Practical Guide. *Int. J. Mol. Sci.* 17:655. <https://doi.org/10.3390/ijms17050655>
- Hendrix, J., Flors, C., Dedecker, P., Hofkens, J., Engelborghs, Y. (2008) Dark States in Monomeric Red Fluorescent Proteins Studied by Fluorescence Correlation and Single Molecule Spectroscopy. *Biophys. J.* 94:4103–4113. <https://doi.org/10.1529/biophysj.107.123596>
- Hendrix, J., Schrimpf, W., Höller, M., Lamb, D.C. (2013) Pulsed Interleaved Excitation Fluctuation Imaging. *Biophys. J.* 105:848–861. <https://doi.org/10.1016/j.bpj.2013.05.059>
- Hennen, J., Hur, K.-H., Saunders, C.A., Luxton, G.W.G., Mueller, J.D. (2017) Quantitative Brightness Analysis of Protein Oligomerization in the Nuclear Envelope. *Biophys. J.* 113:138–147. <https://doi.org/10.1016/j.bpj.2017.05.044>
- Hillesheim, L.N., Müller, J.D. (2003) The Photon Counting Histogram in Fluorescence Fluctuation Spectroscopy with Non-Ideal Photodetectors. *Biophys. J.* 85:1948–1958. [https://doi.org/10.1016/S0006-3495\(03\)74622-0](https://doi.org/10.1016/S0006-3495(03)74622-0)
- Huet, S., Avilov, S. V., Ferbitz, L., Daigle, N., Cusack, S., Ellenberg, J. (2010) Nuclear Import and Assembly of Influenza A Virus RNA Polymerase Studied in Live Cells by Fluorescence Cross-Correlation Spectroscopy. *J. Virol.* 84:1254–1264. <https://doi.org/10.1128/JVI.01533-09>
- Hur, K.-H., Macdonald, P.J., Berk, S., Angert, C.I., Chen, Y., Mueller, J.D. (2014) Quantitative Measurement of Brightness from Living Cells in the Presence of Photodepletion. *PLoS One* 9:e97440. <https://doi.org/10.1371/journal.pone.0097440>
- Hur, K.-H., Mueller, J.D. (2015) Quantitative Brightness Analysis of Fluorescence Intensity Fluctuations in *E. Coli*. *PLoS One* 10:e0130063. <https://doi.org/10.1371/journal.pone.0130063>
- Kannan, B., Har, J.Y., Liu, P., Maruyama, I., Ding, J.L., Wohland, T. (2006) Electron Multiplying Charge-Coupled Device Camera Based Fluorescence Correlation Spectroscopy. *Anal. Chem.* 78:3444–3451. <https://doi.org/10.1021/ac0600959>
- Kitamura, A., Kinjo, M. (2018) State-of-the-art fluorescence fluctuation-based spectroscopic techniques for the study of protein aggregation. *Int. J. Mol. Sci.* 19. <https://doi.org/10.3390/ijms19040964>
- Krmpot, A.J., Nikolić, S.N., Vitali, M., Papadopoulos, D.K., Oasa, S., Thyberg, P., Tisa, S., Kinjo, M., Nilsson, L., Gehring, W.J., Terenius, L., Rigler, R., Vukojević, V. (2015) Quantitative confocal fluorescence microscopy of dynamic processes by multifocal fluorescence correlation spectroscopy.

- In: *Advanced Microscopy Techniques IV; and Neurophotonics II*. OSA, Washington, D.C., p. 953600
- Macdonald, P., Johnson, J., Smith, E., Chen, Y., Mueller, J.D. (2013) Brightness Analysis. In: *Methods in Enzymology*. Elsevier Inc., pp. 71–98
- Macdonald, P.J., Chen, Yun, Wang, X., Chen, Yan, Mueller, J.D. (2010) Brightness Analysis by Z-Scan Fluorescence Fluctuation Spectroscopy for the Study of Protein Interactions within Living Cells. *Biophys. J.* 99:979–988. <https://doi.org/10.1016/j.bpj.2010.05.017>
- Melnykov, A. V., Hall, K.B. (2009) Revival of High-Order Fluorescence Correlation Analysis: Generalized Theory and Biochemical Applications. *J. Phys. Chem. B* 113:15629–15638. <https://doi.org/10.1021/jp906539k>
- Meseth, U., Wohland, T., Rigler, R., Vogel, H. (1999) Resolution of Fluorescence Correlation Measurements. *Biophys. J.* 76:1619–1631. [https://doi.org/10.1016/S0006-3495\(99\)77321-2](https://doi.org/10.1016/S0006-3495(99)77321-2)
- Müller, J.D. (2004) Cumulant Analysis in Fluorescence Fluctuation Spectroscopy. *Biophys. J.* 86:3981–3992. <https://doi.org/10.1529/biophysj.103.037887>
- Nolan, R., Alvarez, L.A.J., Elegheert, J., Iliopoulou, M., Jakobsdottir, G.M., Rodriguez-Muñoz, M., Aricescu, A.R., Padilla-Parra, S. (2017a) nandb—number and brightness in R with a novel automatic detrending algorithm. *Bioinformatics* 33:3508–3510. <https://doi.org/10.1093/bioinformatics/btx434>
- Nolan, R., Iliopoulou, M., Alvarez, L., Padilla-Parra, S. (2017b) Detecting protein aggregation and interaction in live cells: A guide to number and brightness. *Methods* :1–6. <https://doi.org/10.1016/j.ymeth.2017.12.001>
- O'Donnell, K.A. (1986) Correction of dead-time effects in photoelectric-counting distributions. *J. Opt. Soc. Am. A* 3:113. <https://doi.org/10.1364/JOSAA.3.000113>
- Oh, D., Zidovska, A., Xu, Y., Needleman, D.J. (2011) Development of Time-Integrated Multipoint Moment Analysis for Spatially Resolved Fluctuation Spectroscopy with High Time Resolution. *Biophys. J.* 101:1546–1554. <https://doi.org/10.1016/j.bpj.2011.08.013>
- Ojosnegros, S., Cutrale, F., Rodríguez, D., Otterstrom, J.J., Chiu, C.L., Hortigüela, V., Tarantino, C., Seriola, A., Mieruszynski, S., Martínez, E., Lakadamyali, M., Raya, A., Fraser, S.E. (2017) Eph-ephrin signaling modulated by polymerization and condensation of receptors. *Proc. Natl. Acad. Sci.* 114:13188–13193. <https://doi.org/10.1073/pnas.1713564114>
- Ossato, G., Digman, M.A., Aiken, C., Lukacsovich, T., Marsh, J.L., Gratton, E. (2010) A Two-Step Path to Inclusion Formation of Huntingtin Peptides Revealed by Number and Brightness Analysis. *Biophys. J.* 98:3078–3085. <https://doi.org/10.1016/j.bpj.2010.02.058>
- Pack, C., Saito, K., Tamura, M., Kinjo, M. (2006) Microenvironment and Effect of Energy Depletion in the Nucleus Analyzed by Mobility of Multiple Oligomeric EGFPs. *Biophys. J.* 91:3921–3936. <https://doi.org/10.1529/biophysj.105.079467>

- Palmer, A.G., Thompson, N.L. (1987) Molecular aggregation characterized by high order autocorrelation in fluorescence correlation spectroscopy. *Biophys. J.* 52:257–270. [https://doi.org/10.1016/S0006-3495\(87\)83213-7](https://doi.org/10.1016/S0006-3495(87)83213-7)
- Palmer, A.G., Thompson, N.L. (1989a) High-order fluorescence analysis of model protein clusters. *Proc. Natl. Acad. Sci. USA* 86:6148–6152
- Palmer, A.G., Thompson, N.L. (1989b) Intensity dependence of high order autocorrelation functions in fluorescence correlation spectroscopy. *Rev. Sci. Instrum.* 60:624–633
- Petráček, Z., Schwille, P. (2008) Photobleaching in Two-Photon Scanning Fluorescence Correlation Spectroscopy. *ChemPhysChem* 9:147–158. <https://doi.org/10.1002/cphc.200700579>
- Qian, H., Elson, E.L. (1990a) On the analysis of high order moments of fluorescence fluctuations. *Biophys. J.* 57:375–380. [https://doi.org/10.1016/S0006-3495\(90\)82539-X](https://doi.org/10.1016/S0006-3495(90)82539-X)
- Qian, H., Elson, E.L. (1990b) Distribution of molecular aggregation by analysis of fluctuation moments. *Proc. Natl. Acad. Sci.* 87:5479–5483. <https://doi.org/10.1073/pnas.87.14.5479>
- Saffarian, S., Elson, E.L. (2003) Statistical Analysis of Fluorescence Correlation Spectroscopy: The Standard Deviation and Bias. *Biophys. J.* 84:2030–2042. [https://doi.org/10.1016/S0006-3495\(03\)75011-5](https://doi.org/10.1016/S0006-3495(03)75011-5)
- Sanchez-Andres, A., Chen, Y., Müller, J.D. (2005) Molecular Brightness Determined from a Generalized Form of Mandel's Q-Parameter. *Biophys. J.* 89:3531–3547. <https://doi.org/10.1529/biophysj.105.067082>
- Schätzel, K., Drewel, M., Stimac, S. (1988) Photon Correlation Measurements at Large Lag Times: Improving Statistical Accuracy. *J. Mod. Opt.* 35:711–718. <https://doi.org/10.1080/09500348814550731>
- Skinner, J.P., Chen, Y., Müller, J.D. (2008) Fluorescence Fluctuation Spectroscopy in the Presence of Immobile Fluorophores. *Biophys. J.* 94:2349–2360. <https://doi.org/10.1529/biophysj.107.115642>
- Slaughter, B.D., Schwartz, J.W., Li, R. (2007) Mapping dynamic protein interactions in MAP kinase signaling using live-cell fluorescence fluctuation spectroscopy and imaging. *Proc. Natl. Acad. Sci.* 104:20320–20325. <https://doi.org/10.1073/pnas.0710336105>
- Thompson, N.L. (1991) Fluorescence Correlation Spectroscopy. In: Lakowics, J.R. (Ed.), *Topics in Fluorescence Spectroscopy, Volume 1 Techniques*. Plenum Press, pp. 337–378
- Trullo, A., Corti, V., Arza, E., Caiolfa, V.R., Zamai, M. (2013) Application limits and data correction in number of molecules and brightness analysis. *Microsc. Res. Tech.* 76:1135–1146. <https://doi.org/10.1002/jemt.22277>
- Ulbrich, M.H., Isacoff, E.Y. (2007) Subunit counting in membrane-bound proteins. *Nat. Methods* 4:319–321. <https://doi.org/10.1038/nmeth1024>
- Unruh, J.R., Gratton, E. (2008) Analysis of Molecular Concentration and Brightness from Fluorescence Fluctuation Data with an Electron Multiplied CCD Camera. *Biophys. J.* 95:5385–5398.

- <https://doi.org/10.1529/biophysj.108.130310>
- Vámosi, G., Mücke, N., Müller, G., Krieger, J.W., Curth, U., Langowski, J., Tóth, K. (2016) EGFP oligomers as natural fluorescence and hydrodynamic standards. *Sci. Rep.* 6:33022. <https://doi.org/10.1038/srep33022>
- van Kempen, G.M., van Vliet, L.J. (2000) Mean and variance of ratio estimators used in fluorescence ratio imaging. *Cytometry* 39:300–5
- Wawrezinieck, L., Rigneault, H., Marguet, D., Lenne, P.-F. (2005) Fluorescence Correlation Spectroscopy Diffusion Laws to Probe the Submicron Cell Membrane Organization. *Biophys. J.* 89:4029–4042. <https://doi.org/10.1529/biophysj.105.067959>
- Widengren, J., Mets, Ü., Rigler, R. (1999) Photodynamic properties of green fluorescent proteins investigated by fluorescence correlation spectroscopy. *Chem. Phys.* 250:171–186. [https://doi.org/10.1016/S0301-0104\(99\)00255-4](https://doi.org/10.1016/S0301-0104(99)00255-4)
- Wu, B., Chen, Y., Müller, J.D. (2009) Fluorescence Fluctuation Spectroscopy of mCherry in Living Cells. *Biophys. J.* 96:2391–2404. <https://doi.org/10.1016/j.bpj.2008.12.3902>
- Wu, B., Müller, J.D. (2005) Time-Integrated Fluorescence Cumulant Analysis in Fluorescence Fluctuation Spectroscopy. *Biophys. J.* 89:2721–2735. <https://doi.org/10.1529/biophysj.105.063685>
- Yamamoto, J., Mikuni, S., Kinjo, M. (2018) Multipoint fluorescence correlation spectroscopy using spatial light modulator. *Biomed. Opt. Express* 9:5881. <https://doi.org/10.1364/BOE.9.005881>
- Youker, R.T., Teng, H. (2014) Measuring protein dynamics in live cells: protocols and practical considerations for fluorescence fluctuation microscopy. *J. Biomed. Opt.* 19:090801. <https://doi.org/10.1117/1.JBO.19.9.090801>
- Zamai, M., Trullo, A., Giordano, M., Corti, V., Arza Cuesta, E., Francavilla, C., Cavallaro, U., Caiolfa, V.R. (2019) Number and brightness analysis reveals that NCAM and FGF2 elicit different assembly and dynamics of FGFR1 in live cells. *J. Cell Sci.* 132:jcs220624. <https://doi.org/10.1242/jcs.220624>
- Zhou, J., Tang, Y., Zheng, Q., Li, M., Yuan, T., Chen, L., Huang, Z., Wang, K. (2015) Different KChIPs Compete for Heteromultimeric Assembly with Pore-Forming Kv4 Subunits. *Biophys. J.* 108:2658–2669. <https://doi.org/10.1016/j.bpj.2015.04.024>

Chapter 4

Reduction of Dead Time Effect by Estimating Covariance

4.1 Abstract

Number and brightness analysis (N&B) is a useful tool for the simultaneous visualization of protein oligomers and their localization, with single-molecule sensitivity. N&B determines particle brightness (fluorescence intensity per particle) and maps the spatial distribution of fluorescently labeled proteins by performing statistical analyses of the image series obtained using laser scanning microscopy. The brightness map reveals presence of the oligomers of the targeted protein and their distribution in living cells. However, even when corrections are applied, conventional N&B is affected by afterpulsing, shot noise, thermal noise, dead time, and overestimation of particle brightness when the concentration of the fluorescent particles changes during measurement.

The drawbacks of conventional N&B can be circumvented by using two detectors, a novel approach that we henceforth call two-detector number and brightness analysis (TD-N&B), and introducing a linear regression of fluorescence intensity. This statistically eliminates the effect of noise from the detectors, and ensures that the correct particle brightness is obtained. Our method was theoretically assessed by numerical simulations and experimentally validated using a dilution series of purified enhanced green fluorescent protein (EGFP), EGFP tandem oligomers in cell lysate, and EGFP tandem oligomers in living cells. Furthermore, this method was used to characterize the complex process of ligand-induced glucocorticoid receptor dimerization and their translocation to the cell nucleus in live cells. Our method can be applied to other oligomer-forming proteins in cell signaling, or to aggregations of proteins such as those that cause neurodegenerative diseases.

4.2 Introduction

Upon stimulation with specific ligands, many receptors change their localization and oligomeric states. It is, therefore, important to characterize protein localization and oligomerization in live cells.

Fluorescence microscopy coupled with fluorescence fluctuation spectroscopy (FFS) is suitable for monitoring the localization and oligomerization of proteins in living cells. Fluorescence Correlation Spectroscopy (FCS) [1,2], the longest used FFS, can be used to determine the number of particles in the measurement volume, the diffusion coefficient, and the particle brightness (fluorescence intensity per one particle), which can be used to deduce the oligomeric state of the target particles. However, it is difficult to detect long-distance changes in protein localization using FCS because there is usually

only one point of measurement. Imaging-based FFS techniques have been developed to overcome this drawback. They include image correlation spectroscopy (ICS) [3], raster image correlation spectroscopy (RICS) [4,5], temporal image correlation spectroscopy (TICS) [6], and imaging FCS [7]. ICS determines the radius of the particles, the number of particles in a field of view, and the particle brightness. RICS can measure tiny and fast-diffusing particles/molecules, including organic fluorescent dyes, and small proteins. However, the spatial resolution of RICS is always lower than the resolution of the original image, owing to the correlation calculation between adjacent pixels. For example, when we get original images as 512×512 and the correlation is calculated between adjacent 16×16 pixels, the spatial resolution of the result becomes 32×32 . TICS is useful for measuring relatively slow-diffusing particles such as membrane proteins, but is not suitable for fast-diffusing particles because of the low frame rate of confocal imaging. Imaging FCS, which is similar to TICS, uses an electron multiplying charge-coupled device (EMCCD) or a complementary metal oxide semiconductor (CMOS) for image acquisition.

Number and brightness analysis (N&B) is another FFS technique. It produces a map of the number of particles and the particle brightness [8]. Spatial resolution in N&B is the same as that achieved using a laser scanning microscope (LSM). N&B can be applied to fast-diffusing particles, such as diffusing protein in living cells, compared to TICS and Imaging FCS. For TICS and Imaging FCS, frame time (time taken to obtain a frame and lag time of each frame) is important and required to be much shorter than the characteristic decay time of the fluctuating particles (residence time of particles in measurement volume at a pixel) for calculation of correlation in the temporal domain. This restricts their application to measuring slow-diffusing particles, such as membrane proteins. On the other hand, for N&B, frame time is not required to be shorter than the characteristic decay time of the fluctuating particles. However, pixel dwell time (time taken to obtain a pixel value) is required to be much shorter than the characteristic decay time of the fluctuating particles for N&B [8]. N&B does not analyze the temporal intensity fluctuation during crossing of the particles through the measurement volume, but analyze the variance of instantaneous intensity depending on number of particles in measurement volume during shorter time than characteristic decay time (corresponding to diffusion time in FCS). Therefore the lag time of N&B is not effective but only pixel dwell time is effective, and N&B can be applied to relatively fast-diffusing particles such as diffusing protein in living cells. Nevertheless, N&B does not determine the characteristic decay time or diffusion coefficient unlike TICS and Imaging FCS. N&B has been used in several studies, including a distribution analysis of the oligomeric receptor protein ErbB1, before and after stimulation with epidermal growth factor (EGF) [9]. This study revealed the ligand-independent dimerization of ErbB1 when the density of ErbB1 is sufficiently high and the conversion of ErbB1 into its higher oligomeric state after the stimulation. Another example of the use of N&B is for the investigation of the formation of huntingtin peptide inclusions in degenerative neurological disorders [10]. This study revealed a time-dependent formation of

inclusions and a two-step pathway to inclusion formation. Yet another example of the use of N&B is for the investigation of dynamin-2 oligomer formation in HIV-1 infection [11]. This study revealed that the low oligomeric state of dynamin-2 was associated with the HIV envelope protein. N&B is useful for investigating the diffusing particles in living cells and for resolving the particles spatially. Currently, it is impossible to predict when and where oligomers or inclusions will form. N&B enables simultaneous measurements to be carried out over relatively wide fields in living cells. Therefore, it is expected that N&B will be used widely for the study of oligomer or aggregation formation. However, the accuracy of conventional N&B is not adequate and the results are easily affected by sample concentration, necessitating correction for detector dead time [12,13] and correction for noise. Furthermore, conventional N&B overestimates particle brightness when the concentration of the fluorescent particles is changed (Supplementary Note S1) or fluorescence intensity is decreased by photobleaching during measurement [14].

In this study, we developed an improved N&B, called two-detector N&B (TD-N&B), which overcomes the problems associated with conventional N&B without any mathematical corrections. We achieved improvements by eliminating noise effects from detectors, by incorporating a two-detector optical system, and by introducing linear regression to compensate for the change in fluorescence intensity. Furthermore, we demonstrated the feasibility of our method quantitatively by analyzing enhanced green fluorescent protein (EGFP) dilution series, and by investigating EGFP tandem oligomers in cell lysate and living cells. Finally, we monitored the dimerization of EGFP-tagged glucocorticoid receptors (EGFP-GR), as a cell signaling process. The nuclear translocation and dimerization of GR were visualized from a time series of the brightness map of EGFP-GR, which was obtained by TD-N&B. This is the first step towards using quantitative imaging to elucidate dynamic GR mechanisms. Moreover, our method can be applied to other oligomer-forming proteins, or to aggregation of proteins, such as those that cause neurodegenerative diseases, which are difficult to visualize in living cells or whole organisms using biochemical methods and molecular biology.

4.3 Methods

4.3.1 Two-detector number and brightness analysis (TD-N&B)

The experimental setup of the TD-N&B system is shown in Figure 1A. Two image series were obtained simultaneously using a LSM and two avalanche photodiodes (APDs) operating in the photon counting mode (Figure 1B). We used the APDs to detect fluorescence, but it is also possible to use a detector operating in the analog mode or pseudo-photon counting mode with calibration for image acquisition [15]. The calibration includes: the offset; the S factor, which converts photon counts into digital data, and the read-out variance of the detector. Regardless of the operating mode, the pixel dwell time must be short, compared to the characteristic decay time of the particles in the measurement

volume to detect the fluctuation in the number of particles, which is a necessary condition for image acquisition. In our condition, pixel dwell time was 12.61 μs . The characteristic decay time of EGFP monomer in solution measured by FCS was 90 μs . The characteristic decay time of EGFP tandem oligomers in cell lysate and living cells and EGFP-GR in living cells were longer than 90 μs , and the pixel dwell time is 10 times shorter than those. The TD-N&B system analyzes the time sequence of the count rate (photon counts per second), which is corresponding to fluorescence intensity at the same pixel in the two-image series. A schematic diagram of count rate as a function of time at one pixel is shown in Figure 1C. TD-N&B determines the particle brightness and the number of particles at every pixel using a linear component and a fluctuation component of the count rate.

The time series of the count rate at a pixel detected by the two avalanche photodiodes APD₁ and APD₂ are given by:

$$I_1(t) = \varepsilon_1 N(t) + D_1(t), \quad (1)$$

$$I_2(t) = \varepsilon_2 N(t) + D_2(t), \quad (2)$$

where $I_1(t)$ and $I_2(t)$ are the count rates detected by APD₁ and APD₂, respectively, and ε_1 and ε_2 are the particle brightness values detected by APD₁ and APD₂, respectively (defined as photon counts detected per second per particle). The ratio of ε_1 to ε_2 depends on the performance of the half mirror and the quantum efficiencies of the APDs. $N(t)$ is the number of particles in the measurement volume (the confocal volume of the LSM). $D_1(t)$ and $D_2(t)$ are the noise from APD₁ and APD₂, respectively.

$I_1(t)$, $I_2(t)$, $N(t)$, $D_1(t)$, and $D_2(t)$ can be separated into two components, linear and fluctuating, as follows (Figure 1C):

$$I_1(t) = I_{l1}(t) + \delta I_1(t), \quad (3)$$

$$I_2(t) = I_{l2}(t) + \delta I_2(t), \quad (4)$$

$$N(t) = N_l(t) + \delta N(t), \quad (5)$$

$$D_1(t) = D_{l1}(t) + \delta D_1(t), \quad (6)$$

$$D_2(t) = D_{l2}(t) + \delta D_2(t). \quad (7)$$

where, subscript l represents the linear component and δ signifies the fluctuations. The linear component with offset can be obtained by the least square method from the time sequence of the pixel

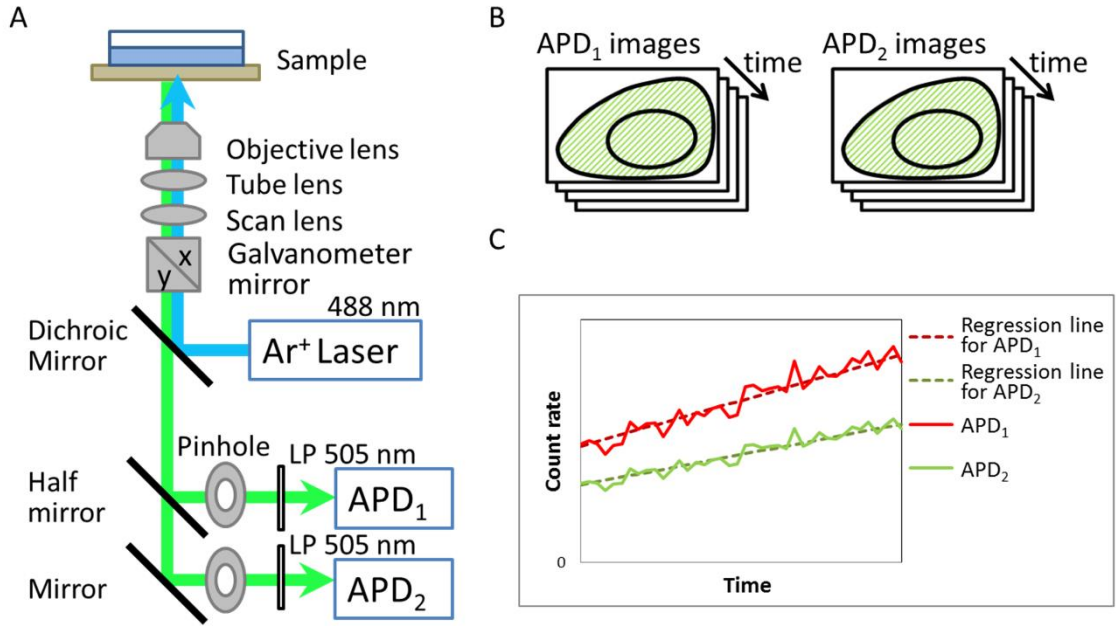


Fig. 1. The concept of two-detector number and brightness analysis (TD-N&B).

(A) Schematic diagram of the experimental setup. (B) Cartoons of image series simultaneously obtained by two avalanche photodiodes (APD). (C) Linear regression of count rate. Count rate at the same pixel was plotted as a function of time.

of interest. The following equation can be constructed from equations (1–7):

$$\begin{aligned}
 & \langle (I_1(t) - I_{l1}(t))(I_2(t) - I_{l2}(t)) \rangle \\
 &= \langle \delta I_1(t) \delta I_2(t) \rangle \\
 &= \langle (\varepsilon_1 \delta N(t) + \delta D_1(t))(\varepsilon_2 \delta N(t) + \delta D_2(t)) \rangle \\
 &= \varepsilon_1 \varepsilon_2 \langle \delta N(t)^2 \rangle + \varepsilon_1 \langle \delta N(t) \delta D_2(t) \rangle + \varepsilon_2 \langle \delta N(t) \delta D_1(t) \rangle + \langle \delta D_1(t) \delta D_2(t) \rangle \\
 &= \varepsilon_1 \varepsilon_2 \langle \delta N(t)^2 \rangle,
 \end{aligned} \tag{8}$$

where $\langle \rangle$ represents the ensemble average. Here, we assumed the following:

$$I_{l1}(t) = \varepsilon_1 N_l(t) + D_{l1}(t), \tag{9}$$

$$I_{l2}(t) = \varepsilon_2 N_l(t) + D_{l2}(t). \tag{10}$$

and we can get the following from equations (1–7, 9, 10):

$$\delta I_1(t) = \varepsilon_1 \delta N(t) + \delta D_1(t), \quad (11)$$

$$\delta I_2(t) = \varepsilon_2 \delta N(t) + \delta D_2(t). \quad (12)$$

In addition, we assumed that there is no correlation between the fluctuations of the number of particles and the detector noise ($\langle \delta N(t) \delta D_2(t) \rangle = \langle \delta N(t) \delta D_1(t) \rangle = 0$). There was also no correlation between the fluctuation fractions of the noise from the two different detectors ($\langle \delta D_1(t) \delta D_2(t) \rangle = 0$). Most of the noise effect can be eliminated using those relations.

When the number of particles in the confocal region obeys the Poisson distribution, the variance of the number is equal to the average:

$$\langle N_I(t) \rangle = \langle \delta N(t)^2 \rangle. \quad (13)$$

Finally, the number of particles and the particle brightness can be obtained from equations (8) and (13) as follows:

$$N = \frac{\langle I_1(t) \rangle \langle I_2(t) \rangle}{\langle (I_1(t) - I_{1l}(t)) (I_2(t) - I_{2l}(t)) \rangle}, \quad (14)$$

$$B = \frac{\langle I_{total}(t) \rangle}{N} = \frac{\langle I_{total}(t) \rangle \langle (I_1(t) - I_{1l}(t)) (I_2(t) - I_{2l}(t)) \rangle}{\langle I_1(t) \rangle \langle I_2(t) \rangle}, \quad (15)$$

$$\langle I_{total}(t) \rangle = \langle I_1(t) \rangle + \langle I_2(t) \rangle = \varepsilon \langle N(t) \rangle + \langle D(t) \rangle. \quad (16)$$

where $I_{total}(t) = I_1(t) + I_2(t)$, $\varepsilon = \varepsilon_1 + \varepsilon_2$, and $D(t) = D_1(t) + D_2(t)$. When the count rate is markedly larger than the noise intensity, we can assume the following:

$$\langle I_1(t) \rangle \approx \varepsilon_1 \langle N(t) \rangle, \quad (17)$$

$$\langle I_2(t) \rangle \approx \varepsilon_2 \langle N(t) \rangle, \quad (18)$$

$$\langle I_{total}(t) \rangle = \langle I_1(t) \rangle + \langle I_2(t) \rangle \approx \varepsilon \langle N(t) \rangle. \quad (19)$$

This theory can be applied to even non-linear concentration change when the concentration change is much slower than frame time, and the concentration change in a small sliding segment (described in the Analysis condition section) can be assumed as linear.

If there are only monomers and dimers of fluorescently labeled target particles, the ratio between the two can be analyzed using an advanced approach. The count rate arising from a monomer and dimer is given by:

$$I = \varepsilon_m N_m + \varepsilon_d N_d, \quad (20)$$

where I is the count rate, ε_m and ε_d are the particle brightness values of the monomer and dimer, respectively, which must be determined or measured by reference measurement, and N_m and N_d are the numbers of monomers and dimers, respectively. The ratio of the number of monomers to the number of dimers is given by:

$$\frac{N_d}{N_m} = \frac{1 - \frac{B}{\varepsilon_m}}{\frac{\varepsilon_d}{\varepsilon_m} \left(\frac{B}{\varepsilon_m} - \frac{\varepsilon_d}{\varepsilon_m} \right)}, \quad (21)$$

where B/ε_m is the particle brightness normalized to the particle brightness of an EGFP monomer. $\varepsilon_d/\varepsilon_m$ is the ratio between the particle brightness of the monomer and that of the dimer when the measurements are performed independently.

4.3.2 Simulation

The fluctuating count rate was numerically simulated using MATLAB R2009b (MathWorks, USA), and the simulated results from conventional N&B and TD-N&B were compared. In the simulation, the particle brightness and the average number of particles were $\varepsilon = 4$ [kHz] and $\langle N(t) \rangle = 50$, respectively. The linear component $N_l(t)$ was calculated using the given slope and $\langle N(t) \rangle$, and the fluctuation component $\delta N(t)$ was generated from a random number obeying the Poisson

distribution. Finally, the total count rate $I_{total}(t)$ was calculated using equation (19), and it was distributed among $I_1(t)$ and $I_2(t)$ in a 2:3 ratio.

4.3.3 Purification of EGFP

EGFP was purified using the his-tag method, which was described previously [16].

4.3.4 Preparation of EGFP tandem oligomer lysate

COS-7 cells were maintained at 37°C under a humidified atmosphere of 5% CO₂, in Dulbecco's modified Eagle's medium (DMEM; #D5796; Sigma-Aldrich, USA) supplemented with 10% fetal bovine serum (FBS; GE Healthcare, USA), 100 µg/mL penicillin G (Sigma-Aldrich, USA), and 100 µg/mL streptomycin (Sigma-Aldrich, USA). The COS-7 cells were seeded into a 6-well chamber (#140675, Thermo Fisher Scientific, USA) and incubated for 24 h. The cells (5×10^5 cells) were transfected with 1.0 µg of EGFP-C1 plasmids encoding EGFP monomer, or the plasmids encoding flexible linker (FL)-linked EGFP tandem oligomers (2–5 mer) [16] using Lipofectamine 2000 (Life Technologies, USA). The cells were incubated for 24 h. The medium was then renewed, followed by a 24-h incubation. The cells were then lysed using CellLytic M cell lysis reagent (Sigma-Aldrich, USA), and a protease inhibitor cocktail (Sigma-Aldrich, USA). The cell debris was then scraped, collected into microtubes, and centrifuged at 20,400 g for 10 min at 4°C. The supernatant cell lysate was collected and subjected to further analysis.

4.3.5 Preparation of EGFP tandem oligomer-transfected U2OS cells

U2OS cells were maintained at 37°C under a humidified atmosphere of 5% CO₂ in McCoy's 5A medium (#16600-820; Life Technologies, USA) supplemented with 10% charcoal-stripped fetal bovine serum (CS-FBS; Thermo Fisher Scientific, USA), 100 µg/mL penicillin G (Sigma-Aldrich, USA), and 100 µg/mL streptomycin (Sigma-Aldrich, USA). The U2OS cells were seeded into an 8-well chambered coverglass (#155411, Thermo Fisher Scientific, USA) and incubated for 24 h. The cells (1.6×10^4 cells) were then transfected with 0.1 µg of EGFP-C1 plasmids encoding EGFP monomer, or the plasmids encoding FL-linked EGFP tandem oligomers (2–5 mer) [16] using ViaFect (Promega, USA). The cells were incubated for 24 h. The medium was then renewed and incubation was continued for 24 h. The medium was renewed again before the measurements were taken.

4.3.6 Measurement of EGFP-GR translocation

U2OS cells were seeded into an 8-well chamber cover glass (Thermo Fisher Scientific, USA), and

incubated at 37°C in 5% CO₂ for 24 h. The cells (1.6×10^4 cells) were transfected with 0.1 µg of EGFP-GR^{WT} and EGFP-GR^{A458T} plasmids using ViaFect (Promega, USA). The cells were incubated for 24 h. The medium was then renewed and incubation was continued for 24 h. The medium was renewed again before the measurements were taken. The measurements were performed immediately after the addition of dexamethasone (final concentration of 100 nM).

4.3.7 Image acquisition for TD-N&B

Confocal fluorescence microscopy images were obtained using an LSM 710 META ConfoCor3 system (Carl Zeiss, Germany) with a C-Apochromat 40×/1.2W Corr objective (Carl Zeiss). The EGFP was excited at a wavelength of 488 nm. EGFP fluorescence was split into two channels by a half mirror, and filtered using a long-pass filter (LP505). The pinhole size was 34 µm. The zoom factor was × 6. The X- and Y-scanning sizes were 256 × 64 pixels. The pixel dwell time was 12.61 µs. Scanning was bi-directional. Except for in the GR experiment, 1,000 images were sequentially obtained; 10,000 images were obtained in the GR experiment. The laser had an output of 0.25 µW at the objective for all measurements.

4.3.8 FCS measurements

FCS measurements were performed using an LSM 710 META ConfoCor3 system (Carl Zeiss) with a C-Apochromat 40×/1.2W Corr objective (Carl Zeiss). The EGFP was excited at a wavelength of 488 nm. EGFP fluorescence was split into two channels by a half mirror and filtered using a long-pass filter (LP505). The pinhole size was 32 µm. The measurement duration was 10 s × 10 times. A multi-component diffusion model with one triplet state was used for curve-fitting:

$$G(\tau) = 1 + \left[1 + \frac{T}{1-T} \exp\left(-\frac{\tau}{\tau_{triplet}}\right) \right] \frac{1}{N} \left[\sum_i^m F_i \left(1 + \frac{\tau}{\tau_i}\right)^{-1} \left(1 + \frac{\tau}{s^2 \tau_i}\right)^{-\frac{1}{2}} \right], \quad (22)$$

where, $G(\tau)$ is a temporal autocorrelation function, T is the triplet fraction, $\tau_{triplet}$ is the relaxation time of the triplet state, N is the average number of fluorescent particles in the measurement volume, F_i and τ_i are the fraction and diffusion time of the i th component, respectively, s is a structure parameter representing the ratio of the beam waist to the axial radius, and m is the number of components. For the purified EGFP experiment, $m = 1$; for the lysate and live cell experiments, $m = 2$. After pinhole adjustment, the structure parameter was determined using a 10^{-7} M standard solution of rhodamine 6G for which the diffusion coefficient is known as $D_{Rh6G} = 414 \mu\text{m}^2/\text{s}$ [17,18].

Particle brightness was calculated as count rate divided by the number of particles, determined by FCS. In the lysate, high-intensity fluorescence bursts were occasionally observed. This might be caused by sporadic passage of aggregated EGFP tandem oligomers. The particle brightness is not significantly affected by this because the aggregates are rarely formed (Supplementary Figure S2).

4.3.9 Analysis conditions

Boxcar filtering [19] and median filtering [8] were introduced for TD-N&B. Except for the GR experiments, 1,000 images were obtained and divided into small sliding segments. The length of each sliding segment was determined to be 200, and there were 801 sliding segments. The TD-N&B calculation was performed on every sliding segment. It produced 801 maps for particle brightness and 801 maps showing number of particles. Median filtering was applied to these two maps. For each pixel, the first-neighbor pixels (3×3) were analyzed. The pixel value was replaced by the median value of the 3×3 array. After median filtering, the results for the two maps were obtained by averaging the 801 maps.

For the GR experiments, 10,000 images were divided into medium sliding segments. We determined the length of each medium sliding segment to be 1,000. This produced 9,001 medium sliding segments. An averaged particle brightness map and an averaged number of particles map were calculated for every medium sliding segment, as described above. Finally, 9,001 maps of the particle brightness and the number of particles were obtained. To reduce the enormous computation time required, parallel computing with a graphics processing unit (GPU) was performed using a JETSON TK-1 developer kit (NVIDIA, USA). The calculation time was approximately 6 h for 10,000 images.

The length of each sliding segment needs to be determined for TD-N&B analysis. Longer sliding segments produce more accurate maps, although there is the possibility that artifacts may arise owing to nonlinear changes in count rate, which are caused by cell migration or photobleaching. However, shorter sliding segments produce less accurate maps. Monomers and oligomers cannot be distinguished in the maps if the sliding segments are too short.

After the calculation, the average count rate and average particle brightness of a map was obtained in the region of interest (ROI). For the purified EGFP experiments, the ROI was set at 254×62 because the pixels at the edges of the images were distorted by median filtering. For the lysate experiments, the ROI was set at 254×62 , and the average particle brightness was calculated by fitting the histogram of particle brightness into the Gaussian distribution in order to avoid the distortion caused by aggregated EGFP tandem oligomers. For the cell experiments, the ROI was set in the nucleus or in the cytoplasm along the nuclear envelope.

4.4 Results

4.4.1 Comparison by simulation

Conventional N&B assumes that the fluorescence intensity is ergodic and its properties can therefore be deduced from a single, sufficiently long, random sample of the process. However, fluorescence intensity can change during the measurement, owing to changes in concentration or to photobleaching, especially in living cells. Therefore, the results of conventional N&B can be seriously distorted. A simulation was performed to assess these effects. In the simulation, ε was

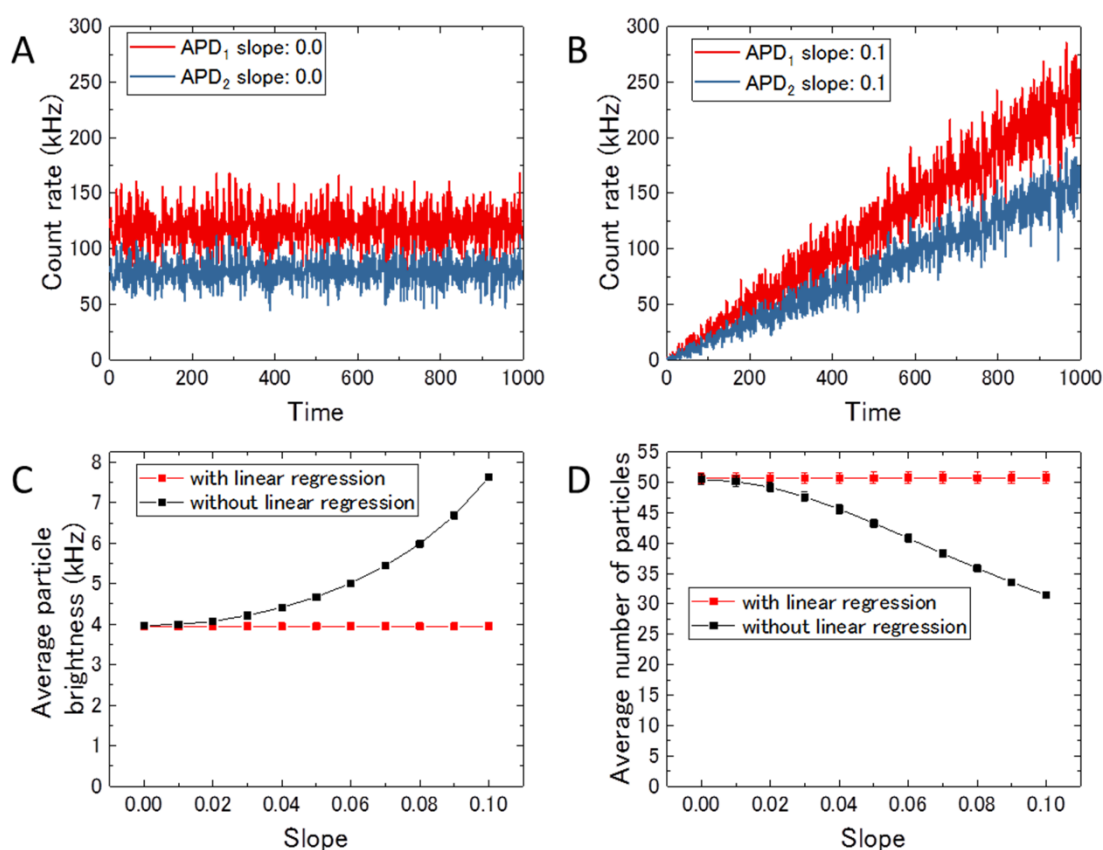


Fig. 2. Two-detector number and brightness analysis (TD-N&B) and conventional N&B simulation over a range of concentrations.

Numerical simulation in a comparison between TD-N&B and conventional N&B. $\varepsilon = 4$ [kHz] and $\langle N(t) \rangle = 50$. The count rate was distributed in a 3:2 ratio between APD₁ and APD₂ by a half mirror. A linear concentration change was assumed, and it caused a linear change of count rate. (A) Simulated count rate with a slope of 0. (B) Simulated count rate with a linear concentration change with a slope of 0.1. (C) Average particle brightness as a function of the slope. (D) Average number of particles as a function of the slope.

fixed at 4 kHz and $\langle N(t) \rangle$ was fixed at 50. As a model, it was assumed that the count rate was detected by APD₁ and APD₂ in a 3:2 ratio, and the slope of the count rate depended on the change in the concentration of the fluorophore. The simulation results are shown in Figure 2. Typical simulated signals with a slope of 0 and signals with linear concentration change with a slope of 0.1 are shown in A and B (Figure 2), respectively. The average particle brightness in conventional N&B increased with the slope of the count rate change (Figure 2C). The average number of particles in conventional N&B decreased with the count rate change (Figure 2D). The results suggest that conventional N&B is not suitable as a quantitative method when the count rate is not stable (slope $\neq 0$). Introducing a linear regression of the TD-N&B signals eliminated the effect of concentration change, and the average particle brightness and the average number of particles remained constant.

4.4.2 TD-N&B in solution

Figure 3 illustrates the dependency of particle brightness and the number of particles on the concentration of EGFP, measured by conventional N&B and TD-N&B. The samples were taken from a series comprising various dilutions of EGFP in phosphate-buffered saline. The average count rate increased with the concentration of EGFP (Figure 3A). Theoretically, the average number of particles increases with concentration, but average particle brightness remains constant. In the present study, the average particle brightness decreased at concentrations over 0.05 μM , as determined by conventional N&B (Figure 3B). The average number of particles did not increase with concentration (Figure 3C). In contrast, the average particle brightness was correctly estimated, even at concentrations over 0.05 μM , and the average number of particles increased with concentration when TD-N&B was used. This suggests that the quantitative results for particle brightness and the number of particles determined by TD-N&B are more accurate than those determined by conventional N&B. However, average particle brightness was not constant at concentrations under 0.05 μM when either method was used. This was caused by insufficient photon counts for statistical analyses.

4.4.3 In vitro investigation of EGFP tandem oligomers using TD-N&B

Next, we confirmed the dependency of particle brightness on the number of EGFP units. The particle brightness of EGFP does not precisely correspond to the number of EGFP units, because it is possible that particle brightness is affected by molecular mechanisms such as energy transfer and/or quenching. Therefore, TD-N&B requires control and calibration experiments. Those experiments were performed on EGFP tandem oligomers in the cell lysate. The schematic sequences of the EGFP tandem oligomers are shown in Figure 4A. Particle brightness was measured using both TD-N&B and conventional N&B, and the results were also compared with those of experiments that used FCS

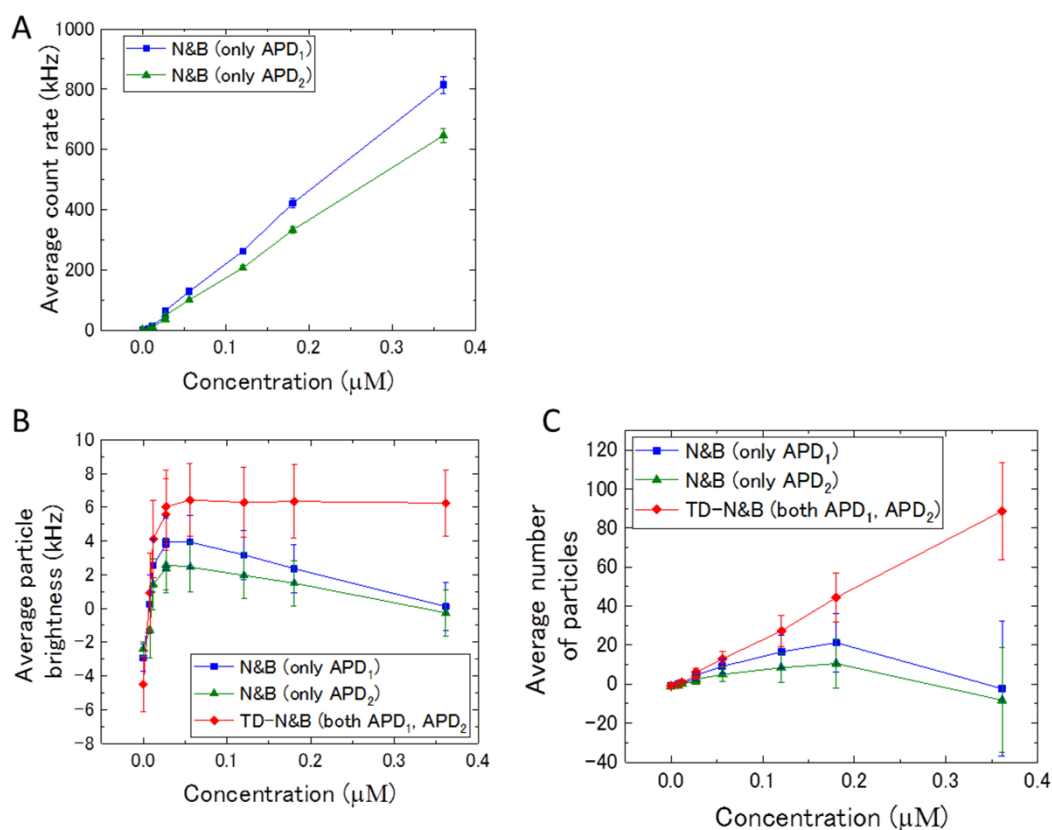


Fig. 3. Two-detector number and brightness analysis (TD-N&B) and conventional N&B experiments on a purified EGFP diluted series.

Dependency of particle brightness and the number of particles on the concentration of EGFP. The experiment was performed with a series of purified EGFP dilutions. The concentrations were measured by fluorescence correlation spectroscopy (FCS). (A) Average count rate versus concentration. (B) Average particle brightness versus concentration. (C) Average number of particles versus concentration.

as a control method (Figure 4B). Each average particle brightness was normalized to the average particle brightness of the EGFP monomers. Significant differences in normalized particle brightness using FCS, TD-N&B, and conventional N&B are shown in Figure 4C–E. A comparison between 3 different methods is shown in Figure 4F. With FCS, the normalized particle brightness increased with the number of EGFP units. Similar results were obtained using TD-N&B, but different results were obtained using conventional N&B. This was probably due to underestimation of particle brightness using conventional N&B. Particle brightness versus count rate plot is shown in supplementary figure S3A.

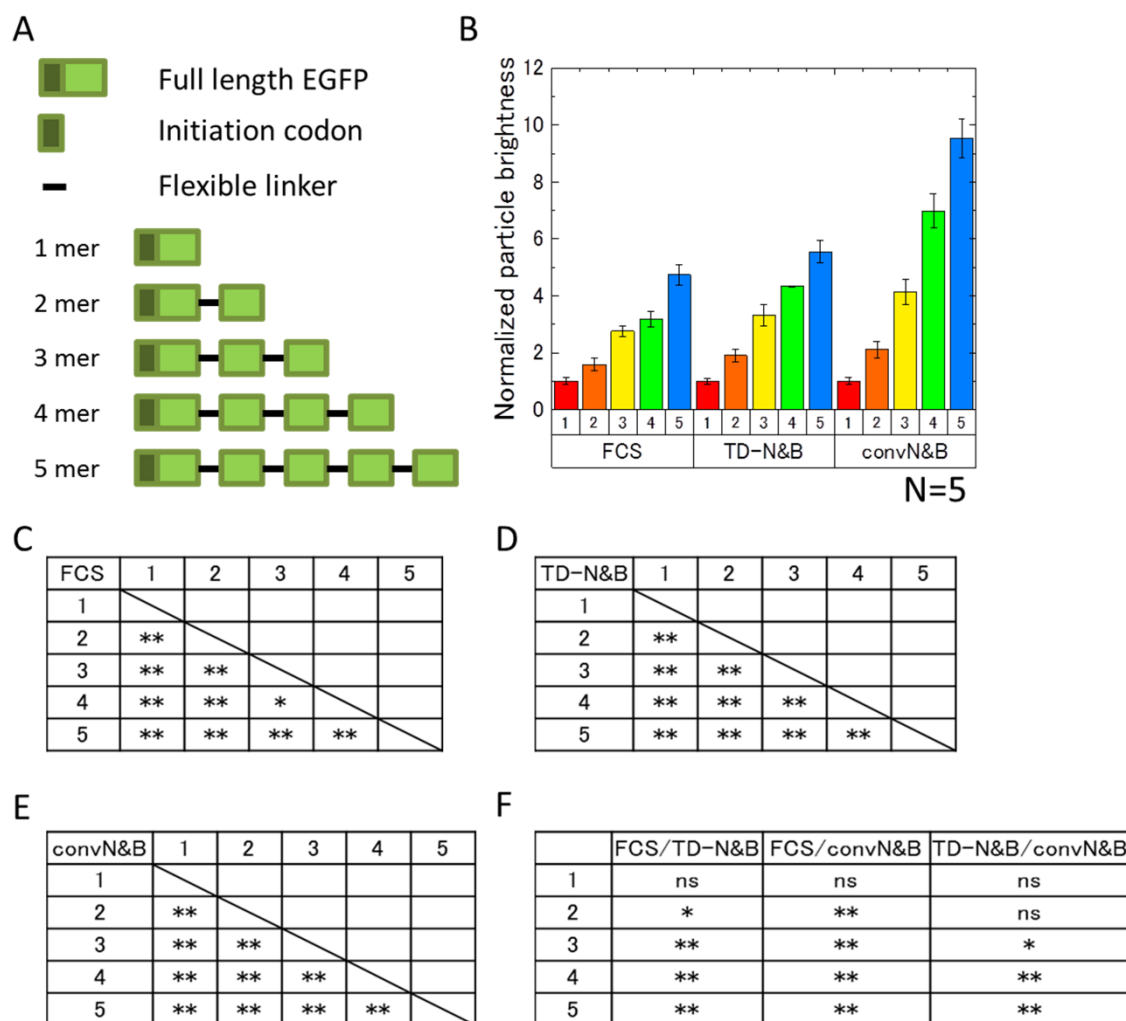


Fig. 4. Two-detector number and brightness analysis (TD-N&B), fluorescence correlation spectroscopy (FCS), and conventional N&B experiments on EGFP tandem oligomers *in vitro*.

The particle brightness of EGFP tandem oligomers in lysates was investigated using FCS, TD-N&B, and conventional N&B. Average particle brightness was normalized to that of EGFP monomers. (A) Schematic structure of EGFP tandem oligomers. (B) Comparison of normalized particle brightness among the different methods (N = 5). (C–E) Significant differences in normalized particle brightness as determined by FCS, TD-N&B, and conventional N&B (ns: not significant; * $p < 0.05$, ** $p < 0.01$). (F) Significant differences in normalized particle brightness among FCS, TD-N&B, and conventional N&B (ns: not significant; * $p < 0.05$, ** $p < 0.01$).

4.4.4 Investigation of EGFP tandem oligomers in live cells

Figures 5A–O show the count rate, the particle brightness, and the number of EGFP tandem oligomers in living cells. Normalized particle brightness was compared using FCS and TD-N&B, as seen in Figures 5P and 5Q. Significant differences in normalized particle brightness in the nucleus and cytoplasm, as determined by FCS, are shown in Figures 5R and 5S. Significant differences in normalized particle brightness in the nucleus and cytoplasm, as determined by TD-N&B are shown in Figures 5T and 5U. The results obtained using TD-N&B were similar to those obtained using FCS. Normalized particle brightness increased linearly in the cytoplasm. However, the average values of normalized particle brightness did not correspond with the number of EGFP units in the cytoplasm, unlike in the lysate, indicating that some of the EGFP units in the EGFP tandem oligomers did not fluoresce, owing to the effects of quenching, temperature, pH, and photobleaching. A detailed investigation of this phenomenon in the near future is warranted.

Moreover, normalized particle brightness did not increase linearly in the nucleus (Figures 5P and 5Q). One explanation is that larger EGFP tandem oligomers do not pass through the nuclear pores easily, resulting in a nuclear count rate that is too low to be determined accurately. Another explanation is that some of the EGFP tandem oligomers are digested into smaller fragments, which pass through the nuclear pores. The particle brightness versus count rate plot is shown in supplementary figure S3B and S3C.

4.4.5 GR measurement

Finally, we investigated the spatio-temporal distribution of nuclear translocating GR using TD-N&B. GRs are nuclear receptors that are ubiquitously expressed in almost all cells in the human body. GRs and their associated steroid ligands, the glucocorticoid hormones, regulate numerous genes that modulate the immune system [20], and play a critical role in the development and the constitutive activity of the central nervous system [21]. Although steroid hormones were first used in clinical treatments in 1948 [20], the detailed molecular mechanism of GR action remains unclear. This lack of basic mechanistic understanding hampers our ability to efficiently treat/avoid the serious side-effects related to prolonged treatment with steroid hormones.

GRs act as transcription factors by binding to the glucocorticoid response elements (GREs) in the nucleus, and act as modulators of other transcription factors. They exhibit complex dynamic behaviors such as nuclear translocation upon stimulation with steroid hormones and assembly at the DNA as dimers [22–24]. However, whether GRs form monomers or dimers during translocation is still unknown.

Figure 6 shows the particle brightness of EGFP-GR^{WT} and EGFP-GR^{A458T} in U2OS cells during nuclear translocation, as determined by TD-N&B. GR^{A458T} is a dimerization-deficient mutant. The

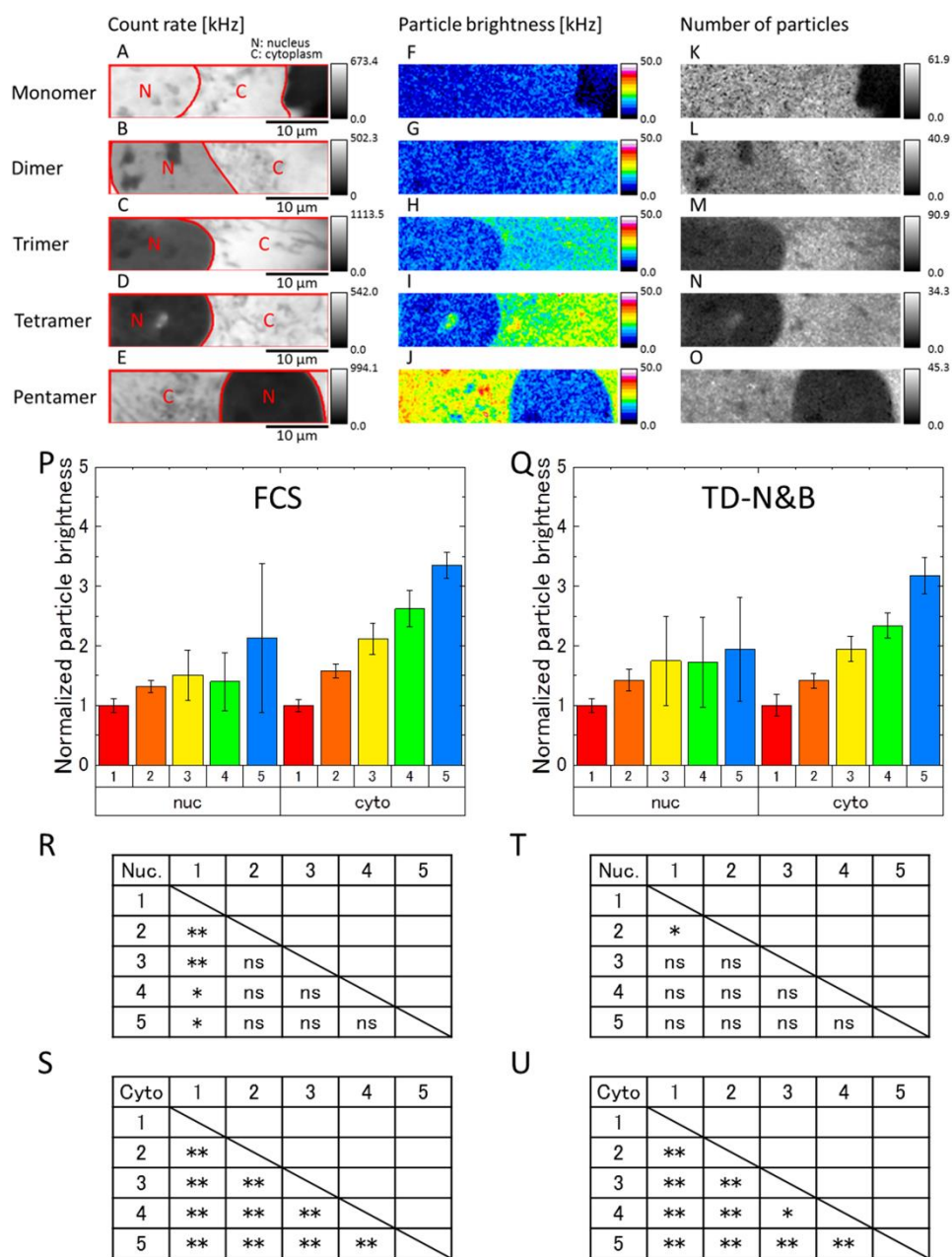


Fig. 5. Two-detector number and brightness analysis (TD-N&B) and FCS experiments on EGFP tandem oligomers *in vivo*.

Count rate, particle brightness, and the number of particles of EGFP tandem oligomers in living cells. Count rate images (A–E), particle brightness images (F–J), and the number of particles images (K–O). N: nucleus; C: cytoplasm. (P) Comparison of normalized particle brightness determined by FCS (N = 5). Nuc: in the nucleus; Cyto: in the cytoplasm. (Q) Comparison of normalized particle brightness determined by TD-N&B (N = 5). (R–U) Significant differences in normalized particle brightness in the nucleus and cytoplasm as determined by FCS and TD-N&B (ns: not significant; *p < 0.05, **p < 0.01).

average count rate and average particle brightness were calculated among pixels in a selected ROI. Average particle brightness was normalized to the average particle brightness of the EGFP monomer. Therefore, a normalized particle brightness of 1.0 or 2.0 indicated EGFP-GR monomers and dimers, respectively. The average count rate of both the wild-type (WT) and A458T increased in the nucleus and decreased in the cytoplasm, owing to nuclear translocation. The normalized particle brightness of both the WT and A458T was constant at approximately 1.0 in the cytoplasm, indicating that EGFP-GR^{WT} and EGFP-GR^{A458T} were monomeric. However, the normalized particle brightness of EGFP-GR^{WT} increased in the nucleus to 1.63 (Figure 6F), compared to the case in A458T, in which the normalized particle brightness increased to 1.34 (Figure 6H). The increase in the normalized particle brightness in the nucleus after translocation was larger in the EGFP-GR^{WT} than in EGFP-GR^{A458T}. This implies that EGFP-GR^{WT} translocated as a monomer and dimerized in the nucleus.

4.5 Discussion

We have developed and present here a two-detector optical system significantly improved N&B analysis, which we call TD-N&B. TD-N&B enables a more precise quantitative determination of particle brightness and the number of particles, compared to conventional N&B. Underestimation of particle brightness by conventional N&B in regions of high concentration was observed (Figure 3B), which is caused by the effect of dead time in the APDs. The authors of previous studies [12,13] have described a correction method for such an effect. However, TD-N&B provides accurate measurements without the need for detector dead time correction. Furthermore, TD-N&B and the linear regression analysis developed here can also eliminate other noise, including afterpulsing, shot noise, and thermal noise from detectors. Generally, it is difficult to completely predict such noise and correct the fluorescence intensity accordingly. Therefore, TD-N&B has a marked advantage in this respect. TD-N&B is applicable to concentration change during measurement in time regimes where changes in fluorescence intensity can be assumed to be linear (Figure 2).

The sensitivity to increased particle brightness using EGFP tandem oligomers is clearly demonstrated in Figure 4. The normalized particle brightness of TD-N&B corresponds to the number of EGFP units in the lysate experiment. This suggests that the number of EGFP units included in the EGFP tandem oligomers can be estimated by normalized particle brightness. We also performed TD-N&B analysis in live cells (Figure 5). The normalized particle brightness in TD-N&B increased linearly with the number of EGFP units in the live cells, but it did not directly correspond to the number of EGFP units. This suggests that the number of EGFP units included in the EGFP tandem oligomers needs to be estimated carefully. However, we were able to deduce oligomer formation from the increasing normalized particle brightness.

Finally, we were able to simultaneously monitor protein behaviors, such as the nuclear translocation and dimerization of GR in living cells using TD-N&B. It is impossible to investigate

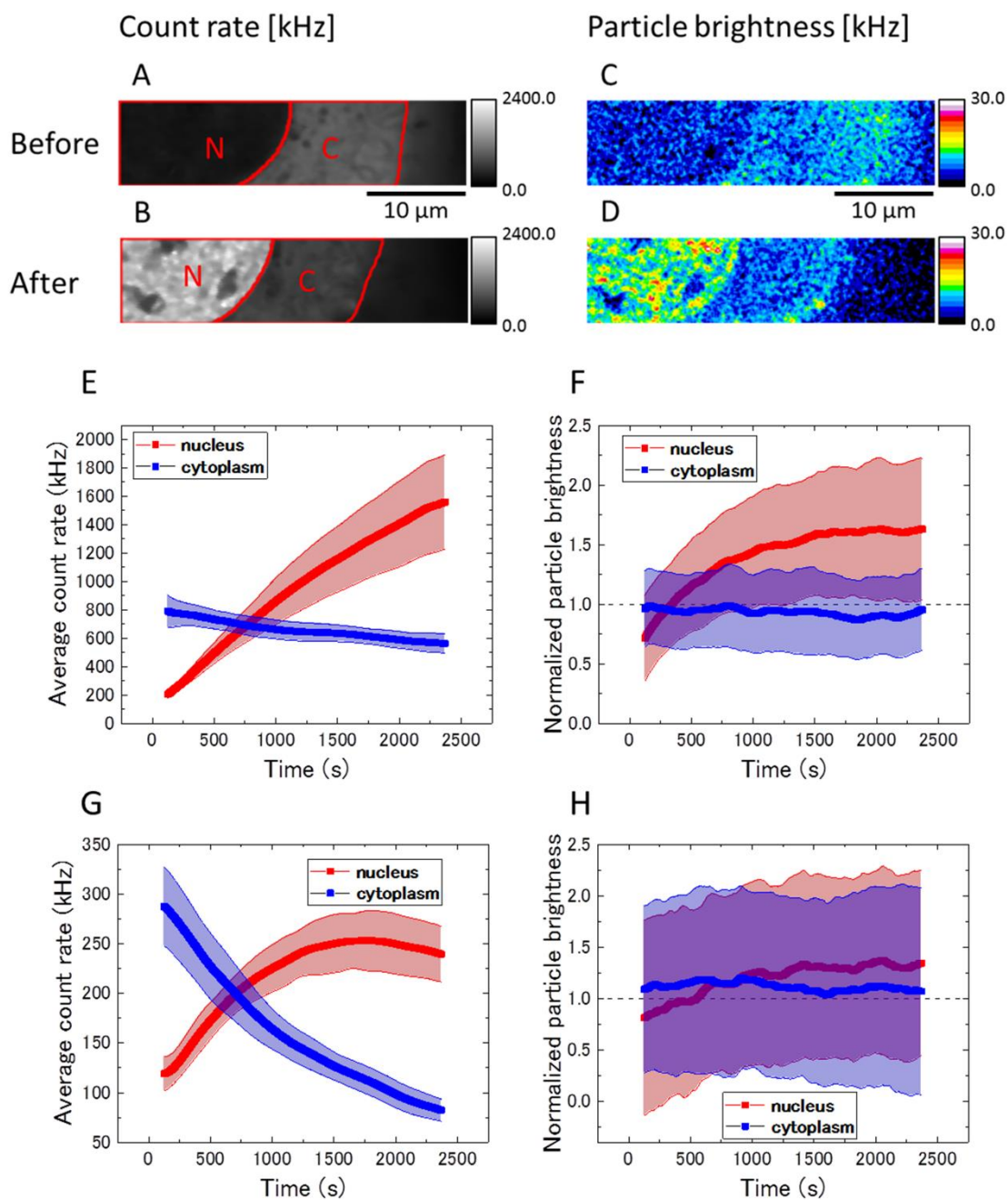


Fig. 6. Particle brightness of EGFP-GR^{WT} and EGFP-GR^{A458T} during nuclear translocation.

GR^{A458T} is a dimerization-deficient mutant. U2OS cells were transfected with EGFP-GR^{WT} and EGFP-GR^{A458T}, and stimulated with 100 nM dexamethasone. (A, B) Count rate image of EGFP-GR^{WT} before and after translocation. N: nucleus; C: cytoplasm. (C, D) Particle brightness image of EGFP-GR^{WT} before and after translocation. Average count rate during the translocation of EGFP-GR^{WT} (E) and EGFP-GR^{A458T} (G). Normalized particle brightness during the translocation of EGFP-GR^{WT} (F) and EGFP-GR^{A458T} (H).

the translocation of GR using conventional N&B, because the count rate in a ROI is dramatically changed by nuclear translocation. After translocation, the normalized particle brightness of EGFP-GR^{WT} was 1.63, and the normalized particle brightness of EGFP-GR^{A458T} was 1.34. When we assumed that the normalized particle brightness of EGFP-GR was 2.0, as it should ideally be when EGFP-GR is dimerized, the concentration ratio of the number of monomers to dimers of EGFP-GR^{WT} was estimated to be 1:0.85, and the concentration ratio of EGFP-GR^{A458T} was 1:0.26, according to equation (21). However, the normalized particle brightness of the EGFP dimers was actually 1.65 times higher than that of the EGFP monomers. Therefore, because the normalized particle brightness of EGFP-GR was 1.65 and not 2.0 when EGFP-GR was dimerized, the concentration ratio between the monomers and dimers of EGFP-GR^{WT} was 1:19.1, and the concentration ratio between the monomers and dimers of EGFP-GR^{A458T} was 1:0.66. Hence, it is possible to estimate the ratio of monomers to dimers in living cells using TD-N&B.

Our results suggest that a small amount of EGFP-GR^{A458T} dimerized in the nucleus. It has been reported that GR^{A458T} is partially dimerized in the nucleus [25]. Moreover, it has also been reported that GR dimerizes in the cytoplasm when its concentration is high [26]. The concentration of GR may have been low in our experiments, compared to the case in previous reports.

4.6 Conclusion

We have developed TD-N&B from N&B. The problems of conventional N&B were solved by introducing a two-detector optical system and linear regression of fluorescence intensity. The accuracy of TD-N&B was confirmed quantitatively by simulations and measurements in a dilution series of purified EGFP, EGFP tandem oligomers in cell lysate and living cells. TD-N&B can sequentially detect protein oligomerization over a wide field, even if the protein is diffused in living cells. Finally, the spatio-temporal measurement of localization and oligomer state change was demonstrated by an investigation of GR. We expect that TD-N&B will be useful for the discovery of compounds that promote/inhibit oligomerization, especially those that inhibit aggregation, which may be useful for the treatment of neurodegenerative diseases.

4.7 References

- [1] E.L. Elson, D. Magde, Fluorescence correlation spectroscopy. I. Conceptual basis and theory, *Biopolymers*. 13 (1974) 1–27. doi:10.1002/bip.1974.360130102.
- [2] D. Magde, E.L. Elson, W.W. Webb, Fluorescence correlation spectroscopy. II. An experimental realization, *Biopolymers*. 13 (1974) 29–61. doi:10.1002/bip.1974.360130103.
- [3] N.O. Petersen, P.L. Höddelius, P.W. Wiseman, O. Seger, K.E. Magnusson, Quantitation of membrane receptor distributions by image correlation spectroscopy: concept and application,

- Biophys. J. 65 (1993) 1135–1146. doi:10.1016/S0006-3495(93)81173-1.
- [4] M.A. Digman, P. Sengupta, P.W. Wiseman, C.M. Brown, A.R. Horwitz, E. Gratton, Fluctuation Correlation Spectroscopy with a Laser-Scanning Microscope: Exploiting the Hidden Time Structure, *Biophys. J.* 88 (2005) L33–L36. doi:10.1529/biophysj.105.061788.
- [5] M.A. Digman, C.M. Brown, P. Sengupta, P.W. Wiseman, A.R. Horwitz, E. Gratton, Measuring Fast Dynamics in Solutions and Cells with a Laser Scanning Microscope, *Biophys. J.* 89 (2005) 1317–1327. doi:10.1529/biophysj.105.062836.
- [6] P.W. Wiseman, J.A. Squier, M.H. Ellisman, K.R. Wilson, Two-photon image correlation spectroscopy and image cross-correlation spectroscopy, *J. Microsc.* 200 (2000) 14–25. doi:10.1046/j.1365-2818.2000.00736.x.
- [7] B. Kannan, J.Y. Har, P. Liu, I. Maruyama, J.L. Ding, T. Wohland, Electron Multiplying Charge-Coupled Device Camera Based Fluorescence Correlation Spectroscopy, *Anal. Chem.* 78 (2006) 3444–3451. doi:10.1021/ac0600959.
- [8] M.A. Digman, R. Dalal, A.F. Horwitz, E. Gratton, Mapping the Number of Molecules and Brightness in the Laser Scanning Microscope, *Biophys. J.* 94 (2008) 2320–2332. doi:10.1529/biophysj.107.114645.
- [9] P. Nagy, J. Claus, T.M. Jovin, D.J. Arndt-Jovin, Distribution of resting and ligand-bound ErbB1 and ErbB2 receptor tyrosine kinases in living cells using number and brightness analysis, *Proc. Natl. Acad. Sci.* 107 (2010) 16524–16529. doi:10.1073/pnas.1002642107.
- [10] G. Ossato, M.A. Digman, C. Aiken, T. Lukacsovich, J.L. Marsh, E. Gratton, A Two-Step Path to Inclusion Formation of Huntingtin Peptides Revealed by Number and Brightness Analysis, *Biophys. J.* 98 (2010) 3078–3085. doi:10.1016/j.bpj.2010.02.058.
- [11] D.M. Jones, L.A. Alvarez, R. Nolan, M. Ferriz, R. Sainz Urruela, X. Massana-Muñoz, H. Novak-Kotzer, M.L. Dustin, S. Padilla-Parra, Dynamin-2 Stabilizes the HIV-1 Fusion Pore with a Low Oligomeric State, *Cell Rep.* 18 (2017) 443–453. doi:10.1016/j.celrep.2016.12.032.
- [12] J. Hendrix, W. Schrimpf, M. Höller, D.C. Lamb, Pulsed Interleaved Excitation Fluctuation Imaging, *Biophys. J.* 105 (2013) 848–861. doi:10.1016/j.bpj.2013.05.059.
- [13] L.N. Hillesheim, J.D. Müller, The Photon Counting Histogram in Fluorescence Fluctuation Spectroscopy with Non-Ideal Photodetectors, *Biophys. J.* 85 (2003) 1948–1958. doi:10.1016/S0006-3495(03)74622-0.
- [14] K.-H. Hur, P.J. Macdonald, S. Berk, C.I. Angert, Y. Chen, J.D. Mueller, Quantitative Measurement of Brightness from Living Cells in the Presence of Photodepletion, *PLoS One.* 9 (2014) e97440. doi:10.1371/journal.pone.0097440.
- [15] R.B. Dalal, M.A. Digman, A.F. Horwitz, V. Vetri, E. Gratton, Determination of particle number and brightness using a laser scanning confocal microscope operating in the analog

- mode, *Microsc. Res. Tech.* 71 (2008) 69–81. doi:10.1002/jemt.20526.
- [16] M. Oura, J. Yamamoto, H. Ishikawa, S. Mikuni, R. Fukushima, M. Kinjo, Polarization-dependent fluorescence correlation spectroscopy for studying structural properties of proteins in living cell, *Sci. Rep.* 6 (2016) 31091. doi:10.1038/srep31091.
- [17] C.B. Müller, A. Loman, V. Pacheco, F. Koberling, D. Willbold, W. Richtering, J. Enderlein, Precise measurement of diffusion by multi-color dual-focus fluorescence correlation spectroscopy, *Europhys. Lett.* 83 (2008) 46001. doi:10.1209/0295-5075/83/46001.
- [18] C.T. Culbertson, S.C. Jacobson, J. Michael Ramsey, Diffusion coefficient measurements in microfluidic devices., *Talanta.* 56 (2002) 365–73. doi:10.1016/S0039-9140(01)00602-6.
- [19] A. Trullo, V. Corti, E. Arza, V.R. Caiolfa, M. Zamai, Application limits and data correction in number of molecules and brightness analysis, *Microsc. Res. Tech.* 76 (2013) 1135–1146. doi:10.1002/jemt.22277.
- [20] D.W. Cain, J.A. Cidlowski, Immune regulation by glucocorticoids, *Nat. Rev. Immunol.* 17 (2017) 233–247. doi:10.1038/nri.2017.1.
- [21] M. Srinivasan, D.K. Lahiri, Glucocorticoid-Induced Leucine Zipper in Central Nervous System Health and Disease, *Mol. Neurobiol.* 54 (2017) 8063–8070. doi:10.1007/s12035-016-0277-5.
- [22] S. Oasa, A. Sasaki, J. Yamamoto, S. Mikuni, M. Kinjo, Homodimerization of glucocorticoid receptor from single cells investigated using fluorescence correlation spectroscopy and microwells, *FEBS Lett.* 589 (2015) 2171–2178. doi:10.1016/j.febslet.2015.07.003.
- [23] M. Tiwari, S. Oasa, J. Yamamoto, S. Mikuni, M. Kinjo, A Quantitative Study of Internal and External Interactions of Homodimeric Glucocorticoid Receptor Using Fluorescence Cross-Correlation Spectroscopy in a Live Cell, *Sci. Rep.* 7 (2017) 4336. doi:10.1038/s41598-017-04499-7.
- [24] B.F. Luisi, W.X. Xu, Z. Otwinowski, L.P. Freedman, K.R. Yamamoto, P.B. Sigler, Crystallographic analysis of the interaction of the glucocorticoid receptor with DNA, *Nature.* 352 (1991) 497–505. doi:10.1038/352497a0.
- [25] C.M. Jewell, A.B. Scoltock, B.L. Hamel, M.R. Yudt, J.A. Cidlowski, Complex Human Glucocorticoid Receptor dim Mutations Define Glucocorticoid Induced Apoptotic Resistance in Bone Cells, *Mol. Endocrinol.* 26 (2012) 244–256. doi:10.1210/me.2011-1116.
- [26] S. Robertson, J.M. Rohwer, J.P. Hapgood, A. Louw, Impact of Glucocorticoid Receptor Density on Ligand-Independent Dimerization, Cooperative Ligand-Binding and Basal Priming of Transactivation: A Cell Culture Model, *PLoS One.* 8 (2013) e64831. doi:10.1371/journal.pone.0064831.

4.8 Supplemental Information 1

We will show that the concentration change of fluorescent particles in measurement time causes overestimation of particle brightness when the linear regression is not performed. We assume linear concentration change in measurement time for simplification. Let T be the number of frames. $N(t)$ can be separated into two components, linear and fluctuating:

$$N(t) = N_l(t) + \delta N(t). \quad (\text{S1})$$

We assume that the linear component has a slope of A and an offset of B as the following:

$$N_l(t) = At + B. \quad (\text{S2})$$

In addition, time average corresponds to the time average of linear component:

$$\langle N(t) \rangle = \langle N_l(t) \rangle. \quad (\text{S3})$$

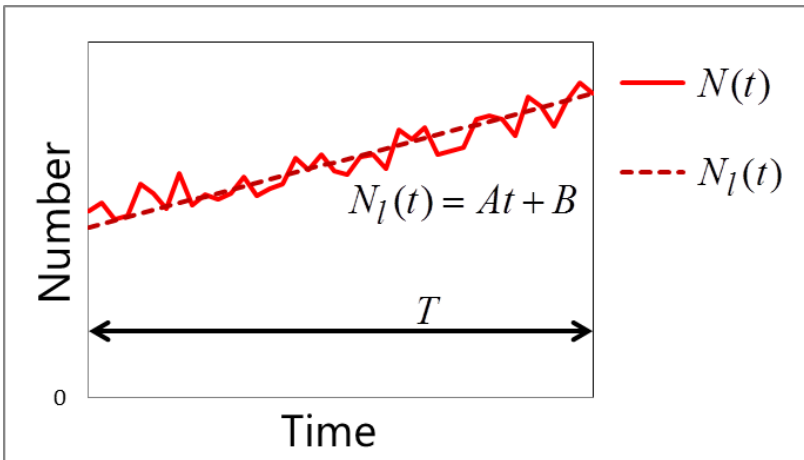


Figure 1. Linear concentration change in measurement time.

Number of particle as a function of time. Solid red line is the number of particles. Dotted line is linear component of $N(t)$.

Apparent number of particles N_{app} and apparent particle brightness B_{app} without linear regression are defined as follows:

$$N_{app} = \frac{\langle I_1(t) \rangle \langle I_2(t) \rangle}{\langle (I_1(t) - \langle I_1(t) \rangle)(I_2(t) - \langle I_2(t) \rangle) \rangle}, \quad (S4)$$

$$B_{app} = \frac{\langle I_{total}(t) \rangle}{N_{app}}. \quad (S5)$$

Substitution of equation (1, 2) and (S1, S3) into the following equation gives

$$\begin{aligned} & \langle (I_1(t) - \langle I_1(t) \rangle)(I_2(t) - \langle I_2(t) \rangle) \rangle \\ &= \varepsilon_1 \varepsilon_2 \langle (N(t) - \langle N(t) \rangle)^2 \rangle \\ &= \varepsilon_1 \varepsilon_2 \langle (N_I(t) + \delta N(t) - \langle N(t) \rangle)^2 \rangle \\ &= \varepsilon_1 \varepsilon_2 \left\{ \langle (N_I(t) - \langle N_I(t) \rangle)^2 \rangle + 2 \langle (N_I(t) - \langle N(t) \rangle) \delta N(t) \rangle + \langle \delta N(t)^2 \rangle \right\} \\ &= \varepsilon_1 \varepsilon_2 \left\{ \langle (N_I(t) - \langle N_I(t) \rangle)^2 \rangle + \langle \delta N(t)^2 \rangle \right\}. \end{aligned} \quad (S6)$$

Here, we assumed the following:

$$\langle (N_I(t) - \langle N(t) \rangle) \delta N(t) \rangle = 0. \quad (S7)$$

$\langle N_I(t) \rangle$ and $\langle (N_I(t) - \langle N_I(t) \rangle)^2 \rangle$ are calculated as follows:

$$\begin{aligned} \langle N_I(t) \rangle &= \frac{1}{T} \int_0^T At + B dt \\ &= \frac{1}{2} AT + B, \end{aligned} \quad (S8)$$

$$\begin{aligned} \langle (N_I(t) - \langle N_I(t) \rangle)^2 \rangle &= \frac{1}{T} \int_0^T \left(At - \frac{1}{2} AT \right)^2 dt \\ &= \frac{1}{12} A^2 T^2. \end{aligned} \quad (S9)$$

Finally, apparent particle brightness B_{app} can be obtained from equations (S6, S8, S9) and (13,

17-19):

$$B_{app} = \varepsilon + \frac{1}{12} \frac{A^2 T^2}{\langle N(t) \rangle} \varepsilon. \quad (\text{S10})$$

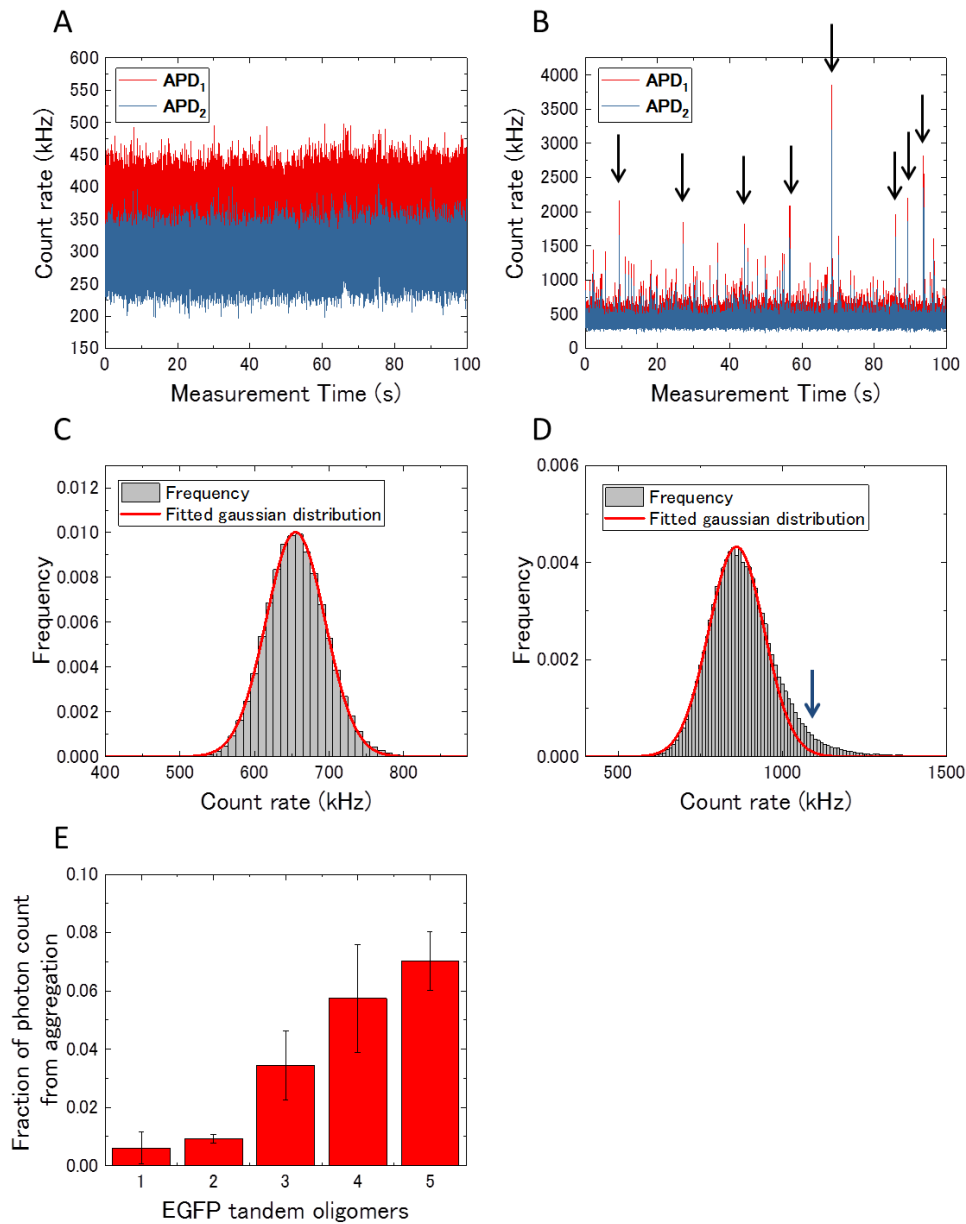
In equation (S10), the second term is always larger than 0 when the slope of the linear component A is not 0:

$$\frac{A^2 T^2}{\langle N(t) \rangle} \varepsilon \geq 0. \quad (\text{S11})$$

Therefore, the concentration change in measurement time cause overestimation of particle brightness when the linear regression is not performed:

$$B_{app} \geq B = \varepsilon. \quad (\text{S12})$$

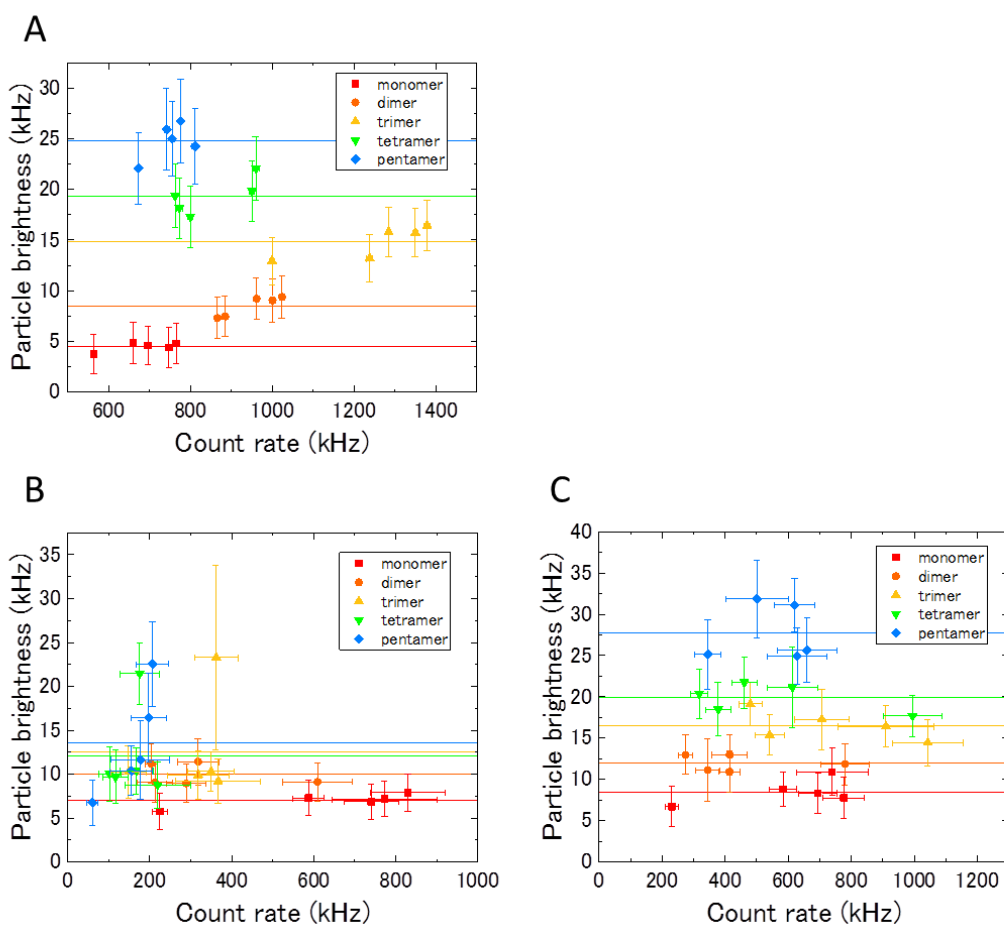
4.9 Supplemental Information 2



Supplementary Fig. S2. Aggregation of EGFP tandem oligomers in cell lysate estimated by the distribution of photon counts in FCS.

(A) and (B) show the fluorescence intensity fluctuation in the EGFP monomer lysate and EGFP pentamer lysate, respectively. High-intensity fluorescence burst were occasionally observed (black arrows). Photon count distribution of the EGFP monomer lysate (C) and EGFP pentamer lysate (D). Frequency was normalized to 1. The distributions were fitted to a normal distribution (red line). Rarely formed aggregated EGFP tandem oligomers were occasionally observed (blue arrow). (E) Fraction of photon count from aggregation was estimated by the area outside of the normal distribution.

4.10 Supplemental Information 3



Supplementary Fig. S3. Particle brightness versus count rate plot.

(A) Particle brightness versus count rate of EGFP tandem oligomer in the lysate. (B) Particle brightness versus count rate of EGFP tandem oligomer in the nuclei of living cells. (C) Particle brightness versus count rate of EGFP tandem oligomer in the cytoplasm of living cells. Colored horizontal lines are average for the particle brightness of EGFP tandem oligomers.

Chapter 5

Application of ML and MAP Estimation Along With EB Method

5.1 Abstract

Number and brightness (N&B) analysis is useful for monitoring the spatial distribution of the concentration and oligomeric state of fluorescently labeled proteins in cells. N&B analysis is based on the statistical analysis of fluorescence images by using the method of moments (MoM). Further, N&B analysis can determine the particle number and particle brightness, which indicate the concentration and oligomeric state, respectively. However, the statistical accuracy and precision are limited in actual experiments with fluorescent proteins, owing to low excitation and the limited number of images. In this study, we applied maximum likelihood (ML) estimation and maximum a posteriori (MAP) estimation coupled with the empirical Bayes (EB) method (referred to as EB-MAP). In EB-MAP, we constructed a simple prior distribution for a pixel to utilize the information of the surrounding pixels. To evaluate the accuracy and precision of our method, we conducted simulations and experiments and compared the results of MoM, ML, and EB-MAP. The results showed that MoM estimated the particle number with many outliers. The outliers hampered the visibility of the spatial distribution and cellular structure. In contrast, EB-MAP suppressed the number of outliers and improved the visibility notably. The precision of EB-MAP was better by an order of magnitude in terms of particle number and 1.5 times better in terms of particle brightness compared with those of MoM. The proposed method (EB-MAP-N&B) is applicable to studies on fluorescence imaging, and would aid in accurately recognizing changes in the concentration and oligomeric state in cells. Our results hold significant importance because quantifying the concentration and oligomeric state would contribute to the understanding of dynamic processes in molecular mechanism in cells.

5.2 Introduction

Fluorescence imaging reveals the localization and distribution of fluorescently labeled molecules in cells. The concentration of molecules is strongly related to the progress of chemical reactions in cells, and the reactions regulate cellular functions. Thus, quantifying the concentration would yield valuable information about the regulations and the functions of cells. However, changes in the fluorescence intensity of images are caused by changes in the concentration and brightness of a single particle. Thus, with the exception of single molecule detection, it is challenging to quantify the concentration of fluorescent molecules from only the fluorescence images. Continuously observing the changes in

fluorescence intensity allows for the deconstruction of the fluorescence intensity into two factors.

Fluorescence fluctuation spectroscopy (FFS) (1–3) is a general term for methods that analyze the temporal and spatial fluctuations in fluorescence intensity; it also provides useful information on factors such as concentration, oligomeric state, and rate of diffusion. Fluorescence correlation spectroscopy (FCS) (4) is a well-known method based on the statistical analysis of temporally correlated fluctuations caused by diffusing particles. The measurement type of this method is a single-spot measurement, typically achieved using confocal fluorescence microscopy. Fluorescent particles freely diffuse and pass through the confocal volume (i.e., measurement volume) created by microscopy. Microscopy records the fluctuation in fluorescence intensity over time, and the fluctuation is described as an autocorrelation function. Typically, the weighted least squares method determines the parameters of the autocorrelation function. However, with the exception of several reports (5, 6), FCS could obtain single-spot information.

Number and brightness (N&B) analysis (7) is another method based on the statistical analysis of temporally independent fluctuations in photon-counting images. In this method, images are typically obtained using confocal laser scanning microscopy. This microscopy method successively counts photons within a given sampling time while scanning and recording the counts as an image consisting of pixels. Iterative scanning produces a sequence of images, and the temporal fluctuation at each pixel position is analyzed based on the method of moments (MoM). Let us define an imaging duration as the period between a sampling and the next sampling at a pixel position. Under typical measurement conditions, the sampling time for a single pixel is less than several tens of microseconds, and the imaging duration is between hundreds of milliseconds to seconds for images of a sufficiently large size. This imaging duration is sufficient for fluorescent particles to pass through the confocal volume, and the temporal fluctuations become independent, unlike those in FCS because of the long imaging duration. In MoM, the first and second raw moments are estimated; moments are characteristic values of the probability distribution. The first moment is the sample average, and the second is an element constituting sample variance. The estimator consisting of the moments gives the particle number and particle brightness (7–10). The particle number reflects the concentration, whereas the particle brightness reflects the fluorescence intensity of a single particle. The fold change in particle brightness can be used to infer the oligomeric state. In the dimerization of two monomers into a dimer (Fig. 1), the fluorescence intensities of the monomers and the dimers are the same. In contrast, the numbers of particles are different, i.e., 2 and 1 for the monomers and the dimers, respectively. A dimer carries two fluorescent proteins; thus, the particle brightness of a dimer is twice that of a monomer.

FCS is a single-spot measurement, whereas N&B analysis is a two-dimensional imaging-based measurement. The N&B analysis determines the particle number and particle brightness at each pixel position, and reveals their distribution as an image. Thus, N&B analysis is advantageous for monitoring the wide spatial range in cells. However, the conventional method estimates the particle

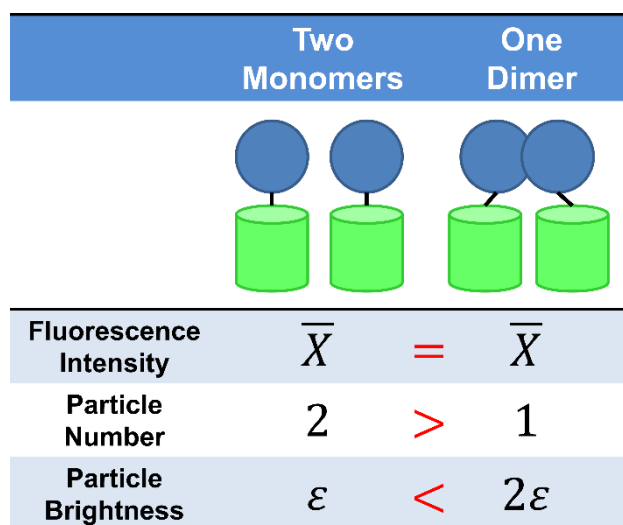


FIGURE 1: Reflection of oligomeric state by particle brightness

Fluorescent protein (green cylinder), two fluorescently labeled monomers, and one dimer. Fluorescence intensity of the monomers and the dimer are given by \bar{X} (the overline represents average). In the dimerization, the particle number reduces by half, and the particle brightness doubles.

number and particle brightness with low accuracy and precision in a practical experiment with fluorescent proteins. Theoretically, a measurement with high excitation and an analysis with a large number of images yield accurate and precise estimation; however, they cause photobleaching and have low time-resolution in an actual experiment. If photobleaching occurs, MoM underestimates the particle number and overestimates particle brightness. Under undesired conditions, such as low excitation and small number of images, the particle number and particle brightness are sometimes estimated negatively, and outliers of particle number appear often. In this report, we consider the estimation of the particle number and particle brightness in the absence of photobleaching.

In this study, we evaluated the performance of three different approaches, namely, MoM estimation, maximum likelihood (ML) estimation, and maximum a posteriori (MAP) estimation coupled with the empirical Bayes (EB) method (hereinafter referred to as EB-MAP). Regarding MoM, Qian and Elson reported a basic theory for N&B analysis in 1990, and Digman et al. applied it to laser scanning microscopy in 2008. However, little research has been conducted on devising solutions to improve the accuracy and precision of N&B analysis at a fundamental level, although it has been 30 years since the introduction of this theory. Furthermore, the application of ML estimation and EB-MAP to N&B analysis has not been studied before. In the estimation using MoM, we adopted two-detector N&B (TD-N&B) analysis, which reduces the effect of afterpulse and dead time reported previously (11). The ML determines the parameters by maximizing the likelihood function. The MAP estimation is a Bayesian approach, and utilizes prior distribution in addition to the likelihood function. The

advantages of ML and Bayesian approaches have been reported in several studies. Strey investigated the least squares method and ML for the autocorrelated time trace originating from the Ornstein–Uhlenbeck process (12). He reported that using the least squares method in FCS causes systematic deviation from the true parameters. Jazani et al. reported such a deviation in FCS using Bayesian non-parametrics (13). Regarding the fluorescence lifetime measurement, Santra et al. investigated the least squares method, ML, and the related methods, and reported robustness of ML (14, 15). In the N&B analysis, a simple assumption (detailed later, before Eq. 3) enables the description of the probability distribution of photon counts based on Neyman type A distribution. Shenton evaluated the asymptotic efficiency of an MoM estimator (16), and Shenton and Bowman investigated the bias and variance of MoM and ML with a sample size of 100 (17). These reports suggested that the estimations of ML are more precise than those of MoM. However, ML sometimes estimates the particle number and particle brightness as infinity and 0, respectively, although their parameter space is limited on the intervals over 0 and below infinity; these estimates are known as boundary estimates (18, 19).

To avoid such parameters, we applied MAP estimation. The prior distribution acts as a regularization term and prevents the boundary estimates. We assumed that the distribution of the particle number at a pixel and the surrounding pixels follows lognormal distribution. Then, we applied the EB method to determine the parameters of the distribution. Finally, we demonstrated the feasibility of our methods by simulations and experiments on an enhanced green fluorescent protein (EGFP) solution and the cells expressing EGFP tandem-oligomers.

5.3 Methods

5.3.1 Photon-counting model

Single detector

We constructed a double-detector system for single-color imaging by coupling a half mirror. In our single-detector system, the saturation of the photon count in the avalanche photodiode is severe if the fluorescence intensity is higher than 500 kHz. To extend the applicability of our method, we included the half mirror and reduced the fluorescence intensity of the detector. First, we describe a theory for photon counting by a single detector, and then extend the theory to double detectors.

A semiclassical description of photon counting was made by Mandel (20). Here, we make assumptions based on the theory of photon counting histogram (PCH) (21). Let $I_t(t)$ be the instantaneous light intensity of a detector at time t , and T be the sampling time. The light intensity at a sampling time is given by the integral from t to $t + T$ of $I_t(t)$. Here, we assume that the sampling time is sufficiently short compared with the residence time of the diffusing particles in the confocal volume. This assumption indicates that the number of particles does not change during the sampling time, and thus enables to track the number of particles at the moment of sampling. Under

this assumption, the light intensity during the sampling time is given by $I_t T$, and the probability distribution for observing W photons during sampling by a single detector is given by rewriting Mandel's formula (21, 22):

$$P(W|\eta) = \int_0^\infty \text{Poi}(W|\eta I_0) P(I_0) dI_0, \quad (1)$$

where η denotes the detection efficiency of the detector; I_0 is the integrated light intensity ($I_0 = I_t T$); $P(I_0)$ is the probability distribution for I_0 ; $\text{Poi}(W|\eta I_0)$ is a Poisson distribution given as follows:

$$\text{Poi}(W|\eta I_0) = \frac{(\eta I_0)^W}{W!} \exp(-\eta I_0). \quad (2)$$

We simply assume that the intensity fluctuation depends only on the changes in the number of particles, and the fluctuation follows Poisson distribution. The probability distribution for observing W photons is given by Neyman type A distribution as follows:

$$\text{Ney}(W|\nu, \varepsilon) = \sum_{Z=0}^{\infty} \text{Poi}(W|\varepsilon Z) \text{Poi}(Z|\nu), \quad (3)$$

where ν denotes the particle number ($0 < \nu$), a parameter of the Poisson distribution characterizing the fluctuation in the instantaneous number of particles in the confocal volume; Z is a hidden variable and a realized outcome of the Poisson distribution; ε denotes particle brightness ($0 < \varepsilon$), an average photon count from a single particle within a sampling time; and ε/T represents the particle brightness in Hz. Calculating the probabilities using Eq. 3 is difficult because it contains an infinite series; however, the following recursive formula is available (23, 24):

$$\text{Ney}(W|\nu, \varepsilon) = \begin{cases} \exp[\nu\{\exp(-\varepsilon) - 1\}], & (W = 0), \\ \frac{1}{W} \nu \varepsilon \exp(-\varepsilon) \sum_{l=0}^{W-1} \frac{\varepsilon^{W-l-1}}{(W-l-1)!} \text{Ney}(l|\nu, \varepsilon), & (W \geq 1). \end{cases} \quad (4)$$

Double detectors

We extend the equations obtained above to a double-detector system. The light intensity is separated by a half mirror and detected by two photon detectors. Let I_1 and I_2 be integrated light intensities in detector 1 and 2, respectively. The probability distribution for observing X and Y photons at

detector 1 and 2, respectively, is given as follows (22):

$$P(X, Y | \eta_1, \eta_2) = \int_0^\infty \int_0^\infty \text{Poi}(X | \eta_1 I_1) \text{Poi}(Y | \eta_2 I_2) P(I_1, I_2) dI_1 dI_2, \quad (5)$$

where η_1 and η_2 denote the detection efficiency of detector 1 and 2, respectively. Under the same assumptions as those for Eq. 3, the probability distribution for observing X and Y photons is given by

$$\begin{aligned} P(X, Y | \nu, \varepsilon, p) &= \sum_{Z=0}^{\infty} \text{Poi}(X | \varepsilon p Z) \text{Poi}(Y | \varepsilon(1-p)Z) \text{Poi}(Z | \nu) \\ &= \text{Bin}(X, Y | p) \text{Ney}(W | \nu, \varepsilon), \end{aligned} \quad (6)$$

where p represents a fraction of light intensity reaching detector 1, W is equal to $X + Y$, and $\text{Bin}(X, Y | p)$ is a binomial distribution given by

$$\text{Bin}(X, Y | p) = \frac{(X+Y)!}{X!Y!} p^X (1-p)^Y. \quad (7)$$

The recursive formula similar to Eq. 4 is given by (see Supporting Material for derivation)

$$P(X, Y | \nu, \varepsilon, p) = \begin{cases} \exp[\nu(\exp[-\varepsilon] - 1)], & (X=0, Y=0), \\ \frac{1}{Y} \nu \varepsilon (1-p) \exp[-\varepsilon] \sum_{m=0}^{Y-1} \frac{\{(1-p)\varepsilon\}^{Y-m-1}}{(Y-m-1)!} P(0, m | \nu, \varepsilon, p), & (X=0, Y \geq 1), \\ \frac{1}{X} \nu \varepsilon p \exp[-\varepsilon] \sum_{m=0}^Y \frac{\{(1-p)\varepsilon\}^{Y-m}}{(Y-m)!} \sum_{l=0}^{X-1} \frac{(p\varepsilon)^{X-l-1}}{(X-l-1)!} P(l, m | \nu, \varepsilon, p), & (X \geq 1, Y \geq 0). \end{cases} \quad (8)$$

Single detector affected by dead time

Dead time is a non-ideal property of a photon detector that causes loss of photon count. Dead time is a time period after photon detection during which detectors cannot detect any photons. Underestimation of particle brightness without correction for dead time has been reported (11, 25). Let τ be the dead time, and $\delta = \tau/T$. The probability distribution for observing W photons on a dead-time-affected detector is given as follows for $W < 1/\delta$ (see Supporting Material for derivation):

$$P(W|v, \varepsilon, \delta) = \sum_{m=0}^{\infty} A_m(W, \delta) \text{Ney}(W + m|v, \varepsilon), \quad (9)$$

where the function $A_m(W, \delta)$ is given by

$$A_m(W, \delta) = \binom{W+m}{W} \sum_{k=m}^{W+m} (-1)^{k-m} \binom{W}{k-m} \delta^k \left[\left(1 - \frac{m}{k}\right) (W-1)^k + \frac{m}{k} W^k \right]. \quad (10)$$

Double detectors affected by dead time

For a double-detector system, let τ_1 and τ_2 be the dead time for detectors 1 and 2, respectively, and let us define $\delta_1 = \tau_1/T$ and $\delta_2 = \tau_2/T$. The joint probability distribution for observing X and Y photons on a dead-time-affected detector is given as follows for $X < 1/\delta_1$ and $Y < 1/\delta_2$ (see Supporting Material for derivation):

$$P(X, Y|v, \varepsilon, p, \delta_1, \delta_2) = \sum_{m=0}^{\infty} \sum_{h=0}^m A_h(X, \delta_1) A_{m-h}(Y, \delta_2) P(X+h, Y+m-h|v, \varepsilon, p). \quad (11)$$

In this study, we assumed that higher terms of the infinite series, such as $3 \leq m$, are negligible.

5.3.2 Maximum likelihood estimation

Double-detector model

The ML determines parameters by maximizing a likelihood function. We assume independent I time observations. In the N&B analysis, independent observations are realized if the imaging duration is sufficiently longer than the residence time of the fluorescent particles in the confocal volume. The likelihood function is given as follows, with $\mathbf{x} = (x_1, x_2, \dots, x_I)$ and $\mathbf{y} = (y_1, y_2, \dots, y_I)$:

$$\mathcal{L}(\mathbf{x}, \mathbf{y}|v, \varepsilon, p) = \prod_{i=1}^I P(x_i, y_i|v, \varepsilon, p). \quad (12)$$

We numerically estimate the maximum point on the natural logarithm of the likelihood function by using the Newton–Raphson method. This is an iterative method and requires the first and second derivatives of the log-likelihood function. The first derivatives with respect to the parameters are given by,

$$\frac{\partial \log \mathcal{L}}{\partial \nu}(\mathbf{x}, \mathbf{y} | \nu, \varepsilon, p) = -I + \frac{1}{\nu \varepsilon} S_1(\mathbf{x} + \mathbf{y}, \nu, \varepsilon), \quad (13)$$

$$\frac{\partial \log \mathcal{L}}{\partial \varepsilon}(\mathbf{x}, \mathbf{y} | \nu, \varepsilon, p) = \frac{1}{\varepsilon} S_0(\mathbf{x} + \mathbf{y}) - \frac{1}{\varepsilon} S_1(\mathbf{x} + \mathbf{y}, \nu, \varepsilon), \quad (14)$$

$$\frac{\partial \log \mathcal{L}}{\partial p}(\mathbf{x}, \mathbf{y} | \nu, \varepsilon, p) = \frac{1}{p} S_0(\mathbf{x}) - \frac{1}{1-p} S_0(\mathbf{y}), \quad (15)$$

where

$$S_0(\mathbf{w}) := \sum_{i=1}^I w_i, \quad (16)$$

$$S_1(\mathbf{w}, \nu, \varepsilon) := \sum_{i=1}^I \frac{(w_i + 1) \text{Ney}(w_i + 1 | \nu, \varepsilon)}{\text{Ney}(w_i | \nu, \varepsilon)}, \quad (17)$$

$\mathbf{w} = (w_1, w_2, \dots, w_I)$, and $w_i = x_i + y_i$ ($i = 1, 2, \dots, I$). Setting the first derivatives to zero gives

$$\nu \varepsilon = \frac{1}{I} \sum_{i=1}^I (x_i + y_i), \quad (18)$$

$$\hat{p} = \frac{\sum_{i=1}^I x_i}{\sum_{i=1}^I (x_i + y_i)}. \quad (19)$$

Substituting $\varepsilon = \bar{w}/\nu$ ($\bar{w} = \frac{1}{I} \sum_{i=1}^I x_i + y_i$) into the probability distribution and the log-likelihood function gives a univariate likelihood function. The first and second derivatives with respect to ν are given by,

$$\frac{\partial \log \mathcal{L}}{\partial \nu}(\mathbf{x}, \mathbf{y} | \nu, \frac{\bar{w}}{\nu}, p) = -I - \frac{I\bar{w}}{\nu} + \left(\frac{1}{\nu} + \frac{1}{\bar{w}} \right) S_1\left(\mathbf{x} + \mathbf{y}, \nu, \frac{\bar{w}}{\nu}\right), \quad (20)$$

$$\begin{aligned}
& \frac{\partial^2 \log \mathcal{L}}{\partial \nu^2}(\mathbf{x}, \mathbf{y} | \nu, \frac{\bar{w}}{\nu}, p) \\
&= \frac{I\bar{w}}{\nu^2} - \frac{1}{\nu} \left(\frac{2}{\nu} + \frac{1}{\bar{w}} \right) S_1 \left(\mathbf{x} + \mathbf{y}, \nu, \frac{\bar{w}}{\nu} \right) + \left(\frac{1}{\nu} + \frac{1}{\bar{w}} \right)^2 S_2 \left(\mathbf{x} + \mathbf{y}, \nu, \frac{\bar{w}}{\nu} \right) \\
& - \left(\frac{1}{\nu} + \frac{1}{\bar{w}} \right)^2 S_3 \left(\mathbf{x} + \mathbf{y}, \nu, \frac{\bar{w}}{\nu} \right),
\end{aligned} \tag{21}$$

where

$$S_2(\mathbf{w}, \nu, \varepsilon) := \sum_{i=1}^I \frac{(w_i + 1)(w_i + 2) \text{Ney}(w_i + 2 | \nu, \varepsilon)}{\text{Ney}(w_i | \nu, \varepsilon)}, \tag{22}$$

$$S_3(\mathbf{w}, \nu, \varepsilon) := \sum_{i=1}^I \left\{ \frac{(w_i + 1) \text{Ney}(w_i + 1 | \nu, \varepsilon)}{\text{Ney}(w_i | \nu, \varepsilon)} \right\}^2. \tag{23}$$

For the initial value of $\nu^{(0)}$, the k -th iteration process of the Newton–Raphson method ($k = 0, 1, 2, \dots$) is given by,

$$\nu^{(k+1)} = \nu^{(k)} - \frac{\frac{\partial \log \mathcal{L}}{\partial \nu}(\mathbf{x}, \mathbf{y} | \nu, \frac{\bar{w}}{\nu}, p)}{\frac{\partial^2 \log \mathcal{L}}{\partial \nu^2}(\mathbf{x}, \mathbf{y} | \nu, \frac{\bar{w}}{\nu}, p)}. \tag{24}$$

Dead-time-affected double-detector model

The likelihood function for a dead-time-affected photon count is given by,

$$\mathcal{L}(\mathbf{x}, \mathbf{y} | \nu, \varepsilon, p, \delta_1, \delta_2) = \prod_{i=1}^I P(x_i, y_i | \nu, \varepsilon, p, \delta_1, \delta_2). \tag{25}$$

In the dead-time-affected model, the relationship between ν and ε , similar to Eq. 18, was not obtained; thus, we use the Newton–Raphson method for two variables to find the maximum of the likelihood function. The first and second derivatives of the log-likelihood function are calculated from the probability distribution for the dead-time-affected photon count and the first and second derivatives of this probability distribution. The first and second derivatives are obtained by taking the derivative of Eq. 11. We assumed a constant dead time of 50 ns ($\delta_1 = \delta_2 = 7.82 \times 10^{-3}$). The first and second derivatives of the probability distribution for an ideal photon count are given by,

$$\frac{\partial P}{\partial v}(X, Y|v, \varepsilon, p) = -P(X, Y|v, \varepsilon, p) + \frac{X+1}{v\varepsilon p}P(X+1, Y|v, \varepsilon, p), \quad (26)$$

$$\frac{\partial P}{\partial \varepsilon}(X, Y|v, \varepsilon, p) = \frac{X+Y}{\varepsilon}P(X, Y|v, \varepsilon, p) - \frac{X+1}{\varepsilon p}P(X+1, Y|v, \varepsilon, p), \quad (27)$$

$$\begin{aligned} \frac{\partial^2 P}{\partial v^2}(X, Y|v, \varepsilon, p) &= P(X, Y|v, \varepsilon, p) - \frac{(2v+1)(X+1)}{v^2\varepsilon p}P(X+1, Y|v, \varepsilon, p) \\ &\quad + \frac{(X+1)(X+2)}{v^2\varepsilon^2 p^2}P(X+2, Y|v, \varepsilon, p), \end{aligned} \quad (28)$$

$$\begin{aligned} \frac{\partial^2 P}{\partial v \partial \varepsilon}(X, Y|v, \varepsilon, p) &= -\frac{X+Y}{\varepsilon}P(X, Y|v, \varepsilon, p) + \frac{(X+Y+v\varepsilon)(X+1)}{v\varepsilon^2 p}P(X+1, Y|v, \varepsilon, p) \\ &\quad - \frac{(X+1)(X+2)}{v\varepsilon^2 p^2}P(X+2, Y|v, \varepsilon, p), \end{aligned} \quad (29)$$

$$\begin{aligned} \frac{\partial^2 P}{\partial \varepsilon^2}(X, Y|v, \varepsilon, p) &= \frac{(X+Y)(X+Y-1)}{\varepsilon^2}P(X, Y|v, \varepsilon, p) \\ &\quad - \frac{2(X+Y)(X+1)}{\varepsilon^2 p}P(X+1, Y|v, \varepsilon, p) \\ &\quad + \frac{(X+1)(X+2)}{\varepsilon^2 p^2}P(X+2, Y|v, \varepsilon, p). \end{aligned} \quad (30)$$

For the initial values of $v^{(0)}$ and $\varepsilon^{(0)}$, the k -th iteration process of the Newton–Raphson method ($k = 1, 2, 3, \dots$) is given by,

$$\begin{pmatrix} v^{(k+1)} \\ \varepsilon^{(k+1)} \end{pmatrix} = \begin{pmatrix} v^{(k)} \\ \varepsilon^{(k)} \end{pmatrix} - \begin{pmatrix} \frac{\partial^2 \log L}{\partial v^2} & \frac{\partial^2 \log L}{\partial v \partial \varepsilon} \\ \frac{\partial^2 \log L}{\partial v \partial \varepsilon} & \frac{\partial^2 \log L}{\partial \varepsilon^2} \end{pmatrix}^{-1} \begin{pmatrix} \frac{\partial \log L}{\partial v} \\ \frac{\partial \log L}{\partial \varepsilon} \end{pmatrix}, \quad (31)$$

where $\log \mathcal{L}$ is the abbreviated form of $\log \mathcal{L}(x, y|v, \varepsilon, p, \delta_1, \delta_2)$.

5.3.3 *Maximum a posteriori estimation*

In ML, the estimates are sometimes on the boundary of the parameter space, which are known as boundary estimates (18, 19). In our N&B analysis, although the parameter space of ν and ε is $0 < \nu < \infty$ and $0 < \varepsilon < \infty$, respectively, the maximum point of the log-likelihood is sometimes given by ν of infinity and ε of 0 (see Fig. S3.3 in Supporting Material). Some studies have reported that boundary estimates are obtained via analyses using a statistical model that contains hidden variables, and appear on a small sample size (18). In fact, N&B analysis has a hidden variable Z for the number of particles at the moment of a sampling. The boundary estimates appeared well in an analysis with a small frame number or low particle brightness (see Fig. S3.1 in Supporting Material). To avoid the estimates, we applied MAP estimation. A MAP estimate is given by maximizing the product of the likelihood function and prior distribution. The prior distribution is a probability distribution, which characterizes the uncertainty of the parameters before observations. The prior distribution prevents the estimates from moving to the boundary.

In this study, we assumed lognormal distribution as the prior distribution to represent the similarity in particle number between a pixel and the surrounding eight pixels. For N&B analysis, the assumption of similarity would be realistic, because of two reasons. (a) Diffraction limit: diffraction prevents a microscope from imaging the light emitted from a point light source. Even if the particle number changes sharply between a pixel and the surrounding eight pixels, the change would be alleviated. (b) Overlap of confocal volume during sampling: to maintain the lateral resolution, a pixel size smaller than the resolution is recommended. Confocal laser scanning microscopy scans the pixel size within a sampling time. During scanning, the illuminated area overlaps between the adjacent pixels if the confocal volume has a radius as large as the pixel size. We simply consider a fraction of the overlap in the x - y plane. In our measurement, we used an excitation wavelength of 488 nm and a numerical aperture of 1.2; further, we theoretically calculated the radius of the Airy disk (lateral resolution) as 248 nm. We set a pixel size of 146 nm and estimated the radius of the confocal volume as 214 nm by using FCS (see Materials and Methods in Supporting Material). The overlap fraction of the illuminated area can be calculated by $\pi r^2 / (\pi r^2 + 2sr)$, where r is the radius of the confocal volume and s is the pixel size (see Supporting Material for derivation). In our measurement, this fraction is 0.697, suggesting that the illuminated area does not change markedly in the adjacent pixels. To determine the parameters of the lognormal distribution, we applied the EB method to a pixel by using the surrounding eight pixels. The EB method is described later.

Double-detector model

We assumed that the prior distributions of the particle number ν and particle brightness ε are independent, and are given by lognormal and uniform distributions from 0 to ∞ , respectively. The joint posterior distribution is given by

$$P(v, \varepsilon | \mathbf{x}, \mathbf{y}, \hat{p}, \hat{\mu}, \hat{\sigma}) \propto \mathcal{L}(\mathbf{x}, \mathbf{y} | v, \varepsilon, \hat{p}) \text{LN}(v | \hat{\mu}, \hat{\sigma}) \text{Uni}(\varepsilon), \quad (32)$$

where \hat{p} is an estimate for p . We assumed that p can be approximated as a constant independent of the pixel position and measurements, and can be estimated prior to the measurements by using Eq. 19 ($\hat{p} = 0.5665$). The same assumption is used in the following. Further, $\hat{\mu}$ and $\hat{\sigma}$ are estimates given by the EB method; LN and Uni represent the lognormal and uniform distributions, respectively. We estimated the maximum of the joint posterior distribution using the Newton–Raphson method as before. Taking the logarithm of both sides on Eq. 32 and the derivative of the log-posterior distribution gives the equations required for the Newton–Raphson method. The first and second derivatives of $\log \mathcal{L}(\mathbf{x}, \mathbf{y} | v, \varepsilon, \hat{p})$ and $\log \text{LN}(v | \hat{\mu}, \hat{\sigma})$ are given by Eq. 13 and 14, and

$$\begin{aligned} \frac{\partial^2 \log \mathcal{L}}{\partial v^2}(\mathbf{x}, \mathbf{y} | v, \varepsilon, \hat{p}) \\ = -\frac{1}{v^2 \varepsilon} S_1(\mathbf{x} + \mathbf{y}, v, \varepsilon) + \frac{1}{v^2 \varepsilon^2} S_2(\mathbf{x} + \mathbf{y}, v, \varepsilon) - \frac{1}{v^2 \varepsilon^2} S_3(\mathbf{x} + \mathbf{y}, v, \varepsilon), \end{aligned} \quad (33)$$

$$\frac{\partial^2 \log \mathcal{L}}{\partial v \partial \varepsilon}(\mathbf{x}, \mathbf{y} | v, \varepsilon, \hat{p}) = -\frac{1}{v \varepsilon^2} S_2(\mathbf{x} + \mathbf{y}, v, \varepsilon) + \frac{1}{v \varepsilon^2} S_3(\mathbf{x} + \mathbf{y}, v, \varepsilon), \quad (34)$$

$$\frac{\partial^2 \log \mathcal{L}}{\partial \varepsilon^2}(\mathbf{x}, \mathbf{y} | v, \varepsilon, \hat{p}) = -\frac{1}{\varepsilon^2} S_0(\mathbf{x} + \mathbf{y}) + \frac{1}{\varepsilon^2} S_2(\mathbf{x} + \mathbf{y}, v, \varepsilon) - \frac{1}{\varepsilon^2} S_3(\mathbf{x} + \mathbf{y}, v, \varepsilon), \quad (35)$$

$$\frac{\partial \log \text{LN}}{\partial v}(v | \hat{\mu}, \hat{\sigma}) = -\frac{1}{v} - \frac{\log v - \hat{\mu}}{\hat{\sigma}^2 v}, \quad (36)$$

$$\frac{\partial^2 \log \text{LN}}{\partial v^2}(v | \hat{\mu}, \hat{\sigma}) = \frac{1}{v^2} + \frac{\log v - \hat{\mu} - 1}{\hat{\sigma}^2 v^2}. \quad (37)$$

For the initial values of $v^{(0)}$ and $\varepsilon^{(0)}$, the k -th iteration process of the Newton–Raphson method ($k = 1, 2, 3, \dots$) is given by Eq. 31 by replacing $\log \mathcal{L}$ with $\log P(v, \varepsilon | \mathbf{x}, \mathbf{y}, \hat{p}, \hat{\mu}, \hat{\sigma})$.

Dead-time-affected double-detector model

The joint posterior distribution is given by

$$P(v, \varepsilon | \mathbf{x}, \mathbf{y}, \hat{p}, \delta_1, \delta_2, \hat{\mu}, \hat{\sigma}) \propto \mathcal{L}(\mathbf{x}, \mathbf{y} | v, \varepsilon, \hat{p}, \delta_1, \delta_2) \text{LN}(v | \hat{\mu}, \hat{\sigma}) \text{Uni}(\varepsilon). \quad (38)$$

To find the maximum of the posterior distribution, we used the Newton–Raphson method for two variables as done previously. The first and second derivatives of the log-posterior distribution are given by those of the log-likelihood and log-prior distribution, which are given by Eq. 25, 36, and 37. The

iteration process of the Newton–Raphson method is given by Eq. 31 by replacing $\log \mathcal{L}$ with $\log P(\nu, \varepsilon | \mathbf{x}, \mathbf{y}, \hat{p}, \delta_1, \delta_2, \hat{\mu}, \hat{\sigma})$.

5.3.4 Empirical Bayes method

Lognormal prior model

As mentioned above, we assumed that the particle number distributions of a pixel (center pixel) and the surrounding eight pixels are given by identical lognormal distributions. The parameter of the lognormal distribution is a hyperparameter, and we estimated the hyperparameters μ and σ for predicting the center pixel by using the surrounding eight pixels. In this study, we estimated the hyperparameters using the EB method (26, 27); this method determines the hyperparameters by maximizing the marginal likelihood. To find the maximum point, we used the expectation maximization (EM) algorithm (26, 27). We simply write the joint posterior distribution on the surrounding pixels with $\nu_{1:J} = (\nu_1, \nu_2, \dots, \nu_J)$ and $\varepsilon_{1:J} = (\varepsilon_1, \varepsilon_2, \dots, \varepsilon_J)$ as follows:

$$P(\nu_{1:J}, \varepsilon_{1:J} | \mathbf{x}_{1:J}, \mathbf{y}_{1:J}, \hat{p}, \mu, \sigma) = \frac{1}{\mathcal{M}} \prod_{j=1}^J [\mathcal{L}(\mathbf{x}_j, \mathbf{y}_j | \nu_j, \varepsilon_j, \hat{p}) \text{LN}(\nu_j | \mu, \sigma) \text{Uni}(\varepsilon_j)], \quad (39)$$

where the subscript j represents the addresses between the surrounding pixels, subscript $1:J$ represents the vector of the addresses (in this study, $J = 8$). The photon count observations at each pixel are assumed to be conditionally independent given μ and σ . For MoM and ML, photon count observations at each pixel are assumed to be independent. \mathcal{M} is the marginal likelihood given by

$$\begin{aligned} \mathcal{M}(\mathbf{x}_{1:J}, \mathbf{y}_{1:J} | \hat{p}, \mu, \sigma) &= \int_0^\infty \int_0^\infty \prod_{j=1}^J [\mathcal{L}(\mathbf{x}_j, \mathbf{y}_j | \nu_j, \varepsilon_j, \hat{p}) \text{LN}(\nu_j | \mu, \sigma) \text{Uni}(\varepsilon_j)] d\nu_{1:J} d\varepsilon_{1:J} \\ &= \prod_{j=1}^J \left[\int_0^\infty \int_0^\infty \mathcal{L}(\mathbf{x}_j, \mathbf{y}_j | \nu_j, \varepsilon_j, \hat{p}) \text{LN}(\nu_j | \mu, \sigma) \text{Uni}(\varepsilon_j) d\nu_j d\varepsilon_j \right]. \end{aligned} \quad (40)$$

The EM algorithm is an iterative method to find the maximum, which is given by maximizing the following function $\mathcal{Q}(\mu, \sigma, \mu_{\text{old}}, \sigma_{\text{old}})$ (see Supporting Material for derivation):

$$\mathcal{Q}(\mu, \sigma, \mu_{\text{old}}, \sigma_{\text{old}}) = \sum_{j=1}^J \int_0^\infty \int_0^\infty P(\nu_j, \varepsilon_j | \mathbf{x}_j, \mathbf{y}_j, \hat{p}, \mu_{\text{old}}, \sigma_{\text{old}}) \log \text{LN}(\nu_j | \mu, \sigma) d\nu_j d\varepsilon_j. \quad (41)$$

The algorithm consists of an E step and an M step. The E step is a calculation step of expectations with the fixed hyperparameters μ_{old} and σ_{old} . The M step is a maximization step of $Q(\mu, \sigma, \mu_{\text{old}}, \sigma_{\text{old}})$ by changing the hyperparameters μ and σ . The first derivative of $Q(\mu, \sigma, \mu_{\text{old}}, \sigma_{\text{old}})$ is given by,

$$\frac{\partial Q}{\partial \mu}(\mu, \sigma, \mu_{\text{old}}, \sigma_{\text{old}}) = \frac{1}{\sigma^2} \sum_{j=1}^J \left[\mathbb{E}_{v_j, \varepsilon_j} [\log v_j] - \mu \right], \quad (42)$$

$$\frac{\partial Q}{\partial \sigma}(\mu, \sigma, \mu_{\text{old}}, \sigma_{\text{old}}) = \sum_{j=1}^J \left[-\frac{1}{\sigma} + \frac{\mathbb{E}_{v_j, \varepsilon_j} [(\log v_j - \mu)^2]}{\sigma^3} \right], \quad (43)$$

where $\mathbb{E}_{v_j, \varepsilon_j}[\]$ denotes an expectation with posterior distribution $P(v_j, \varepsilon_j, |x_j, y_j, \hat{p}, \mu_{\text{old}}, \sigma_{\text{old}})$. Setting the first derivatives to zero gives

$$\mu_{\text{new}} = \frac{1}{J} \sum_{j=1}^J \mathbb{E}_{v_j, \varepsilon_j} [\log v_j], \quad (44)$$

$$\sigma_{\text{new}} = \left(\frac{1}{J} \sum_{j=1}^J \mathbb{E}_{v_j, \varepsilon_j} [(\log v_j)^2] - \mu_{\text{new}}^2 \right)^{\frac{1}{2}}. \quad (45)$$

In this model, $\mathbb{E}_{v_j, \varepsilon_j} [\log v_j]$ and $\mathbb{E}_{v_j, \varepsilon_j} [(\log v_j)^2]$ are calculated in the E step, and μ_{new} and σ_{new} are estimated in the M step. The estimated μ_{new} and σ_{new} are used as μ_{old} and σ_{old} , respectively, in the following E step. The iteration of the E step and the M step continues until convergence.

Lognormal prior with gamma hyperprior model

In the previously described lognormal prior model, the EB method gives the estimates, and the estimates can be substituted for lognormal distribution $\text{LN}(v|\hat{\mu}, \hat{\sigma})$. The distribution enables the prediction of particle number in a pixel. However, the precision of the estimates is insufficiently high; thus, the prediction sometimes fails (see Fig S1.1 in Supporting Material). The low precision could be attributed to the small number of grouped pixels; especially, a low $\hat{\sigma}$ reduces the variance of the distribution, and the prediction fails to represent the variation in the particle number of grouped pixels. To avoid this problem, Chung et al. proposed to use gamma distribution as a hyperprior (28). A

hyperprior is a prior distribution for a hyperparameter, which acts as a penalty against a low $\hat{\sigma}$. A gamma hyperprior for σ is given by

$$\text{Gam}(\sigma|\alpha, \beta) = \frac{\beta^\alpha}{\Gamma(\alpha)} \sigma^{\alpha-1} \exp(-\beta\sigma), \quad (46)$$

where α and β are parameters taking a positive value ($0 < \alpha$, $0 < \beta$), $\Gamma(\alpha)$ is a gamma function, and $\Gamma(\alpha) = \int_0^\infty u^{\alpha-1} \exp(-u) du$. Chung et al. recommended to use $\alpha = 2$ and $\beta \rightarrow 0$ by default. In this study, we used $\alpha = J + 1$ and $\beta = 0.01J$ (we assumed $J = 8$; thus, $\alpha = 9$ and $\beta = 0.08$). We choose a pair of α and β to simplify the calculation in the M step and construct the gamma distribution with a mode of 100. With this choice, the 25th and 75th percentiles of the gamma distribution are $Q_{25} = 85.5$ and $Q_{75} = 135.0$, respectively. The gamma distribution works to positively increase $\hat{\sigma}$ and prevents the prediction from failing. Simply considering the default amount of particle number variation whose σ of 100 is given, the 25th and 75th percentiles for ν are $Q_{25} = 5.10 \times 10^{-30} \exp(\mu)$ and $Q_{75} = 1.96 \times 10^{29} \exp(\mu)$, respectively. The median of the distribution is given by $\exp(\mu)$. Although the percentiles depend on μ , the Q_{25} – Q_{75} interval would be regarded as sufficiently wide. An actual experimental range of the particle number in an N&B analysis would be $10^{-3} < \nu < 10^3$. With a small particle number, the fluorescence background and autofluorescence are not negligible. In contrast, with a large particle number, the fluorescence intensity increases, and the photon count saturation of the detectors is not negligible. The joint posterior distribution is given by

$$\begin{aligned} P(\nu_{1:J}, \varepsilon_{1:J} | \mathbf{x}_{1:J}, \mathbf{y}_{1:J}, \hat{\rho}, \mu, \sigma, \alpha, \beta) \\ = \frac{1}{\mathcal{M}} \prod_{j=1}^J [\mathcal{L}(\mathbf{x}_j, \mathbf{y}_j | \nu_j, \varepsilon_j, \hat{\rho}) \text{LN}(\nu_j | \mu, \sigma) \text{Uni}(\varepsilon_j)] \text{Gam}(\sigma | \alpha, \beta), \end{aligned} \quad (47)$$

where

$$\begin{aligned} \mathcal{M}(\mathbf{x}_{1:J}, \mathbf{y}_{1:J} | \hat{\rho}, \mu, \sigma, \alpha, \beta) \\ = \prod_{j=1}^J \left[\int_0^\infty \int_0^\infty \mathcal{L}(\mathbf{x}_j, \mathbf{y}_j | \nu_j, \varepsilon_j, \hat{\rho}) \text{LN}(\nu_j | \mu, \sigma) \text{Uni}(\varepsilon_j) d\nu_j d\varepsilon_j \right] \text{Gam}(\sigma | \alpha, \beta). \end{aligned} \quad (48)$$

\mathcal{Q} is given by (see Supporting Material for derivation),

$$\begin{aligned}
& \mathcal{Q}(\mu, \sigma, \mu_{\text{old}}, \sigma_{\text{old}}) \\
&= \sum_{j=1}^J \int_0^{\infty} \int_0^{\infty} P(v_j, \varepsilon_j, | \mathbf{x}_j, \mathbf{y}_j, \hat{p}, \mu_{\text{old}}, \sigma_{\text{old}}, \alpha, \beta) \log \text{LN}(v_j | \mu, \sigma) dv_j d\varepsilon_j \quad (49) \\
&+ \log \text{Gam}(\sigma | \alpha, \beta).
\end{aligned}$$

The first derivatives are given by

$$\frac{\partial \mathcal{Q}}{\partial \mu}(\mu, \sigma, \mu_{\text{old}}, \sigma_{\text{old}}) = \frac{1}{\sigma^2} \sum_{j=1}^J \left[\mathbb{E}_{v_j \varepsilon_j} [\log v_j] - \mu \right], \quad (50)$$

$$\frac{\partial \mathcal{Q}}{\partial \sigma}(\mu, \sigma, \mu_{\text{old}}, \sigma_{\text{old}}) = \sum_{j=1}^J \left[-\frac{1}{\sigma} + \frac{\mathbb{E}_{v_j \varepsilon_j} [(\log v_j - \mu)^2]}{\sigma^3} \right] + \frac{\alpha - 1}{\sigma} - \beta. \quad (51)$$

Setting the first derivatives to zero and substituting $\alpha = J + 1$ gives

$$\mu_{\text{new}} = \frac{1}{J} \sum_{j=1}^J \mathbb{E}_{v_j \varepsilon_j} [\log v_j], \quad (52)$$

$$\sigma_{\text{new}} = \left[\frac{J}{\beta} \left\{ \frac{1}{J} \sum_{j=1}^J \mathbb{E}_{v_j \varepsilon_j} [(\log v_j)^2] - \mu_{\text{new}}^2 \right\} \right]^{\frac{1}{3}}. \quad (53)$$

The model for a dead-time-affected detector is given by replacing $\mathcal{L}(\mathbf{x}_j, \mathbf{y}_j | v_j, \varepsilon_j, \hat{p})$ in Eq. 48 with $\mathcal{L}(\mathbf{x}_j, \mathbf{y}_j | v_j, \varepsilon_j, \hat{p}, \delta_1, \delta_2)$, and by replacing posterior distribution on the expectation.

5.4 Results

5.4.1 Comparison of different concentrations by simulation

To determine if the ML and EB-MAP methods produce estimates accurately and precisely, we simulated images imitating measurements with different concentrations. Fig. 2A–F show the variation in estimates given by MoM (Fig. 2A and 2D), ML (Fig. 2B and 2E), and EB-MAP (Fig. 2C and 2F). One thousand images were simulated with a fixed particle brightness of 10 kHz and different particle numbers.

Fig. 2A–C show the dependence of the estimated particle number on the true particle number. In

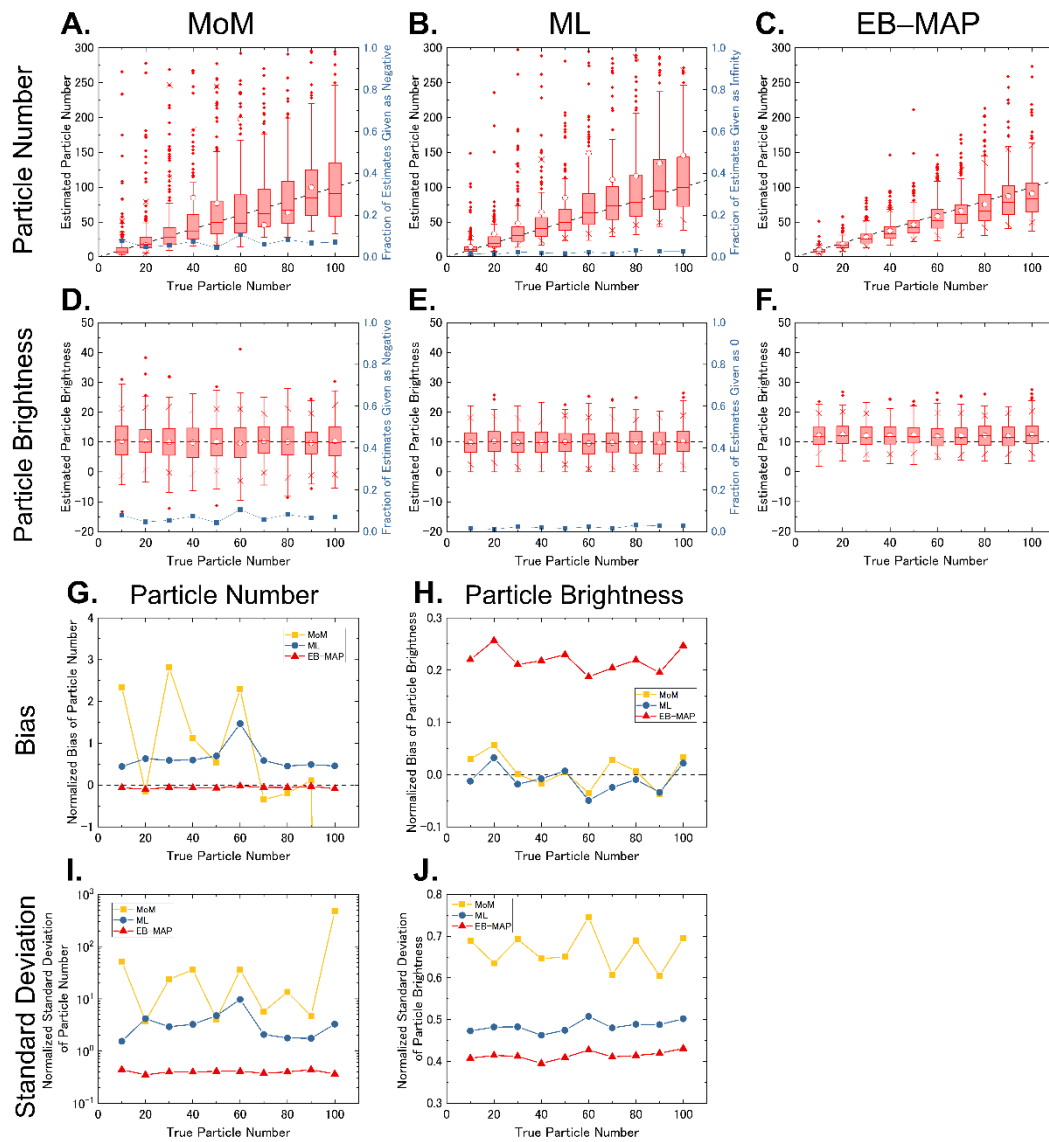


FIGURE 2: Simulations with different particle numbers

One thousand images were simulated with a fixed particle brightness of 10 kHz and different particle numbers, and analyzed by MoM (A, D), ML (B, E), and EB-MAP (C, F). (A, B, C) Dependence of the estimated particle number on true particle number. Dashed lines represent the true value. In the box plot, open circle: average, box: interval between 25th and 75th percentiles, central bar: median, diamonds: outliers, crosses: 5th and 95th percentiles, and the error bars are minimum and maximum points without outliers. Fig. 2A and 2B contain numerous outliers, which are shown in an enlarged view (see Fig. S2.1 in Supporting Material for broad view). In MoM and ML estimations, estimates are sometimes out of the parameter space; the fraction of estimates outside the parameter space is shown on the right axes. (D, E, F) Dependence of the estimated particle brightness [kHz] on true particle number. A fraction of estimates outside the parameter space is shown. (G–J) Normalized bias and standard deviation are shown for particle numbers (G, I) and particle brightness (H, J).

Fig. 2A, the averages are scattered around the true values and do not overlap with them. The medians are closer to the true values than to the averages. In Fig. 2B, the averages are overestimated, and the medians overlap with the true values. In Fig. 2C, the averages are close to the true values. Fig. 2G and 2I show the normalized bias and standard deviation of the particle number; the normalization is divided by the true value. A bias of 0 indicates accurate estimation, and a low standard deviation indicates high-precision estimation. Fig. 2G and 2I show that EB-MAP estimated the particle number with the highest accuracy and precision. The precision of EB-MAP estimation was an order of magnitude higher than that of MoM. Note that the bias and the standard deviation of ML were given by excluding the particle number of infinity; these values are only for reference. Fig. 2D-F show the dependence of the estimated particle brightness on the true particle number. For all the methods, the averages and the medians were close to the true value and were constant. The number of outliers was notably smaller than that estimated for the particle number. Fig. 2H and 2J show the normalized bias and standard deviation of the particle brightness. Fig. 2H indicates that MoM and ML estimated the particle brightness accurately, but EB-MAP overestimated the values. The magnitude of bias on EB-MAP was constant. Fig. 2J indicates that the estimation of EB-MAP was the most precise, that of ML was the second-best, and that of EB-MAP was 1.5 times better than that of MoM. One could consider that either the particle number or particle brightness would be underestimated if the other was overestimated in Fig. 2G and 2H. Although each estimate of MoM and ML satisfies Eq. 18, the average of the estimates does not satisfy such relation (see Supporting Material for details).

These results suggest that EB-MAP is more advantageous than MoM and ML for estimating the particle number. In contrast, the median of the estimates given by MoM and ML would be useful as a representative value. Moreover, Digman et al. (7) and our group (11) applied a spatial median filter to the images of the estimates in previous studies (see Fig. S2.2 in Supporting Material for the results regarding application of median filter). Regarding particle brightness, MoM and ML are advantageous for accurate estimation, but EB-MAP estimates with the highest precision.

5.4.2 Comparison of different laser powers or oligomeric states by simulation

Next, we simulated images imitating measurements with different laser powers or oligomeric states. One thousand images were simulated with a fixed particle number and varying particle brightness. In the simulation of the fixed particle number, we simulated a 2×2 grid-patterned area to demonstrate the applicability of the EB-MAP estimation. The EB-MAP implemented by lognormal prior with gamma hyperprior can be applied even if the particle number changes sharply (see Fig. S1.2 in Supporting Material).

Fig. 3A and 3B show the true and estimated particle numbers given by MoM, ML, and EB-MAP. In the image with the particle brightness of 20 kHz, the grid pattern was observed clearly for all the methods. In the images with lower particle brightness of 10 and 5 kHz, many outliers appeared in the

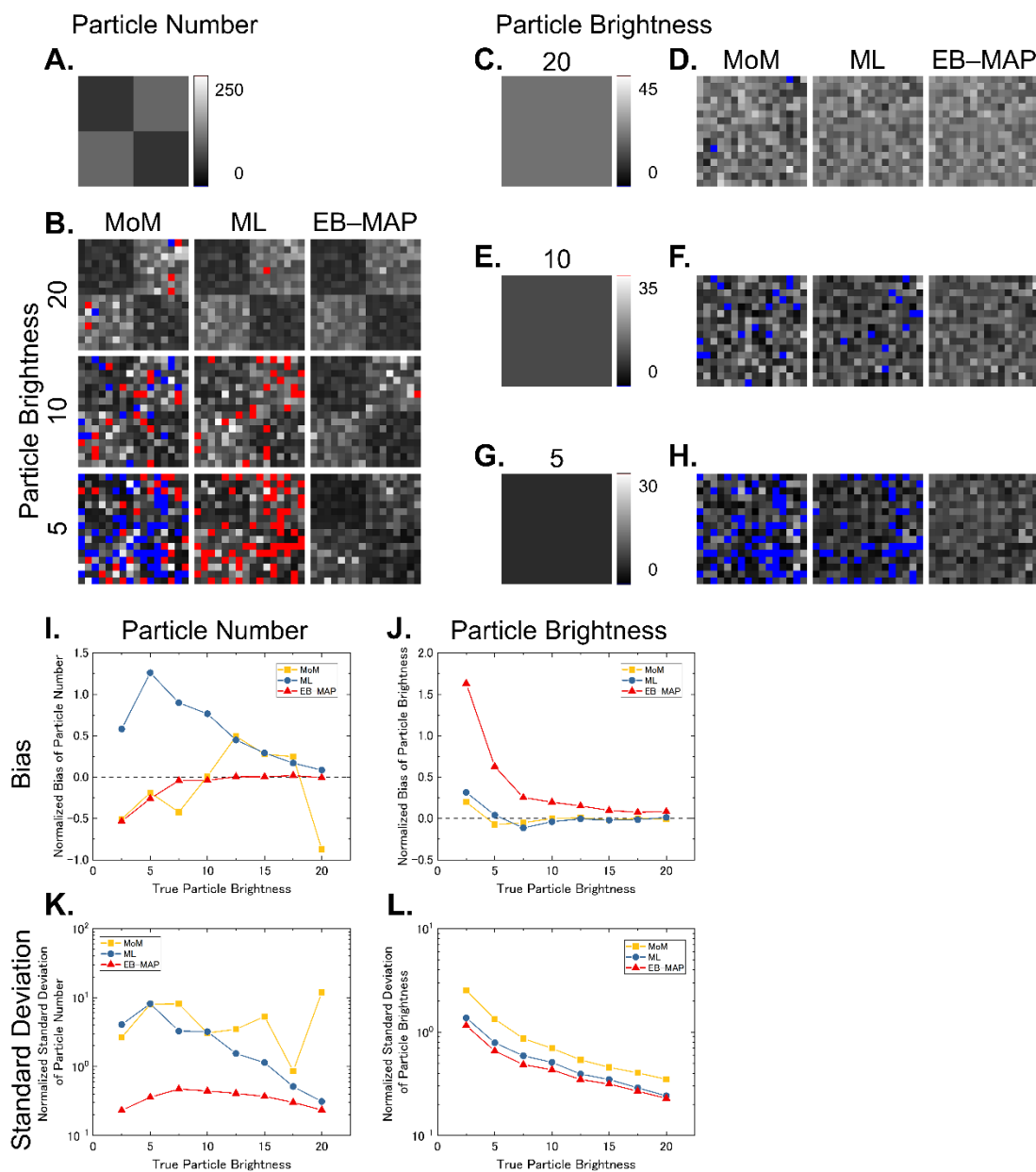


FIGURE 3: Simulations with different particle brightness on grid-patterned image

One thousand images were simulated with a fixed particle number and different particle brightness. The particle number has a 2×2 grid-patterned area, in which each pixel has 50 or 100 particles. (A) True image for particle number. (B) Estimated images for the particle number given by MoM, ML, and EB-MAP under different particle brightness [kHz]. The brightness and contrast of the images are the same between A and B. The pixels below the range are colored in blue, and those beyond the range are colored in red. (C, E, G) True images for the particle brightness of 20, 10, and 5 kHz, respectively. (D, F, H) Estimated images for particle brightness [kHz]. The brightness and contrast of the images are the same between C and D, E and F, and G and H. (I-L) Normalized bias and standard deviation for a true particle number of 100 particles (I, K) and particle brightness (J, L).

MoM and ML methods. However, outliers were very small in number, and the edge of the grid pattern was stored, in the case of the EB–MAP method. Fig. 3I and 3K show the normalized bias and standard deviation of the particle number, respectively (see Fig. S3.1 in Supporting Material for box plot). As seen from Fig. 3I, MoM estimated unstably, and sometimes overestimated and underestimated. Further, ML markedly overestimated at lower particle brightness; EB–MAP estimated with a bias of 0 for a particle brightness of over 7.5 kHz and underestimated for a particle brightness of less than 7.5 kHz. As seen in Fig. 3K, ML and EB–MAP estimated more precisely compared with MoM. The precision of EB–MAP estimation was an order of magnitude better than that of MoM. Fig. 3C–H show the true and estimated particle brightness. Although outliers were fewer in number, MoM and ML sometimes estimated negatively if the true particle brightness was low. Fig. 3J and 3L show the normalized bias and standard deviation of the particle brightness, respectively. As seen from Fig. 3J, MoM and ML estimated accurately, except for a true particle brightness of 2.5 kHz; however, EB–MAP markedly overestimated if the true particle brightness was low. Fig. 3L shows that ML and EB–MAP estimated more precisely compared with MoM. To carefully examine the bias produced by MoM and ML, we performed another simulation with a particle brightness of less than 5 kHz (see Fig. S3.4 in Supporting Material). The results showed that MoM underestimated and ML overestimated, if the true particle brightness was low. The magnitude of bias of ML was smaller than that of EB–MAP.

5.4.3 Experimental comparison of different concentrations

To demonstrate the applicability of ML and EB–MAP, we experimentally obtained images of the EGFP solution and analyzed them. In the previous simulations, we simulated the ideal photon counts based on Neyman type A distribution. However, the effect of the dead time on photon detectors cannot be neglected in actuality. We analyzed the images using MoM, ML, and EB–MAP, which can be applied to dead-time-affected photon counts (see Fig. S4.3 in Supporting Material for results without correction for dead time). For analyses based on MoM, we adopted the TD–N&B analysis (11), which does not require correction for dead time. This method is based on covariance and fluorescence intensity estimation; the covariance is not affected by dead time. Although the fluorescence intensity is affected by dead time, we assume that the effect is negligibly small in our measurements. This effect has been previously evaluated by Hillesheim et al. (29). As a control for N&B analysis, FCS measurements were also performed (see Fig. S4.4 in Supporting Material). We prepared different concentrations of EGFP using phosphate-buffered saline (pH 7.4). The average of fluorescence intensity increased with the concentration; we plotted the averages in the x -axis. It can be expected that increasing the concentration will increase the particle number, but the particle brightness will remain constant.

Fig. 4A shows the dependence of the average particle number on the average of fluorescence intensity (see Fig. S4.1 in Supporting Material for box plot) and fitted lines. Each line shows an

increase in particle number (see Table S4.3 in Supporting Material for details on parameters of the lines). For MoM, the averages were scattered around the fitted line. For ML, the averages were closer to the line, but a few were away from the line at high concentration. For EB-MAP, all the symbols of the average overlapped with the line. Fig. 4B shows the dependence of the average particle brightness on the average of the fluorescence intensity and fitted lines. For all the methods, the averages were close to the fitted line and showed a constant particle brightness. The particle brightness was the highest for EB-MAP and second-highest for ML. The magnitude relationship of particle brightness between MoM, ML, and EB-MAP was similar to that of the simulated result for low particle brightness (see Fig. S3.4 in Supporting Material). Fig. 4C and 4D show the standard deviations of the particle number and particle brightness, respectively. The ML and EB-MAP estimated more precisely compared with MoM. The precision of EB-MAP estimation was an order of magnitude better for particle number and 1.5 times better for particle brightness than those of MoM. These results are consistent with the simulated results.

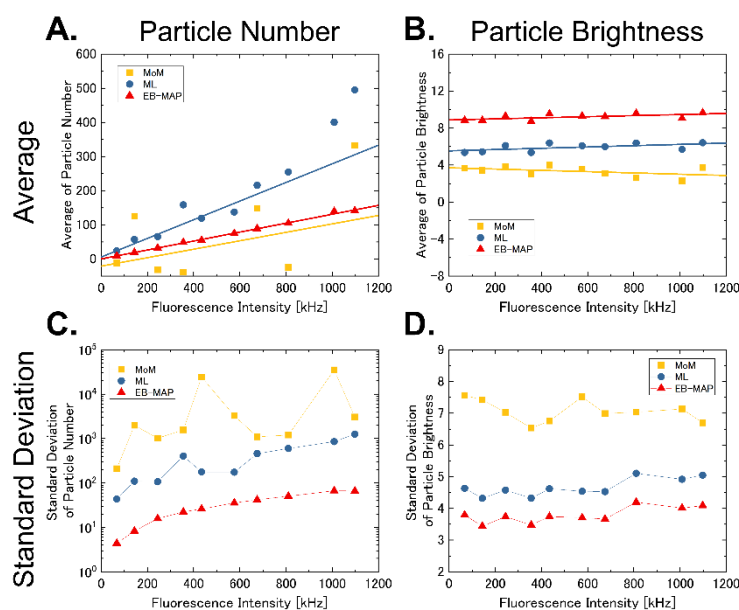


FIGURE 4: Experiments on EGFP solution with different concentrations

Dependence of average and standard deviation on the concentration for particle number (A, C) and particle brightness [kHz] (B, D). Fluorescence intensity is plotted on the x-axis, instead of the concentration. The solid lines in A and B are fitted lines obtained by the weighted least squares method.

5.4.4 Experimental comparison of different laser powers

Next, we obtained images of the EGFP solution with different laser powers and analyzed them. As a control, FCS measurements were also performed (see Fig. S5.3 in Supporting Material). It can be

expected that increasing the laser power will increase the particle brightness, but the particle number will remain constant.

Fig. 5A shows the dependence of average particle number on the laser power (see Fig. S5.1 in Supporting Material for box plot). For MoM, the averages had a large variation and were not constant. For ML, the averages increased roughly and seemed to become constant at high laser power, but did not increase monotonically. For EB-MAP, the averages increased and saturated at high laser power. The dotted line was arbitrarily drawn with a slope of 0 and an intercept of 53.1, which is an average of the first three largest values (i.e., the highest average, second-highest average, and third-highest average). Fig. 5B shows the dependence of the average particle brightness on the laser power. For all the methods, the averages were close to the fitted line and increased (see Table S5.3 in Supporting Material for details on parameters of the lines). For MoM, the lines had an intercept of nearly 0. In contrast, for ML and EB-MAP, although the fitted line characterized the averages precisely, the lines had positive intercepts. Fig. 5C and 5D show the standard deviations of the particle number and particle brightness, respectively. Both ML and EB-MAP estimated more precisely than MoM. The precision of EB-MAP estimation was an order of magnitude better for particle number and 1.5–2 times better for particle brightness than those of MoM. These results are consistent with the simulated results.

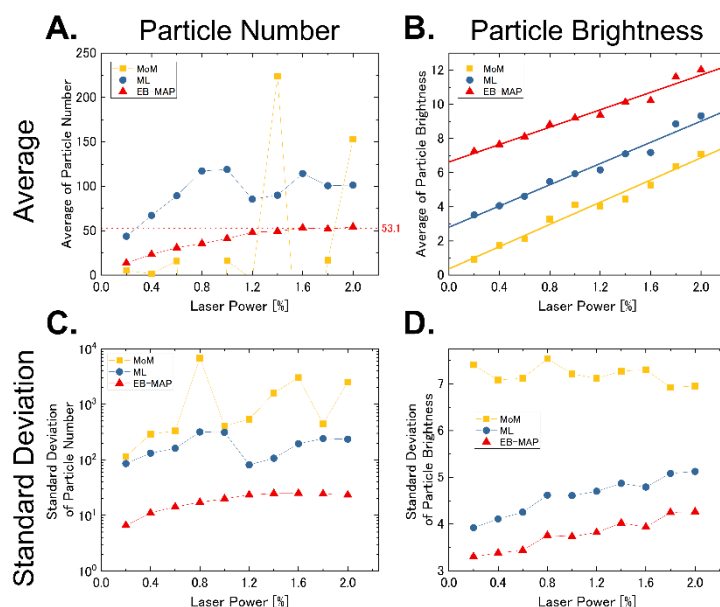


FIGURE 5: Experiments on EGFP solution with different laser power

Dependence of average and standard deviation on the laser power for particle number (A, C) and particle brightness [kHz] (B, D). The dotted line in A was arbitrarily drawn with a slope of 0 and an intercept of 53.1. The solid lines in B are fitted lines obtained by the weighted least squares method.

5.4.5 Experimental comparison of EGFP tandem oligomers

Finally, we prepared HeLa cells expressing the EGFP monomer, dimer, and trimer separately. The dimer and trimer are EGFP tandem-oligomers, and have flexibly linked two and three EGFP units, respectively. Increasing the EGFP unit will increase the particle brightness. We obtained their images and analyzed them. For quantification, we placed regions of interest (ROIs) of the size 16×16 in the nucleus and cytoplasm, and estimated the averages. Additionally, FCS measurements were also performed as a control (see Fig. S6.4 in Supporting Material).

Fig. 6A shows the fluorescence intensity of a cell expressing EGFP monomer, and Fig. 6B shows the particle number (see Fig. S6.1 and S6.2 in Supporting Material for other results). For MoM and ML, the outline of the nuclear membrane and cellular structure is not clear due to the presence of many outliers. On the other hand, for EB-MAP, there are no outliers and the contrast between the fluorescence intensity and particle number seems similar. The histogram of the particle number in the cytoplasm shows that EB-MAP suppressed the appearance of larger values (see Fig. S6.3 in Supporting Material). Fig. 6C–E show the dependence of the average particle brightness on the number of EGFP units, and Fig. 6F shows the normalized particle brightness and fold change in the particle brightness in the cytoplasm; the normalization is divided by the average of the average particle brightness of the monomer. The fold change in the particle brightness is the normalized average of averages. For MoM, increasing the number of EGFP units increased the average of averages in cytoplasm, and the average did not clearly increase from EGFP dimer to trimer in the nucleus. The fold change in particle brightness did not correspond with the number of EGFP units. The results of FCS were similar to those of MoM. All these results are consistent with the results of a previous study (11). For ML and EB-MAP, the averages were higher, and the fold changes were smaller than those of MoM. To examine the cause of the decreasing fold change, we subtracted the intercept obtained in Fig. 5B from the average particle brightness (the intercept is 2.80 and 6.62 for ML and EB-MAP, respectively), and calculated the fold change (indicated by “+” in Fig. 6F). The corrected fold changes of ML and EB-MAP were recovered and found to be equivalent to those of MoM.

5.5 Discussion

Thus far, we have demonstrated that EB-MAP can estimate precisely. In our statistical model, we did not include a model describing the point spread function (PSF) and scanning to reduce the computational cost. The spatial intensity distribution of the excitation light is described by PSF, and the position of a fluorescent particle in PSF affects the particle brightness. Additionally, scanning changes the position of the fluorescent particles in PSF. In a photon counting histogram (PCH) (21), the Gaussian-Lorentzian distribution and 3D Gaussian distribution are used for two-photon excitation and one-photon excitation (21), respectively. Including a model for PSF requires the calculation of

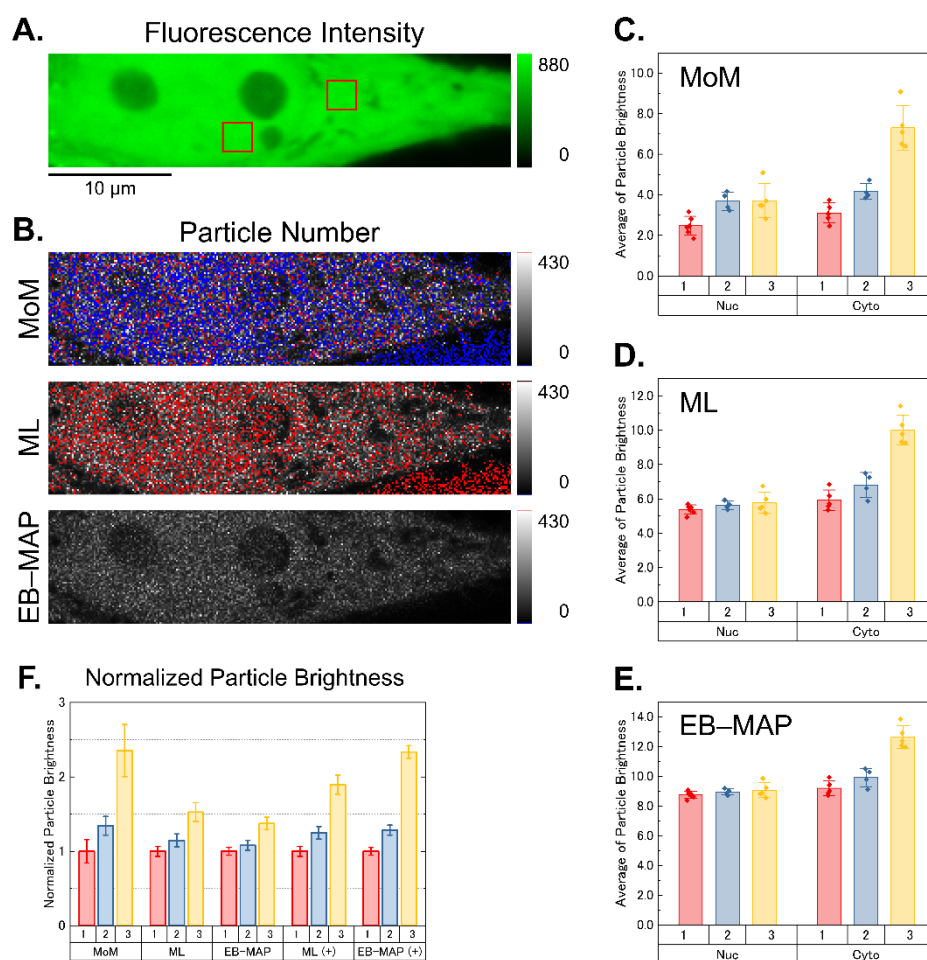


FIGURE 6: Experiments on EGFP tandem oligomers in cells

(A) Fluorescence intensity [kHz] of a cell expressing an EGFP monomer. The red squares are regions of interest (ROIs) placed in the nucleus and cytoplasm. (Please see the digital version of this figure because printed version could seem different.) (B) Estimated images for particle number analyzed by MoM, ML, and EB-MAP. The pixels below the range are colored in blue, and those beyond the range are colored in red. (C-E) Dependence of average particle brightness [kHz] on the number of EGFP units in the nucleus (Nuc) and cytoplasm (Cyto). Dots: sample average of particle brightness in the ROIs, bar: average of the averages, and error bar: sample standard deviation of the averages. (F) Normalized particle brightness in the cytoplasm. Bar: fold change in particle brightness (sample average of the normalized average particle brightness), error bar: sample standard deviation of the normalized average particle brightness. The symbol “+” represents the correction for particle brightness by subtracting the intercept in Fig. 5B.

convolution. Our algorithm for EB-MAP requires iterative computation for numerical integration; the iterative computation is required for each pixel. To prevent any further increase in computational cost, we did not include the model. Nevertheless, the dependence of the estimated particle number and

particle brightness on the sample concentration and laser power corresponded well with the theoretically expected relationship (see Fig. 4 and 5). These results suggest that our method characterized the intensity fluctuation comparatively. However, these results are not absolute estimations, and the estimates could be affected by a shape factor of the PSF described in PCH (21).

In the construction of prior distribution, we assumed lognormal distribution for the particle number; this assumption limits the particle number. In contrast, we assumed uniform distribution for the particle brightness; this assumption does not limit the particle brightness. Another construction of prior distribution is possible, i.e., limiting both the parameters. Such a prior distribution would be useful in further improving the precision. However, this construction increases the number of hyperparameters to be optimized simultaneously, and consequently increases the computational cost. Thus, we simplified the prior distribution and limited only the particle number. In future studies, a prior distribution limiting both the parameters would be required. Our assumption in the prior distribution ignored the distribution of particle brightness and the correlation between the particle number and particle brightness. However, the particle number and particle brightness correlate negatively on the likelihood function. Ignoring the particle brightness in the prior distribution would result in omitted-variable bias (30) (Chapter 3.3), which could have been a possible cause for the overestimated particle brightness in EB-MAP (Fig. 3J). To construct a prior distribution limiting both the parameters, an orthogonal parameterization (31) would be useful to eliminate the correlation of the parameters.

In fluorescence imaging and N&B analysis, the background intensity is a problem. For example, dark count, stray light, and autofluorescence would be sources of background intensity. Dark count and stray light can be corrected by implementing an additional probability distribution such as Poisson distribution, and by estimating the intensity of the background by a reference measurement. However, the correction for autofluorescence is challenging, because the intensity of autofluorescence differs depending on the position in cell and the cellular structure. We assumed that the effect of background intensity can be suppressed by increasing the fluorescence intensity from the target particles. We measured cells with fluorescence intensity, to the maximum extent possible; therefore, we did not perform corrections for background in this research (see Materials and Methods in Supporting Material).

We simulated photon count images with different particle numbers (Fig. 2) and particle brightness (Fig. 3), and evaluated the bias and standard deviation. The evaluation of the bias and standard deviation suggested the following. (a) For estimating the particle number, EB-MAP would be better to improve the accuracy and precision; however, EB-MAP underestimates the particle number if the true particle brightness is low. (b) MoM and ML often cause outliers, which skews the average. The median would be useful to characterize the distribution instead. (c) For estimating the particle brightness, the choice of estimator would change depending on the purpose of the analyst. MoM would be a better choice if the analyst expects estimation with less bias. On the other hand, ML and EB-

MAP would be better if the analyst expects precise estimation, and already knows that the true particle brightness is constant or a correction for the bias is available.

We applied these methods to the images of EGFP solution with different concentrations (Fig. 4) and laser powers (Fig. 5). We analyzed the images with the models considering the dead-time effect; considering this effect enabled recovery of the behavior of the parameters on different concentrations (see Fig. S4.4 in Supporting Material for results without correction). This suggests that the consideration of dead time is essential.

In the estimations of particle number with different laser powers using EB-MAP (Fig. 5), the particle number increased with the increasing laser power and saturated at the highest laser power. Considering the simulated results, the saturated value of 53.1 would be an unbiased estimation, although the true particle number is unknown in the experiments. However, decreasing the laser power below 1.6% decreased the estimates. Although experiments with different concentrations (Fig. 4) were conducted with a laser power of less than 1.6%, increasing the concentration increased the particle number linearly. This suggests that an underestimated particle number would be comparable, if the true particle brightness is the same.

In the estimation of particle brightness with different laser powers (Fig. 5), EB-MAP estimated the highest average of particle brightness, and ML and MoM estimated the second- and third-highest averages, respectively. These estimates were characterized well by lines, and ML and EB-MAP had clear positive intercepts. This result indicates that doubling or tripling the true particle brightness does not proportionally increase the particle brightness estimated by ML and EB-MAP. Therefore, in the experiments with EGFP tandem oligomers, the fold change in particle brightness by ML and EB-MAP decreased compared with that of MoM (Fig. 6F). We calculated the fold change again by subtracting the intercept (indicated by “+”: ML (+) and EB-MAP (+) in Fig. 6F). This correction recovered the fold change in particle brightness by ML and EB-MAP to be equivalent to that of MoM. This result implies that although ML and EB-MAP overestimate the particle brightness, they could be useful for relative quantification of particle brightness. The theoretical behavior of the estimated particle brightness was not investigated in detail in this study. Further studies are required for robust correction of the fold change. We performed simulations to investigate the origin of the positive intercept (see Fig. S5.4 in Supporting Material). The simulation results showed that the intercept decreased with the increasing number of images. The origin of the positive intercept would be the insufficient number of images at low particle brightness. Subtracting the intercept would compensate when sufficient number of images is not available. Further, the number of EGFP units did not correspond with the fold change obtained by MoM (Fig. 6C); this result is the same as that of FCS (see Fig. S6.4 in Supporting Material) and consistent with that of a previous study (11). These results suggest the presence of a non-fluorescent state of EGFP. There are several possible explanations for this phenomenon. One could be the photophysical processes, such as long-lived dark states (32) and photobleaching (33), and another

could be the chromophore formation (protein maturation and incorrect folding) (34–36). To estimate the number of EGFP units accurately, a simple correction method was proposed for the non-fluorescent state (35, 37). For error analyses on the fold change, see the sections in page 33–42, Supporting Material.

5.6 Conclusion

We applied ML and EB–MAP to N&B analysis to accurately and precisely estimate the particle number and particle brightness, which reflect the concentration and oligomeric state, respectively, of a fluorescently labeled protein in a cell. In the construction of EB–MAP, we effectively utilized the information of the surrounding pixels by assuming lognormal prior and gamma hyperprior. To extend the feasibility of our analysis, we combined the double-detector system achieved by a half mirror (11) and the correction for the dead time of photon detectors. We demonstrated the feasibility, accuracy, and precision of our method by simulations and experiments. The results showed that EB–MAP can be applied even if the particle number of the surrounding pixels changes sharply; further, EB–MAP estimated with better precision compared with that of the conventional method. Although EB–MAP overestimated the particle brightness, a simple correction recovered the fold change in particle brightness comparable to the conventional method. Our method (EB–MAP–N&B) recognizes the changes in parameters sensitively.

The N&B analysis is advantageous for monitoring the spatial distribution of the concentration and oligomeric state in cells. The measurement in this method is performed using confocal laser scanning microscopy. Our method has a wide range of applications in the field of fluorescence imaging. Furthermore, our method would contribute to the understanding of the dynamic processes in oligomerization and protein aggregation in cells.

5.7 References

SUPPORTING CITATIONS

References (40–53) appear in the Supporting Material.

1. Youker, R.T., and H. Teng. 2014. Measuring protein dynamics in live cells: protocols and practical considerations for fluorescence fluctuation microscopy. *J. Biomed. Opt.* 19:090801.
2. Bag, N., and T. Wohland. 2014. Imaging Fluorescence Fluctuation Spectroscopy: New Tools for Quantitative Bioimaging. *Annu. Rev. Phys. Chem.* 65:225–248.
3. Migueles-Ramirez, R.A., A.G. Velasco-Feliz, R. Pinto-Camara, C.D. Wood, and A. Guerrero. 2017. Fluorescence fluctuation spectroscopy in living cells. *Microsc. imaging Sci. Pract. approaches to Appl. Res. Educ.* 138–151.

4. Elson, E.L., and D. Magde. 1974. Fluorescence correlation spectroscopy. I. Conceptual basis and theory. *Biopolymers*. 13:1–27.
5. Krmpot, A.J., S.N. Nikolić, M. Vitali, D.K. Papadopoulos, S. Oasa, P. Thyberg, S. Tisa, M. Kinjo, L. Nilsson, W.J. Gehring, L. Terenius, R. Rigler, and V. Vukojević. 2015. Quantitative confocal fluorescence microscopy of dynamic processes by multifocal fluorescence correlation spectroscopy. In: *Advanced Microscopy Techniques IV*; and *Neurophotonics II*. OSA, Washington, D.C. p. 953600.
6. Yamamoto, J., S. Mikuni, and M. Kinjo. 2018. Multipoint fluorescence correlation spectroscopy using spatial light modulator. *Biomed. Opt. Express*. 9:5881.
7. Digman, M.A., R. Dalal, A.F. Horwitz, and E. Gratton. 2008. Mapping the Number of Molecules and Brightness in the Laser Scanning Microscope. *Biophys. J.* 94:2320–2332.
8. Qian, H., and E.L. Elson. 1990. On the analysis of high order moments of fluorescence fluctuations. *Biophys. J.* 57:375–380.
9. Qian, H., and E.L. Elson. 1990. Distribution of molecular aggregation by analysis of fluctuation moments. *Proc. Natl. Acad. Sci.* 87:5479–5483.
10. Saleh, B. 1978. Photoelectron statistics with applications to spectroscopy and optical communication. Springer-Verlag Berlin Heidelberg GmbH, .
11. Fukushima, R., J. Yamamoto, H. Ishikawa, and M. Kinjo. 2018. Two-detector number and brightness analysis reveals spatio-temporal oligomerization of proteins in living cells. *Methods*. 140–141:161–171.
12. Strey, H.H. 2019. Estimation of parameters from time traces originating from an Ornstein-Uhlenbeck process. *Phys. Rev. E*. 100:062142.
13. Jazani, S., I. Sgouralis, O.M. Shafraz, M. Levitus, S. Sivasankar, and S. Pressé. 2019. An alternative framework for fluorescence correlation spectroscopy. *Nat. Commun.* 10:3662.
14. Santra, K., J. Zhan, X. Song, E.A. Smith, N. Vaswani, and J.W. Petrich. 2016. What Is the Best Method to Fit Time-Resolved Data? A Comparison of the Residual Minimization and the Maximum Likelihood Techniques As Applied to Experimental Time-Correlated, Single-Photon Counting Data. *J. Phys. Chem. B*. 120:2484–2490.
15. Santra, K., E.A. Smith, J.W. Petrich, and X. Song. 2017. Photon Counting Data Analysis: Application of the Maximum Likelihood and Related Methods for the Determination of Lifetimes in Mixtures of Rose Bengal and Rhodamine B. *J. Phys. Chem. A*. 121:122–132.
16. Shenton, L.R. 1949. On the efficiency of the method of moments and Neyman's type A distribution. *Biometrika*. 36:450–454.
17. Shenton, L.R., and K.O. Bowman. 1967. Remarks on Large Sample Estimators for Some Discrete Distributions. *Technometrics*. 9:587–598.
18. Galindo Garre, F., and J.K. Vermunt. 2006. Avoiding Boundary Estimates in Latent Class

- Analysis by Bayesian Posterior Mode Estimation. *Behaviormetrika*. 33:43–59.
19. Allman, E., H.B. Cervantes, S. Hosten, K. Kubjas, D. Lemke, J. Rhodes, and P. Zwiernik. 2019. Maximum likelihood estimation of the Latent Class Model through model boundary decomposition. *J. Algebr. Stat.* 10:51–84.
 20. Mandel, L. 1958. Fluctuations of Photon Beams and their Correlations. *Proc. Phys. Soc.* 72:1037–1048.
 21. Chen, Y., J.D. Müller, P.T.C. So, and E. Gratton. 1999. The Photon Counting Histogram in Fluorescence Fluctuation Spectroscopy. *Biophys. J.* 77:553–567.
 22. Hillesheim, L.N., and J.D. Müller. 2005. The dual-color photon counting histogram with non-ideal photodetectors. *Biophys. J.* 89:3491–3507.
 23. Neyman, J. 1939. On a new class of “contagious” distributions, applicable in entomology and bacteriology. *Ann. Math. Stat.* 10:35–57.
 24. Adelson, R.. 1966. Compound Poisson Distributions. *Oper. Res. Soc.* 17:73–75.
 25. Hendrix, J., W. Schrimpf, M. Höller, and D.C. Lamb. 2013. Pulsed Interleaved Excitation Fluctuation Imaging. *Biophys. J.* 105:848–861.
 26. Bishop, C.M. 2006. Pattern Recognition and Machine Learning. Springer, Germany.
 27. Gelman, A., J. Carlin, H. Stern, and D. Rubin. 2004. Bayesian data analysis. 3rd ed. Chapman & Hall/CRC, UK.
 28. Chung, Y., S. Rabe-Hesketh, V. Dorie, A. Gelman, and J. Liu. 2013. A Nondegenerate Penalized Likelihood Estimator for Variance Parameters in Multilevel Models. *Psychometrika*. 78:685–709.
 29. Hillesheim, L.N., and J.D. Müller. 2003. The Photon Counting Histogram in Fluorescence Fluctuation Spectroscopy with Non-Ideal Photodetectors. *Biophys. J.* 85:1948–1958.
 30. Wooldridge, J.M. 2009. Introductory Econometrics: A Modern Approach. 5th ed. South-Western, Cengage Learning, USA.
 31. Willmot, G.E. 1988. Parameter Orthogonality for a Family of Discrete Distributions. *J. Am. Stat. Assoc.* 83:517–521.
 32. Widengren, J., Ü. Mets, and R. Rigler. 1999. Photodynamic properties of green fluorescent proteins investigated by fluorescence correlation spectroscopy. *Chem. Phys.* 250:171–186.
 33. Hur, K.-H., P.J. Macdonald, S. Berk, C.I. Angert, Y. Chen, and J.D. Mueller. 2014. Quantitative Measurement of Brightness from Living Cells in the Presence of Photodepletion. *PLoS One*. 9:e97440.
 34. Balleza, E., J.M. Kim, and P. Cluzel. 2018. Systematic characterization of maturation time of fluorescent proteins in living cells. *Nat. Methods*. 15:47–51.
 35. Dunsing, V., M. Luckner, B. Zühlke, R.A. Petazzi, A. Herrmann, and S. Chiantia. 2018. Optimal fluorescent protein tags for quantifying protein oligomerization in living cells. *Sci.*

- Rep.* 8:10634.
36. Foo, Y.H., N. Naredi-Rainer, D.C. Lamb, S. Ahmed, and T. Wohland. 2012. Factors affecting the quantification of biomolecular interactions by fluorescence cross-correlation spectroscopy. *Biophys. J.* 102:1174–1183.
 37. Vámosi, G., N. Mücke, G. Müller, J.W. Krieger, U. Curth, J. Langowski, and K. Tóth. 2016. EGFP oligomers as natural fluorescence and hydrodynamic standards. *Sci. Rep.* 6:33022.
 38. Petrášek, Z., and P. Schwillle. 2008. Scanning Fluorescence Correlation Spectroscopy. In: *Single Molecules and Nanotechnology*. Springer, Berlin, Heidelberg, . pp. 83–105.
 39. Kannan, B., J.Y. Har, P. Liu, I. Maruyama, J.L. Ding, and T. Wohland. 2006. Electron Multiplying Charge-Coupled Device Camera Based Fluorescence Correlation Spectroscopy. *Anal. Chem.* 78:3444–3451.
 40. Bédard, G. 1967. Dead-time corrections to the statistical distribution of photoelectrons. *Proc. Phys. Soc.* 90.
 41. Ackermann, J., and H. Hogueve. 2010. Small dead-time expansion in counting distributions and moments. *Nucl. Instruments Methods Phys. Res. Sect. A Accel. Spectrometers, Detect. Assoc. Equip.* 614:297–302.
 42. Oura, M., J. Yamamoto, H. Ishikawa, S. Mikuni, R. Fukushima, and M. Kinjo. 2016. Polarization-dependent fluorescence correlation spectroscopy for studying structural properties of proteins in living cell. *Sci. Rep.* 6:31091.
 43. Pack, C., K. Saito, M. Tamura, and M. Kinjo. 2006. Microenvironment and Effect of Energy Depletion in the Nucleus Analyzed by Mobility of Multiple Oligomeric EGFPs. *Biophys. J.* 91:3921–3936.
 44. Takahasi, H., and M. Mori. 1973. Double exponential formulas for numerical integration. *Publ. Res. Inst. Math. Sci.* 9:721–741.
 45. Müller, C.B., A. Loman, V. Pacheco, F. Koberling, D. Willbold, W. Richtering, and J. Enderlein. 2008. Precise measurement of diffusion by multi-color dual-focus fluorescence correlation spectroscopy. *Europhys. Lett.* 83:46001.
 46. Culbertson, C.T., S.C. Jacobson, and J. Michael Ramsey. 2002. Diffusion coefficient measurements in microfluidic devices. *Talanta.* 56:365–73.
 47. Amrhein, V., S. Greenland, and B. McShane. 2019. Scientists rise up against statistical significance. *Nature.* 567:305–307.
 48. Johnson, D.H. 1999. The Insignificance of Statistical Significance Testing. *J. Wildl. Manage.* 63:763.
 49. Lemoine, N.P. 2019. Moving beyond noninformative priors: why and how to choose weakly informative priors in Bayesian analyses. *Oikos.* 128:912–928.
 50. Gelman, A. 2006. Prior distributions for variance parameters in hierarchical models

- (comment on article by Browne and Draper). *Bayesian Anal.* 1:515–534.
51. Polson, N.G., and J.G. Scott. 2012. On the Half-Cauchy Prior for a Global Scale Parameter. *Bayesian Anal.* 7:887–902.
 52. R Core Team. 2020. R: A language and environment for statistical computing. R Foundation for Statistical Computing, Vienna, Austria. <https://www.r-project.org/>.
 53. Stan Development Team. 2020. RStan: the R interface to Stan. <http://mc-stan.org/>.

5.8 Supplemental Information

Empirical Bayes Method Using Surrounding Pixel Information for Number and Brightness Analysis

R. Fukushima, J. Yamamoto, M. Kinjo

Herein, we provide supplemental information to describe the theoretical derivations, materials and methods, and supplemental data in detail. First, we briefly describe the derivation of the equations in the main text. Then, we describe the simulation method, preparation of EGFP and cells, and measurement and analysis methods. Finally, in the supplemental data, we present additional results that complement the main text and figures.

5.8.1 Theoretical Derivations

Derivation of the recursive formula describing the probability distribution for photon count detected by double detectors

The probability distribution for observing X and Y photons by double detectors is given in Eq. 6. The equation is a summation of W time Bernoulli processes, and W is an independent random variable determined by a Neyman type A distribution. The probability-generating function is given by

$$\begin{aligned} G(z_1, z_2) &= \sum_{X=0}^{\infty} \sum_{Y=0}^{\infty} P(X, Y) z_1^X z_2^Y \\ &= \exp[\nu(\exp[\varepsilon(pz_1 + qz_2 - 1)] - 1)], \end{aligned} \quad (\text{S1})$$

where $p + q = 1$. The a -th order derivative of the probability-generating function with respect to z_1 is given as follows from mathematical induction ($a \geq 1$):

$$\frac{\partial^a G}{\partial z_1^a}(z_1, z_2) = \sum_{l=0}^{a-1} \binom{a-1}{l} \nu(\varepsilon p)^{a-l} \exp[\varepsilon(pz_1 + qz_2 - 1)] \frac{\partial^l G}{\partial z_1^l}(z_1, z_2). \quad (\text{S2})$$

The b -th order derivative of Eq. S2 with respect to z_2 is given as follows from mathematical induction ($b \geq 0$):

$$\begin{aligned} &\frac{\partial^{a+b} G}{\partial z_1^a \partial z_2^b}(z_1, z_2) \\ &= \sum_{m=0}^b \binom{b}{m} \sum_{l=0}^{a-1} \binom{a-1}{l} \nu \varepsilon^{a-l+b-m} p^{a-l} q^{b-m} \exp[\varepsilon(pz_1 + qz_2 - 1)] \frac{\partial^{l+m} G}{\partial z_1^l \partial z_2^m}(z_1, z_2). \end{aligned} \quad (\text{S3})$$

Substituting $z_1 = z_2 = 0$ into the definition of the probability-generating function yields

$$\frac{\partial^{a+b} G}{\partial z_1^a \partial z_2^b}(0,0) = a! b! P(a, b). \quad (\text{S4})$$

Substituting $z_1 = z_2 = 0$ and Eq. S4 into Eq. S3 gives

$$P(a, b) = \frac{1}{a} \nu \varepsilon p \exp[-\varepsilon] \sum_{m=0}^b \frac{(\varepsilon q)^{b-m}}{(b-m)!} \sum_{l=0}^{a-1} \frac{(\varepsilon p)^{a-l-1}}{(a-l-1)!} P(l, m). \quad (\text{S5})$$

Derivation of a photon-counting model for a dead-time-affected single detector

Bédard described the probability for dead-time-affected photon count (1). The probability distribution for observing W photons on a dead-time-affected detector is given as follows for $W < 1/\delta$:

$$\begin{aligned} P(W|\eta, \delta) &= \int_0^{\infty} P(W|\eta, I_0, \delta)P(I_0)dI_0 \\ &= \int_0^{\infty} \{F(W-1|\eta, I_0, \delta) - F(W|\eta, I_0, \delta)\}P(I_0)dI_0, \end{aligned} \quad (S6)$$

where the probability distribution F is given by

$$F(W|\eta, I_0, \delta) = \frac{\gamma\{W+1, \eta I_0(1-W\delta)\}}{W!}, \quad (S7)$$

where $\gamma(W+1, \xi)$ is an incomplete gamma function, and $\gamma(W+1, \xi) = \int_0^{\xi} u^W \exp(-u) du$. δ is obtained by dividing dead time τ by the sampling time ($\delta = \tau/T$). O'Donnell derived a Taylor expansion of the probability distribution from the first to third terms, and Ackermann and Hogreve derived that from the fourth to fifth terms (2). Hillesheim and Müller corrected the dead-time effect with the first term of the expansion (3, 4). We generalize this formulation and present it in a different form for our purpose of approximation. The Taylor expansion is given by

$$\begin{aligned} P(W|\eta, I_0, \delta) &= \sum_{k=0}^{\infty} \frac{\delta^k}{k!} \frac{\partial^k P}{\partial \delta^k}(W|\eta, I_0, 0) \\ &= \sum_{k=0}^{\infty} \frac{\delta^k}{k!} \left\{ \frac{\partial^k F}{\partial \delta^k}(W-1|\eta, I_0, 0) - \frac{\partial^k F}{\partial \delta^k}(W|\eta, I_0, 0) \right\}, \end{aligned} \quad (S8)$$

where the derivative of the distribution F is given as follows from mathematical induction ($k = 1, 2, 3, \dots$):

$$\frac{\partial^k F}{\partial \delta^k}(W|\eta, I_0, 0) = (W)^k \text{Poi}(W|\eta I_0) \sum_{l=0}^{k-1} \left[(-1)^{l+1} \binom{k-1}{l} (\eta I_0)^{k-l} \frac{W!}{(W-l)!} \right]. \quad (S9)$$

$\binom{a}{b}$ is a binomial coefficient given by $\binom{a}{b} = \frac{a!}{b!(a-b)!}$. Each term in the infinite series of Eq. S8 contains a Poisson distribution multiplied by $(\eta I_0)^k$: $\text{Poi}(W|\eta I_0)$, $(\eta I_0)\text{Poi}(W|\eta I_0)$, ...or

$(\eta I_0)^k \text{Poi}(W|\eta I_0)$. Such a Poisson distribution can be rewritten by using $(\eta I_0)^k \text{Poi}(W|\eta I_0) = (W+k)!/W! \text{Poi}(W+k|\eta I_0)$. The infinite series can be separated into multiple terms having $\text{Poi}(W+m|\eta I_0)$ and function $A_m(W, \delta)$ with $m = 0, 1, 2, \dots$ as follows:

$$P(W|\eta, I_0, \delta) = \sum_{m=0}^{\infty} A_m(W, \delta) \text{Poi}(W+m|\eta I_0). \quad (\text{S10})$$

Under our assumption, the probability distribution for observing W photons on a dead-time-affected detector is

$$P(W|\nu, \varepsilon, \delta) = \sum_{m=0}^{\infty} A_m(W, \delta) \text{Ney}(W+m|\nu, \varepsilon). \quad (\text{S11})$$

Derivation of a photon-counting model for dead-time-affected double detectors

For a double-detector system, the joint probability distribution for observing X and Y photons on dead-time-affected detectors is given as follows:

$$P(X, Y|\eta_1, \eta_2, \delta_1, \delta_2) = \int_0^{\infty} \int_0^{\infty} P(X|\eta_1, I_1, \delta_1) P(Y|\eta_2, I_2, \delta_2) P(I_1, I_2) dI_1 dI_2, \quad (\text{S12})$$

where δ_1 and δ_2 represent the dead time of each detector divided by the sampling time. Under our assumption, the joint probability is rewritten as follows for $X < 1/\delta_1$ and $Y < 1/\delta_2$ with $f = 0, 1, 2, \dots$ and $g = 0, 1, 2, \dots$:

$$\begin{aligned} P(X, Y|\nu, \varepsilon, p, \delta_1, \delta_2) &= \sum_{m=0}^{\infty} \sum_{h=0}^m A_h(X, \delta_1) A_{m-h}(Y, \delta_2) P(X+h, Y+m-h|\nu, \varepsilon, p) \\ &= A_0(X, \delta_1) A_0(Y, \delta_2) P(X, Y|\nu, \varepsilon, p) \\ &\quad + A_1(X, \delta_1) A_0(Y, \delta_2) P(X+1, Y|\nu, \varepsilon, p) \\ &\quad + A_0(X, \delta_1) A_1(Y, \delta_2) P(X, Y+1|\nu, \varepsilon, p) \\ &\quad + A_2(X, \delta_1) A_0(Y, \delta_2) P(X+2, Y|\nu, \varepsilon, p) \\ &\quad + A_1(X, \delta_1) A_1(Y, \delta_2) P(X+1, Y+1|\nu, \varepsilon, p) \\ &\quad + A_0(X, \delta_1) A_2(Y, \delta_2) P(X, Y+2|\nu, \varepsilon, p) + \dots \\ &\quad + A_f(X, \delta_1) A_g(Y, \delta_2) P(X+f, Y+g|\nu, \varepsilon, p). \end{aligned} \quad (\text{S13})$$

Derivation of Q function on expectation maximization algorithm

We describe the derivation of the Q function on lognormal prior with gamma hyperprior. Bishop described the details of the derivation generally (5) (Section 9.4, the EM Algorithm in General). The Q function on lognormal prior is derived similarly. The marginal likelihood is given in Eq. 48. The natural logarithm of the marginal likelihood is given by

$$\begin{aligned} \log \mathcal{M}(\mathbf{x}_{1:J}, \mathbf{y}_{1:J} | \hat{p}, \mu, \sigma, \alpha, \beta) \\ = \sum_{j=1}^J \left[\log \int_0^\infty \int_0^\infty \mathcal{L}(\mathbf{x}_j, \mathbf{y}_j | v_j, \varepsilon_j, \hat{p}) \text{LN}(v_j | \mu, \sigma) \text{Uni}(\varepsilon_j) dv_j d\varepsilon_j \right] \\ + \log \text{Gam}(\sigma | \alpha, \beta). \end{aligned} \quad (\text{S14})$$

We introduce a probability distribution $R(v_j, \varepsilon_j)$ and use Jensen's inequality as follows:

$$\begin{aligned} \log \mathcal{M}(\mathbf{x}_{1:J}, \mathbf{y}_{1:J} | \hat{p}, \mu, \sigma, \alpha, \beta) \\ = \sum_{j=1}^J \left[\log \int_0^\infty \int_0^\infty R(v_j, \varepsilon_j) \frac{\mathcal{L}(\mathbf{x}_j, \mathbf{y}_j | v_j, \varepsilon_j, \hat{p}) \text{LN}(v_j | \mu, \sigma) \text{Uni}(\varepsilon_j)}{R(v_j, \varepsilon_j)} dv_j d\varepsilon_j \right] \\ + \log \text{Gam}(\sigma | \alpha, \beta) \\ \geq \sum_{j=1}^J \left[\int_0^\infty \int_0^\infty R(v_j, \varepsilon_j) \log \frac{\mathcal{L}(\mathbf{x}_j, \mathbf{y}_j | v_j, \varepsilon_j, \hat{p}) \text{LN}(v_j | \mu, \sigma) \text{Uni}(\varepsilon_j)}{R(v_j, \varepsilon_j)} dv_j d\varepsilon_j \right] \\ + \log \text{Gam}(\sigma | \alpha, \beta) \\ = \sum_{j=1}^J \left[\int_0^\infty \int_0^\infty R(v_j, \varepsilon_j) \log \text{LN}(v_j | \mu, \sigma) dv_j d\varepsilon_j \right] + \log \text{Gam}(\sigma | \alpha, \beta) + \text{const.} \end{aligned} \quad (\text{S15})$$

The right-hand side of the last equation in Eq. S15 is a lower bound on the log-marginal likelihood. The lower bound is maximized with a fixed μ_{old} and σ_{old} when $R(v_j, \varepsilon_j)$ is equal to $P(v_j, \varepsilon_j, | \mathbf{x}_j, \mathbf{y}_j, \hat{p}, \mu_{\text{old}}, \sigma_{\text{old}}, \alpha, \beta)$, and the maximized lower bound is a Q function.

Derivation of overlap fraction

We simply consider the overlap fraction during scanning in the x - y plane. We assume that the confocal volume has a radius r and the microscope scans a pixel size s within a sampling time. The illuminated area within a sampling time is the trajectory that is given by moving the circular confocal volume along the line of scanning. The illuminated area is the summation of the areas of the circle

with a radius r and the rectangle with lengths of $2r$ and s for its two sides: $\pi r^2 + 2sr$. The overlapped area between the adjacent pixels is the circular area, and is thus given by πr^2 . Therefore, the overlap fraction is given by $\pi r^2 / (\pi r^2 + 2sr)$.

Relation between average of particle number, particle brightness, and photon count average

The product of the particle number and particle brightness is equal to the temporal average of the photon counts (Eq. 18) for MoM and ML. Either the particle number or particle brightness is underestimated if the other is overestimated. One could consider that these relations are the same for the average of the estimates as well, and that the results presented in Fig. 2 are doubtful. Fig. 2G shows an overestimation of the particle number, but Fig. 2H shows an accurate estimation of the particle brightness in MoM and ML. However, these relations are not the same for the average of the estimates. We present a counter-example below, wherein we assume that the spatial distribution of the particle number and the temporal average of the photon counts follow gamma distribution and delta distribution, respectively:

$$\text{Gam}(v|\alpha, \beta) = \frac{\beta^\alpha}{\Gamma(\alpha)} v^{\alpha-1} \exp(-\beta v), \quad (\text{S16})$$

$$\text{Del}(\lambda|d) = \begin{cases} \infty, & \lambda = d, \\ 0, & \lambda \neq d, \end{cases} \quad (\text{S17})$$

where λ is a random variable for the temporal average of photon counts. The assumption of delta distribution means that the temporal average of the photon counts is a constant d at any spatial position. The distribution of $1/v$ is an inverse gamma distribution, and $\varepsilon = \lambda/v$. The distribution of particle brightness is given by

$$P(\varepsilon|\alpha, \beta, d) = \frac{1}{d} \frac{\beta^\alpha}{\Gamma(\alpha)} \left(\frac{\varepsilon}{d}\right)^{-\alpha-1} \exp\left(-\frac{\beta d}{\varepsilon}\right). \quad (\text{S18})$$

The spatial average of the particle number and particle brightness is $\mathbb{E}[v] = \alpha/\beta$ and $\mathbb{E}[\varepsilon] = d\beta/(\alpha - 1)$, respectively. Therefore, the product of the averages is $\mathbb{E}[v]\mathbb{E}[\varepsilon] = ad/(\alpha - 1)$. In contrast, the spatial average of photon count averages is $\mathbb{E}[\lambda] = d$. The product of the averages is not equal to the average of the photon count averages, i.e., $\mathbb{E}[v]\mathbb{E}[\varepsilon] > \mathbb{E}[\lambda]$. For a sufficiently large α , the gamma distribution converges to normal distribution, and the product of averages is close to d . This discussion reveals that the results presented in Fig. 2 are not doubtful.

Appearance of negative particle number and particle brightness in MoM

In MoM, a negative value of the particle number and brightness is occasionally observed. The cause for this is an insufficient number of observations for covariance estimation. Let X_i and Y_i be a photon count at the i th observation ($i = 1, 2, \dots, I$) in detectors 1 and 2, respectively. The estimators for the particle number and brightness in TD-N&B are respectively as follows (6):

$$\hat{\nu} = \frac{\bar{X}\bar{Y}}{\bar{C}}, \quad (\text{S19})$$

$$\hat{\varepsilon} = \frac{(\bar{X} + \bar{Y})\bar{C}}{\bar{X}\bar{Y}}. \quad (\text{S20})$$

where \bar{X} and \bar{Y} are the sample average of X_i and Y_i , respectively, and \bar{C} is sample covariance. \bar{X} , \bar{Y} , and \bar{C} are given as follows:

$$\bar{X} = \frac{1}{I} \sum_{i=1}^I X_i, \quad (\text{S21})$$

$$\bar{Y} = \frac{1}{I} \sum_{i=1}^I Y_i, \quad (\text{S22})$$

$$\bar{C} = \frac{1}{I} \sum_{i=1}^I (X_i - \bar{X})(Y_i - \bar{Y}). \quad (\text{S23})$$

The expected values of the sample average and covariance are given from the probability-generating function (Eq. S1) as follows:

$$\mathbb{E}[\bar{X}] = p\nu\varepsilon, \quad (\text{S24})$$

$$\mathbb{E}[\bar{Y}] = (1 - p)\nu\varepsilon, \quad (\text{S25})$$

$$\mathbb{E}[\bar{C}] = p(1 - p)\nu\varepsilon^2. \quad (\text{S26})$$

If the number of observations is infinite, the estimators for particle number and brightness are equal to the true particle number and brightness, respectively; thus, the estimates are positive. However, there is no guarantee that the estimators are equal to the true ones if the number of observations is finite. Under finite observations, estimates are close to the true values, and deviate from the true value if the number of observations is insufficient. The sample covariance could become negative if the number of observations is insufficient. The negative value of the sample covariance results in negative values of particle number and brightness.

5.8.2 Materials and Methods

Simulation

Photon count images were numerically simulated using Microsoft Visual Studio Community 2017, version 15.9.10 (Microsoft, USA). All programs were written in Visual C++. A typical simulation of FCS must simulate the trajectories of diffusing particles, but the temporal fluctuation of the fluorescence intensity is independent in number and brightness (N&B) analysis; thus, we simulated the temporal fluctuation with independent generation of random numbers. We generated the random numbers by using functions implemented in the header “random.” The seeds for random numbers were generated by the function “std::random_device” and pseudorandom numbers were generated by the function “std::default_random_engine” and the seed. The pseudorandom numbers were transformed into distributions representing photon counts by using the functions “std::poisson_distribution” and “std::binomial_distribution.” The separation probability on binomial distribution was assumed to be 0.5665 (this value is the same as the experimentally estimated value). We did not add any noise and background, to simplify our model. The photon counts were simulated with a sampling time of 10 μ s. The frame size of the simulated images was 18 \times 18, and the pixels excluding the edge were analyzed. As a result, the particle number and brightness with the size of 16 \times 16 were obtained. One thousand images were simulated with a fixed particle brightness of 10 kHz and different particle numbers ($\nu = 10, 20, 30, 40, 50, 60, 70, 80, 90, \text{ and } 100$) (Fig. 2). Further, the frame was separated into 2 \times 2 grids, and 1000 images were simulated with a fixed particle number of 50 or 100 and different particle brightness ($\varepsilon = 0.025, 0.050, 0.075, 0.100, 0.125, 0.150, 0.175, \text{ and } 0.200$) (Fig. 3). These simulations were performed independently on each pixel.

Purification of EGFP

The EGFP was purified using the His-tag method, which has been described previously (6).

Preparation of EGFP tandem oligomer-transfected HeLa cells

HeLa cells were maintained at 37 $^{\circ}$ C under a humidified atmosphere of 5% CO₂ in a Dulbecco's Modified Eagle's Medium (DMEM; Sigma-Aldrich, USA) supplemented with 100 μ g/mL penicillin G (Sigma-Aldrich, USA) and 100 μ g/mL streptomycin (Sigma-Aldrich, USA). The HeLa cells were seeded into an 8-well chambered coverglass (#155411, Thermo Fisher Scientific, USA) and incubated for 24 h. The cells (1.5×10^4 cells) were then transfected with 0.02 μ g of EGFP-C1 plasmids encoding EGFP monomer, or plasmids encoding flexible linker (FL) linked EGFP tandem-oligomers (2–3 mer) (7, 8) using ViaFect (Promega, USA). The pCAGGS plasmid was added as necessary to increase the total amount of plasmids to 0.1 μ g. The cells were incubated for 24 h. The medium was then renewed, and incubation was continued for 24 h. The medium was renewed again before the measurements were performed.

Image acquisition for N&B analysis

Confocal fluorescence microscopy images were obtained using an LSM 510 META ConfoCor3 system (Carl Zeiss, Germany) with a C-Apochromat 40×/1.2W Corr objective (Carl Zeiss, Germany). The EGFP was excited at a wavelength of 488 nm. EGFP fluorescence was split into two channels by a half mirror, filtered using a long-pass filter (LP505), and detected by two avalanche photodiodes, which has been described previously (6). The pinhole size was 94 μm (1.32 airy unit). The zoom factor was $\times 6$, and the pixel size was 0.146 $\mu\text{m} \times 0.146 \mu\text{m}$. The X- and Y-scanning sizes were 256×64 pixels. The pixel dwell time was 6.39 μs , and the scanning was raster scan. Two thousand images were sequentially obtained. The laser had an output of 0.30 μW at the objective for 1.0% output (see Fig. S1.3 for details). For Fig. 4, the images were obtained with different dilution ratios of EGFP with a laser output of 1.0%. For Fig. 5, the images were obtained with different laser outputs (0.2, 0.4, 0.6, 0.8, 1.0, 1.2, 1.4, 1.6, 1.8, and 2.0%). For Fig. 6, the images of the cells were obtained with a laser output of 0.4%. To minimize the background intensity, we selected the cell having a fluorescence intensity greater than 400 kHz on average in the cytoplasm. The fluorescence intensity of the non-transfected cell was less than 20 kHz in an area where the fluorescence intensity was stationary. Thus, the fraction of the background intensity would be less than 0.05 in cytoplasm. On the other hand, the fluorescence intensity in the nucleus was lower than that in the cytoplasm for EGFP dimer and trimer. This could be because of the larger molecular size than an EGFP monomer; EGFP dimer and trimer are difficult to pass through nuclear pores. The fluorescence intensity in the nucleus was greater than 150 kHz on average. Thus, a fraction of the background intensity would be less than 0.13.

Analysis conditions

For analysis based on method of moments (MoM), we adopted two-detector number and brightness analysis (TD-N&B), which has been described previously (6). A method based on covariance estimation of photon count sequence and correction for dead time are not required. In this study, linear regression, boxcar filtering, and median filtering were not implemented, unlike in a previous study (6).

For maximum likelihood (ML) estimation and empirical Bayes–maximum a posteriori (EB–MAP) estimation, a statistical model without correction for dead time was applied to the simulated images. In contrast, a statistical model with correction for dead time was applied to the experimentally obtained images. We assumed the same dead time of 50 ns (performance data, EG&G, Canada) on both detectors ($\delta_1 = \delta_2 = 7.82 \times 10^{-3}$), and a separation probability \hat{p} of 0.5665. The estimated value and standard error for \hat{p} was 0.566565 ± 0.000031 . In the calculation of A_0 , A_1 , and A_2 , we approximated the summation in Eq. 10 by partial summation from 0 to 5, 1 to 5, and 2 to 5, respectively. Although the upper limit of the summation is $W + m$, the difference only slightly affects our result. This is because the difference between the total and partial summations is negligibly small. We plan

to calculate the total summation in future experiments.

In the Newton–Raphson method, the initial pairs of $\nu^{(0)}$ and $\varepsilon^{(0)}$ were determined by choosing the pair giving the maximum log-likelihood between candidates. The candidates were chosen arbitrarily within the interval of the parameters. The iteration process of the Newton–Raphson method was terminated when the relative error of the parameters was less than 1.0×10^{-6} for each parameter. The relative error was estimated as follows for $\nu^{(k)}$ and $\nu^{(k+1)}$: $\nu^{(k+1)}/\nu^{(k)} - 1$. The relative error for $\varepsilon^{(k)}$ was similarly estimated. In ML estimation, log-likelihood sometimes gives maximum on the boundary of the parameter space. In the iteration process, we considered the estimates as boundary estimates, $\hat{\nu}$ of infinity, and $\hat{\varepsilon}$ of 0, when the estimates did not satisfy the above termination condition after 100 iterations. To solve the simultaneous linear equations in Eq. 31, we used Boost uBLAS (<http://www.boost.org/libs/numeric/ublas/>) implemented in Boost C++ Libraries, version 1.72.0.

In the EM algorithm, the choice of the initial pair of μ_{old} and σ_{old} and the termination of the iteration process were the same as those in the Newton–Raphson method. EB–MAP estimation was not performed on the edge of the image because the number of surrounding pixels is less than 8. For numerical integration, we used a double exponential formula (9) implemented with the transformation $\exp(\pi/2 \sinh t)$. We calculated the double integral as iterated integral, and applied the transformation formula to the first and second integrals. The numerical integration was iteratively performed by doubling the number of nodes. The iteration was terminated when the relative error of the integral was less than 1.0×10^{-6} . The EM algorithm requires an iterative calculation of the double integral with different μ and σ . In the first integral with respect to ε , the integration does not depend on μ and σ . To reduce the computational costs, we recorded the integrated value of the first integral, and calculated the second integral iteratively using the recorded first integral. For the first integral, we truncated the infinite summation when the truncation error was less than 1.0×10^{-6} . For the second integral, we fixed the interval of t on the second integration as -2 to 3 ($3.36 \times 10^{-3} < \nu < 6.82 \times 10^6$), and confirmed that the truncation error is less than 1.0×10^{-6} at the endpoints. In this numerical integration, arithmetic computations were performed in a logarithmic scale to avoid underflow and overflow. For the analysis in Fig. 2, the typical computation time was 30 ms, 6 s, and 1400 s for MoM, ML, and EB–MAP, respectively.

Evaluation of analysis results

The fluorescence intensity was calculated by dividing the temporal average of the photon count by the sampling time. After estimations by MoM, ML, and EB–MAP, the variation of the estimates was shown by a box plot, and the sample average and sample standard deviation were estimated within the regions of interest (ROIs). In Fig. 2 and 3, the normalized bias for the particle number was estimated by $\bar{\nu}/\nu_{\text{true}} - 1$, where $\bar{\nu}$ is the sample average of the particle number and ν_{true} is the true particle

number. The normalized bias for particle brightness was similarly estimated. Normalized standard deviation was estimated from the sample standard deviation divided by true parameters. In the calculation of the sample average and sample standard deviation, infinite values were excluded, but negative values and 0 were included. Note that the fraction of the negative values in the particle number and particle brightness estimated by MoM is the same because the estimates of MoM satisfy Eq. 18. Further, the weighted least squares method was applied with the weight of sample variance (Fig. 4 and 5). One could consider that the negative values of particle number and brightness are non-physical and should be excluded when calculating the sample average. However, we do not recommend excluding the negative values. Fig. S3.5 shows the influence of negative values on the calculation of the normalized bias. Excluding negative values resulted in an overestimation of the normalized bias. Thus, we do not recommend excluding the negative values when calculating the sample average. Readers interested in why negative values appear may refer to the section above, “Appearance of negative particle number and particle brightness in MoM.”

For experiments with EGFP in solution, an ROI of size 16×16 was placed at the center of a 256×64 image of the estimates. For experiments with EGFP monomer, dimer, and trimer in a cell, the position of the ROIs of size 16×16 was chosen carefully within the nucleus and cytoplasm. Our theory assumed independent and identical distribution of the photon count sequence. Cell migration and photobleaching could be the causes of artifacts, owing to nonstationary changes in the sequence. We confirmed that the sequences are stationary on each pixel in the ROI. Strong distortion of the sequence would be easily identified, but weak distortion would be missed if the sequence is checked only pixel-by-pixel. To avoid missing the weak distortion, we additionally confirmed that the time sequence made by averaging the spatial photon counts in the ROIs is stationary.

FCS measurements

FCS measurements were performed using an LSM 510 META ConfoCor3 system (Carl Zeiss, Germany) with a C-Apochromat $40 \times / 1.2W$ Corr objective (Carl Zeiss, Germany). The EGFP was excited at a wavelength of 488 nm. EGFP fluorescence was split into two channels by a half mirror and filtered using a long-pass filter (LP505). The pinhole size was $66 \mu\text{m}$. The measurement duration was $10 \text{ s} \times 20$ times. In Fig. S5.3, the measurement duration was $20 \text{ s} \times 20$ times for the lowest and second-lowest laser power. A single-component diffusion model with one triplet state was used for curve-fitting:

$$G(\tau_{\text{cor}}) = \frac{1}{\nu_{\text{FCS}}} \left[1 + f_{\text{tri}} \exp\left(-\frac{\tau_{\text{cor}}}{\tau_{\text{tri}}}\right) \right] \left[1 + \frac{\tau_{\text{cor}}}{\tau_{\text{dif}}} \right]^{-1} \left[1 + \frac{\tau_{\text{cor}}}{\varphi^2 \tau_{\text{dif}}} \right]^{-\frac{1}{2}} + 1, \quad (\text{S27})$$

where $G(\tau_{\text{cor}})$ is a temporal correlation function, f_{tri} is a triplet fraction, τ_{tri} denotes the

relaxation time of triplet state, ν_{FCS} denotes the average number of fluorescent particles in the confocal volume, τ_{dif} is the diffusion time, and φ is a structure parameter representing the ratio of beam waist to the axial radius. After pinhole adjustment, the structure parameter was determined using a 10^{-7} M standard solution of rhodamine 6G, whose diffusion coefficient is known, i.e., $D_{\text{R6G}} = 414 \mu\text{m}^2/\text{s}$ (10, 11). The radius of confocal volume was calculated by $(4\tau_{\text{dif}}D_{\text{R6G}})^{0.5}$ theoretically. The particle brightness was calculated as a summation of count rate divided by the number of particles determined by curve-fitting with a cross correlation function. For Fig. 4, the measurements were performed with different dilution ratios of EGFP with a laser output of 1.0%. For Fig. 5, the measurements were performed with different laser outputs (0.2, 0.4, 0.6, 0.8, 1.0, 1.2, 1.4, 1.6, 1.8, and 2.0%). For Fig. 6, the measurements on cell were performed with a laser output of 0.2%.

5.8.3 Supplemental Data

Validation of construction for prior distribution with lognormally distributed particle number

In a single pixel analysis, MoM and ML estimations are conducted at each pixel on an image, and the neighboring pixels of the analyzed pixel play no role in this. In contrast, the EB–MAP estimation utilizes the information of the surrounding pixels. To verify the EB method, we simulated a lognormally distributed particle number and determined the hyperparameter using two models, namely, lognormal prior and lognormal prior with gamma hyperprior. The purpose is to choose the appropriate hyperparameters for prediction; hyperparameters representing ambiguous prediction are acceptable. Fig. S1.1A and S1.1B show the spatial distribution of the particle number. Fig. S1.1C and S1.1D show the estimated hyperparameters and the Q_{25} – Q_{75} interval, respectively, determined by lognormal prior.

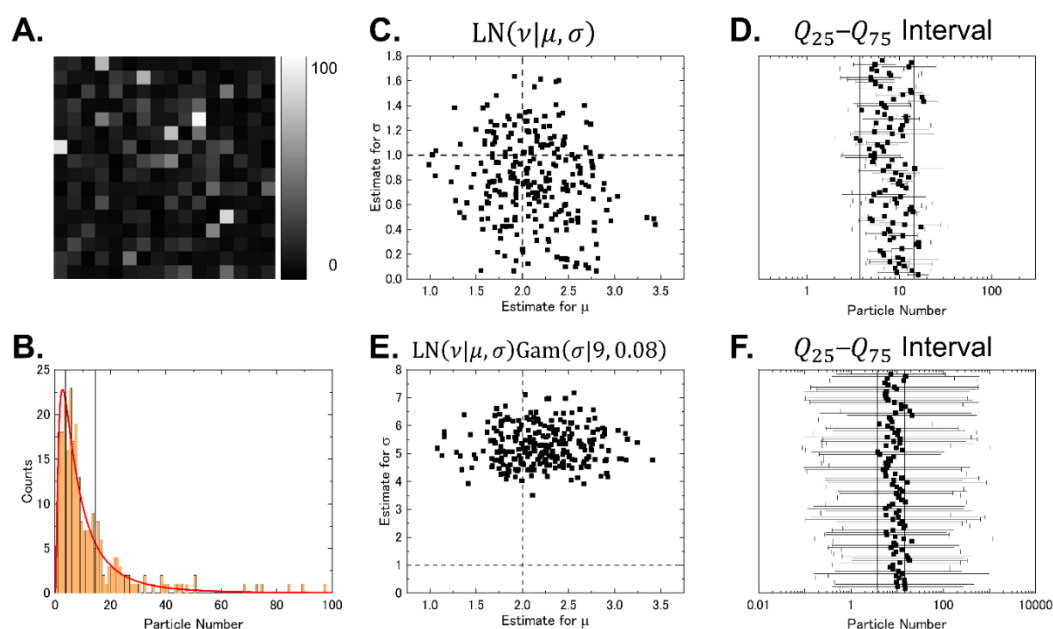


FIGURE S1.1: Comparison between prior models with lognormally distributed particle number

One thousand images were simulated with particle number and particle brightness of 10 kHz, and hyperparameters were estimated by the EB method with different models. The particle number was lognormally distributed independently ($\mu = 2$, $\sigma = 1$). (A) Spatial distribution of particle number. (B) Histogram of the particle number in A. The red curved line is a theoretical line of lognormal distribution. The black solid line shows the 25th and 75th percentiles of the distribution. (C, E) Scatter plot of the hyperparameters estimated by lognormal prior (C) and lognormal prior with gamma hyperprior (E). The dashed lines are true hyperparameters. (D, F) Q_{25} – Q_{75} interval of the lognormal distribution for which the estimated hyperparameters are substituted. The symbols show median, the error bars show the 25th and 75th percentiles of the lognormal distribution. The black solid lines show the 25th and 75th percentiles of the true distribution.

In Fig. S1.1C, the estimates are scattered around the intersection of the true values. In Fig. S1.1D, the estimated $Q_{25}-Q_{75}$ interval is sometimes shorter than the true one. These results suggest that underprediction of the $Q_{25}-Q_{75}$ interval occurs sometimes, which would cause bias. Thus, the lognormal prior model is not appropriate for the prediction of particle number. Fig. S1.1E and S1.1F show the estimated hyperparameters and the $Q_{25}-Q_{75}$ interval, respectively, determined by lognormal prior with gamma hyperprior. Fig. S1.1E shows that the estimates for σ increased, but those for μ did not change markedly as before. Fig. S1.1F shows that the estimated $Q_{25}-Q_{75}$ interval is wider than the true one. These results suggest that the prediction is ambiguous and it is difficult to miss the prediction, although the estimation of the hyperparameters is not accurate. Thus, the lognormal prior with gamma hyperprior can be applied to predict the particle number.

Validation of construction for prior distribution with grid-patterned particle number

In the lognormal prior model, a problem would arise if the distribution of the particle number on the surrounding pixels does not follow lognormal distribution. However, we assumed gamma distribution in addition to the lognormal distribution. The gamma distribution widens the lognormal distribution by increasing $\hat{\sigma}$. The wide prior distribution weakly constrains the estimation. It can be applied to predict distributions other than lognormal distribution. We simulated 2×2 grid-patterned images of the particle number to confirm that the presence of a sharp change in the surrounding pixels does not affect the estimation. The grid-patterned image has two types of area, each of which has the same particle number. The pixels have the particle number of 50 in one area, and 100 in the other.

Fig. S1.2A shows the distribution of the estimated $\hat{\mu}$ and $\hat{\sigma}$ for different particle brightness. At a low particle brightness, $\hat{\sigma}$ was estimated highly. Fig. S1.2B and S1.2C show the $Q_{25}-Q_{75}$ interval of the lognormal distribution for which $\hat{\mu}$ and $\hat{\sigma}$ were substituted. Fig. S1.2B shows the intervals for a particle brightness of 20 kHz. $\hat{\mu}$ inside the grid-patterned area having a particle number of 100 was close to the true value, and $\hat{\mu}$ on the edge of the grid-patterned area was smaller than the true value. The smaller $\hat{\mu}$ could have been caused by the adjacent pixels having a particle number of 50. The $Q_{25}-Q_{75}$ intervals contain the true value both on the edge and in the inner area, and they would be sufficiently wide to predict the particle number. Fig. S1.2C shows the intervals for a particle brightness of 5 kHz. The $Q_{25}-Q_{75}$ intervals were wider than those in Fig. S1.2B, and contain the true value. The lognormal prior with gamma hyperprior can be applied if the particle number changes sharply between the surrounding pixels.

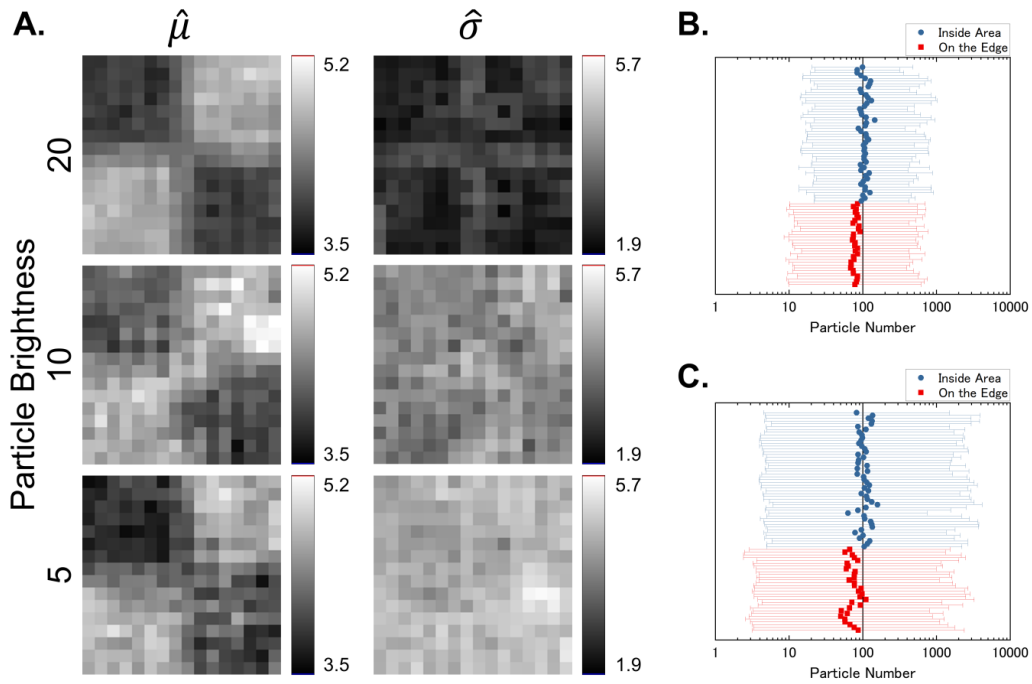
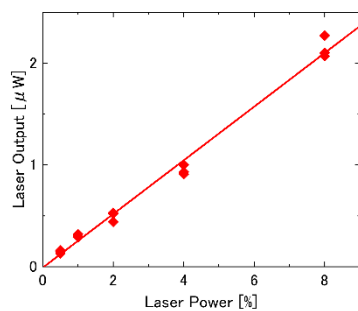


FIGURE S1.2: Optimization of hyperparameters by lognormal prior with gamma hyperprior on grid-patterned particle number

Simulation condition is the same as that in Fig. 3. (A) Spatial distribution of estimated hyperparameters with different particle brightness [kHz]. (B, C) $Q_{25}-Q_{75}$ interval of the lognormal distribution for which the estimated hyperparameters are substituted. The intervals are shown for a particle brightness of 20 kHz (B) and 5 kHz (C). The symbols represent median, and error bars represent the 25th and 75th percentiles of the lognormal distribution. All plots belong to the area with the true particle number of 100. The results on the edge of the area are colored in red, and those inside the area are colored in blue. The black solid lines denote the particle number of 100.

Relation between laser power setting and actual output**FIGURE S1.3: Dependence of actual laser output on laser power setting**

The solid line is a fitted line obtained by the least square method (see Table S1.1 for details on parameters of the line).

Slope	Intercept
0.2636 ± 0.0074	$(-0.9 \pm 3.1) \times 10^{-2}$

TABLE S1.1: Slope and intercept for the fitted line in Fig. S1.3

Estimated value and standard error

Supplemental data for Fig. 2

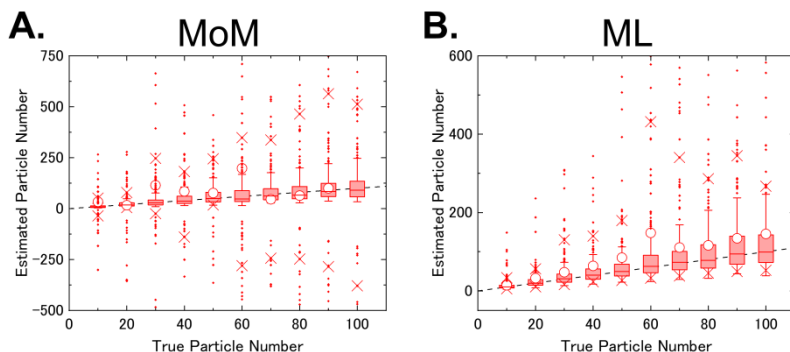


FIGURE S2.1: Broad view of estimated particle number in Fig. 2A and 2B

The view is adjusted to show the 5th and 95th percentiles of the particle number. The plots are shown similarly in Fig. 2. The minimum and maximum values are shown in Table S2.1 and S2.2. (A) Broad view of Fig. 2A. (B) Broad view of Fig. 2B.

True Particle Number	Minimum	Maximum
10	-1.439×10^3	7.999×10^3
20	-6.468×10^2	2.782×10^2
30	-1.251×10^3	1.020×10^4
40	-4.913×10^3	2.217×10^4
50	-8.467×10^2	1.795×10^3
60	-2.181×10^3	3.442×10^4
70	-3.832×10^3	9.617×10^2
80	-1.168×10^4	1.118×10^4
90	-4.259×10^3	3.290×10^3
100	-7.638×10^5	2.478×10^3

TABLE S2.1: Minimum and maximum values of estimated particle number in Fig. 2A

True Particle Number	Minimum	Maximum
10	4.493	1.488×10^2
20	7.980	1.102×10^3
30	1.372×10	1.258×10^3
40	1.717×10	1.798×10^3
50	2.256×10	3.578×10^3
60	2.372×10	8.799×10^3
70	2.918×10	1.661×10^3
80	3.196×10	1.612×10^3
90	4.362×10	1.675×10^3
100	3.847×10	5.089×10^3

TABLE S2.2: Minimum and maximum values of estimated particle number in Fig. 2B

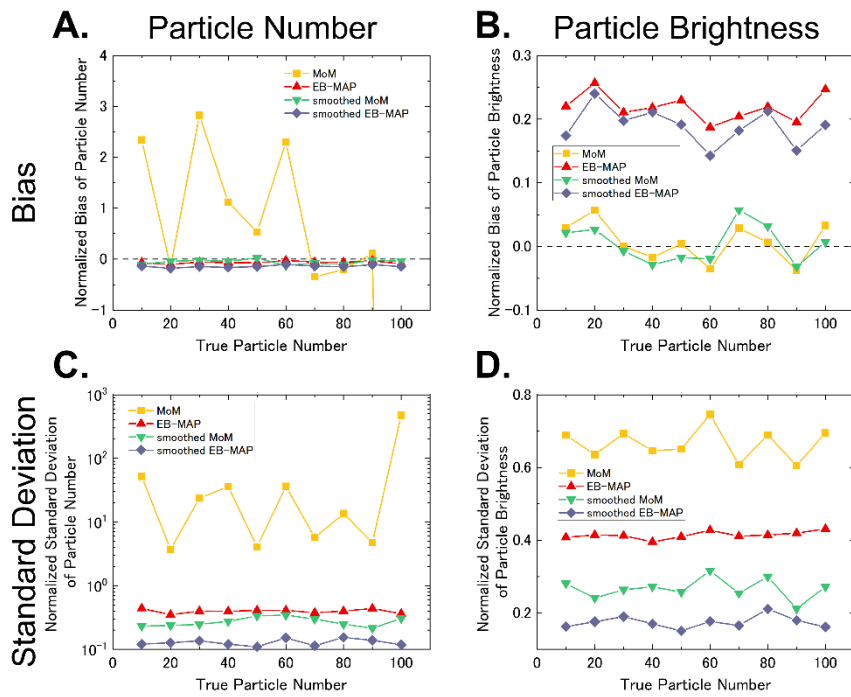


FIGURE S2.2: Noise smoothing by median filter

For noise smoothing, a median filter of size 3×3 was applied to the result of MoM and EB-MAP in Fig. 2.

Normalized bias and standard deviation are shown for particle numbers (A, C) and particle brightness (B, D).

Supplemental data for Fig. 3

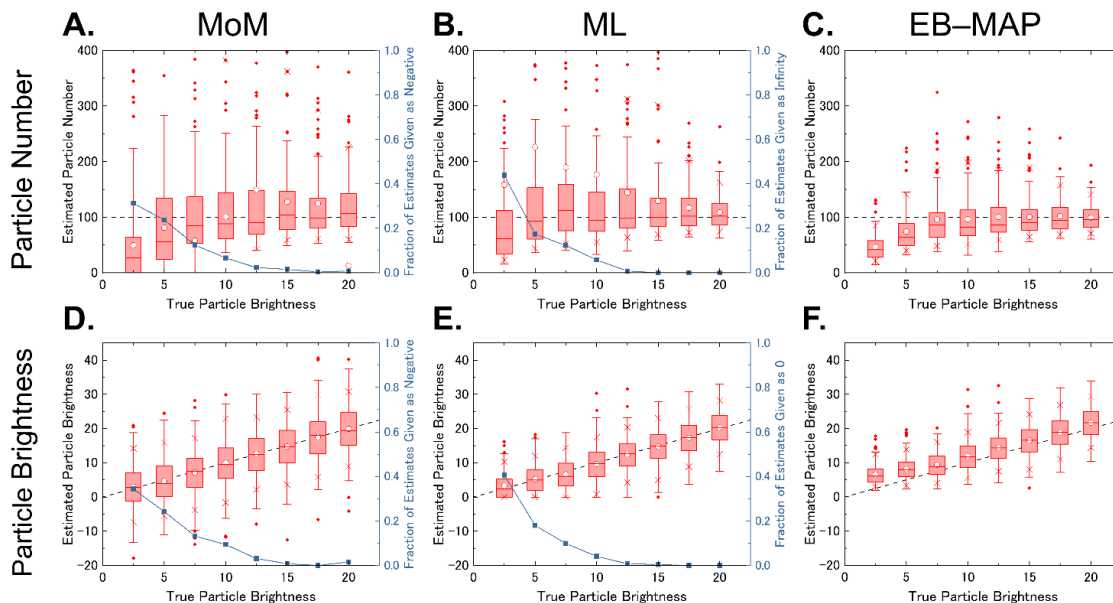


FIGURE S3.1: Variation in estimates for different particle brightness

One thousand images were simulated with a fixed particle number and different particle brightness, and analyzed by MoM (A, D), ML (B, E), and EB-MAP (C, F). (A, B, C) Dependence of estimated particle number on true particle brightness [kHz]. The particle number is shown for the area having a true particle number of 100. Figures S3.1A and S3.1B are shown in enlarged view (see Fig. S3.2 for broad view). (D, E, F) Dependence of estimated particle brightness [kHz] on true particle brightness. All figures are shown similarly in Fig. 2.

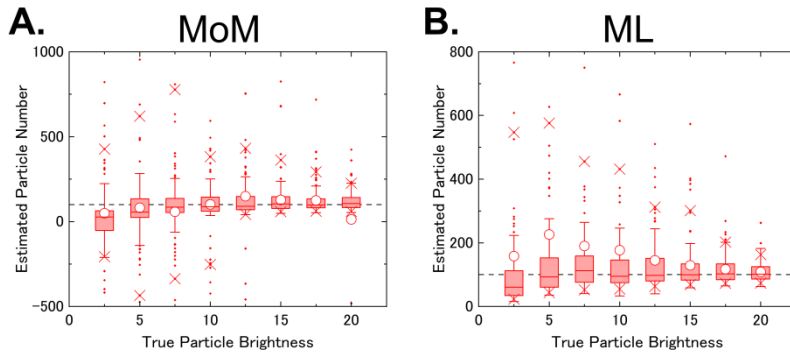


FIGURE S3.2: Broad view of estimated particle number in Fig. S3.1A and S3.1B

The view is adjusted to show the 5th and 95th percentiles of the particle number. The minimum and maximum values are listed in Table S3.1 and S3.2. (A) Broad view of Fig. S3.1A. (B) Broad view of Fig. S3.1B.

True Particle Brightness	Minimum	Maximum
2.5	-1.331×10^4	4.244×10^2
5.0	5.244×10	7.188×10^2
7.5	-4.770×10^3	3.087×10^3
10.0	-1.656×10^3	2.922×10^3
12.5	-1.140×10^3	2.357×10^3
15.0	-7.794×10^3	2.485×10^3
17.5	-5.578×10^3	5.790×10^3
20.0	-5.123×10^2	1.851×10^3

TABLE S3.1: Minimum and maximum values of the estimated particle number in Fig. S3.1A

True Particle Brightness	Minimum	Maximum
2.5	6.250×10	2.629×10^2
5.0	6.454×10	4.720×10^2
7.5	5.863×10	1.092×10^3
10.0	3.974×10	1.380×10^3
12.5	3.290×10	2.492×10^3
15.0	4.023×10	2.583×10^3
17.5	3.595×10	8.441×10^3
20.0	1.561×10	3.534×10^3

TABLE S3.2: Minimum and maximum values of the estimated particle number in Fig. S3.1B

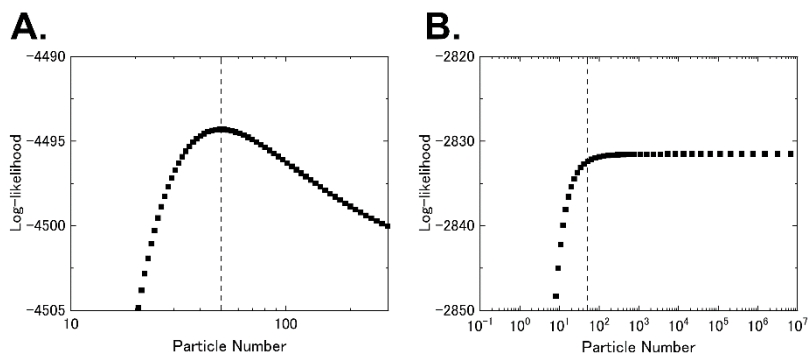


FIGURE S3.3: Shape of likelihood function

Typical results obtained by simulation in Fig. 3. Shape of the likelihood function when the ML estimate is (A) not on the boundary and (B) on the boundary. The dashed lines show the true value of particle number. The images were simulated with a particle brightness of (A) 20 kHz and (B) 5 kHz.

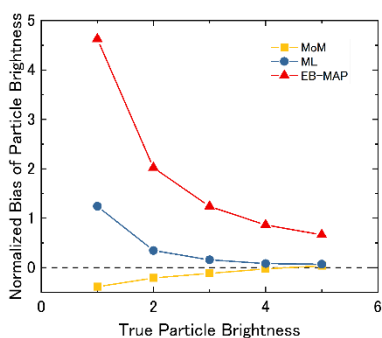


FIGURE S3.4: Normalized Bias of particle brightness

One thousand images were simulated with a fixed particle number of 100 and different particle brightness, and analyzed by MoM, ML, and EB-MAP. The size of the simulated images is 34×34 , and the bias was estimated by excluding the edge of the image (32×32 pixels).

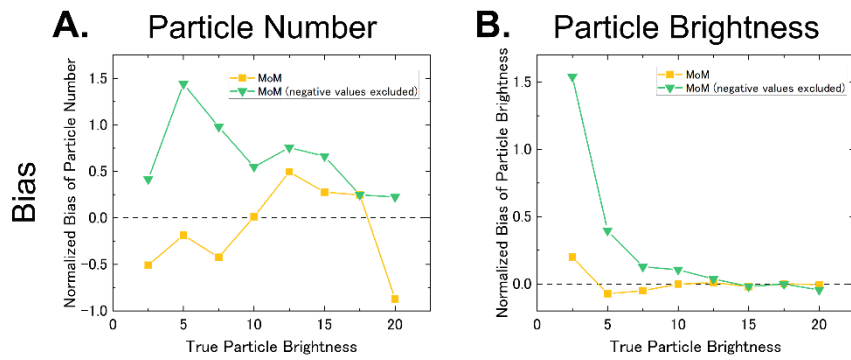


FIGURE S3.5: Influence of negative values on normalized bias

Normalized bias was estimated by excluding negative values in the results of Fig. 3. (A, B) Normalized bias for true particle number of 100 particles (A) and particle brightness (B).

Supplemental data for Fig. 4

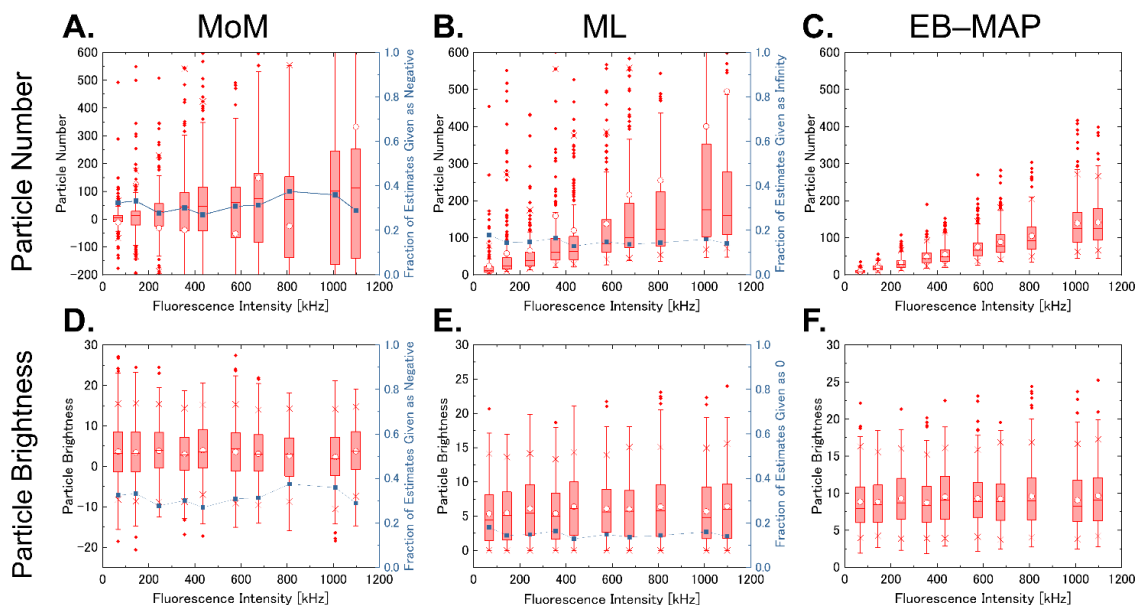


FIGURE S4.1: Variation in estimates for different concentrations

Two thousand images were obtained with different concentrations, and analyzed by MoM (A, D), ML (B, E), and EB-MAP (C, F). (A, B, C) Dependence of the estimated particle number on fluorescence intensity [kHz]. Figure S4.1A and S4.1B are shown in enlarged view (see Fig. S4.2 for broad view). (D, E, F) Dependence of the estimated particle brightness [kHz] on fluorescence intensity [kHz]. All figures are shown similarly in Fig. 2.

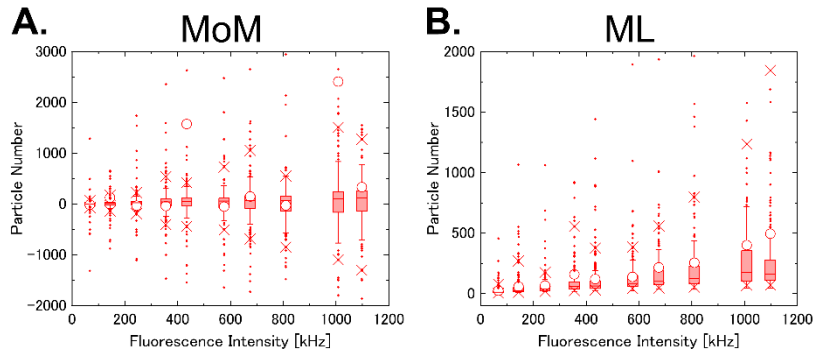


FIGURE S4.2: Broad view of estimated particle number in Fig. S4.1A and S4.1B

The view is adjusted to show the 5th and 95th percentiles of the particle number. The minimum and maximum values are listed in Table S4.1 and S4.2. (A) Broad view of Fig. S4.1A. (B) Broad view of Fig. S4.1B.

Fluorescence Intensity [kHz]	Minimum	Maximum
1.098×10^3	-5.550×10^3	3.751×10^4
1.009×10^3	-9.695×10^3	5.607×10^5
8.100×10^2	-1.030×10^4	7.708×10^3
6.750×10^2	-2.347×10^3	1.297×10^4
5.762×10^2	-4.709×10^4	1.948×10^4
4.344×10^2	-1.030×10^4	3.871×10^5
3.554×10^2	-1.882×10^4	8.033×10^3
2.442×10^2	-1.589×10^4	1.738×10^3
1.438×10^2	-3.185×10^3	3.144×10^4
6.725×10	-2.501×10^3	1.287×10^3

TABLE S4.1: Minimum and maximum values of the estimated particle number in Fig. S4.1A

Fluorescence Intensity [kHz]	Minimum	Maximum
1.098×10^3	4.760×10	9.735×10^3
1.009×10^3	4.654×10	8.153×10^3
8.100×10^2	3.524×10	7.532×10^3
6.750×10^2	3.879×10	5.165×10^3
5.762×10^2	2.668×10	1.895×10^3
4.344×10^2	2.104×10	1.442×10^3
3.554×10^2	1.942×10	3.386×10^3
2.442×10^2	1.278×10	1.061×10^3
1.438×10^2	8.527	1.066×10^3
6.725×10	3.227	4.544×10^2

TABLE S4.2: Minimum and maximum values of the estimated particle number in Fig. S4.1B

	Slope	Intercept
MoM	$(1.24 \pm 0.74) \times 10^{-1}$	-21 ± 16
ML	$(2.73 \pm 0.27) \times 10^{-1}$	5.9 ± 5.7
EB-MAP	$(1.307 \pm 0.016) \times 10^{-1}$	0.41 ± 0.30

	Slope	Intercept
MoM	$(-6.9 \pm 5.0) \times 10^{-4}$	3.71 ± 0.32
ML	$(7.0 \pm 3.6) \times 10^{-4}$	5.54 ± 0.22
EB-MAP	$(5.8 \pm 2.7) \times 10^{-4}$	8.89 ± 0.17

TABLE S4.3: Slope and intercept for the fitted line in Fig. 4A

Estimated value and standard error

TABLE S4.4: Slope and intercept for the fitted line in Fig. 4B

Estimated value and standard error

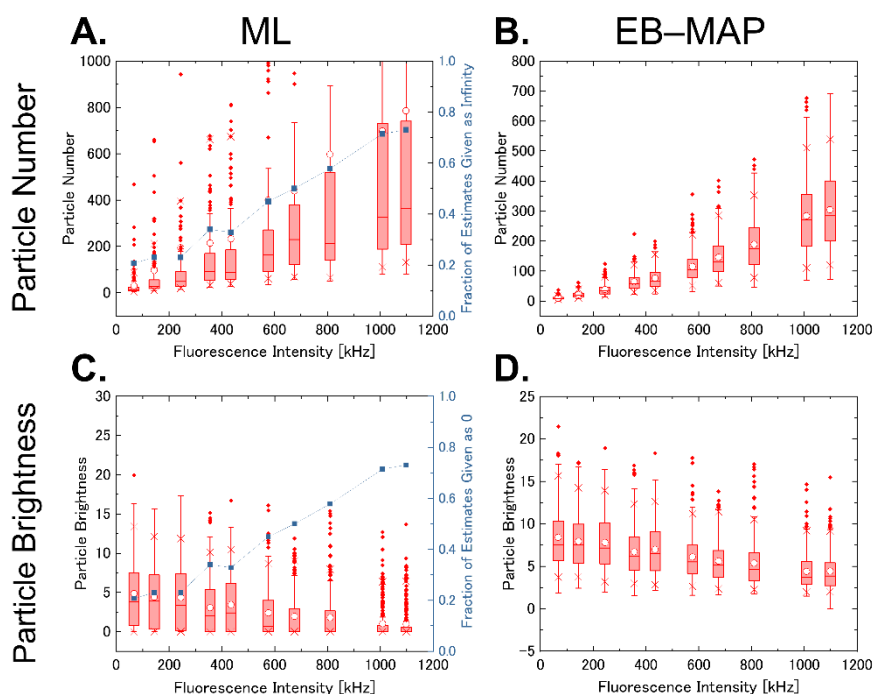


FIGURE S4.3: Variation in estimates without correction for dead time

The images for analysis are the same as those in Fig. 4 and Fig. S4.1, and were analyzed by ML (A, C) and EB-MAP (B, D) without correction for dead time. (A, B) Dependence of the estimated particle number on fluorescence intensity. (C, D) Dependence of the estimated particle brightness [kHz] on fluorescence intensity. All figures are shown similarly in Fig. 2.

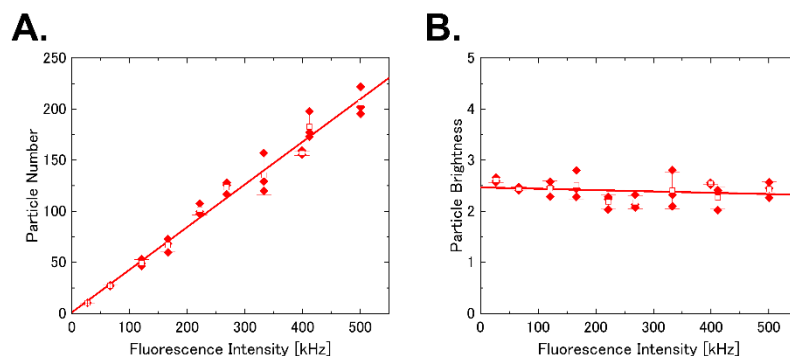


FIGURE S4.4: Estimation by FCS with different concentration

FCS measurements on EGFP solution with different concentrations. (A) Dependence of the estimated particle number on fluorescence intensity. (B) Dependence of the estimated particle brightness [kHz] on fluorescence intensity. In the plot, diamonds: results obtained from a single measurement, open squares: averages, and error bars: standard deviations. The solid lines are fitted lines obtained by the least squares method (see Table S4.5 for details on parameters of the lines).

	Slope	Intercept
Particle Number	0.417 ± 0.013	1.2 ± 3.7
Particle Brightness	$(-2.6 \pm 2.5) \times 10^{-4}$	2.466 ± 0.074

TABLE S4.5: Slope and intercept for the fitted line in Fig. S4.4A and S4.4B

Estimated value and standard error

Supplemental data for Fig. 5

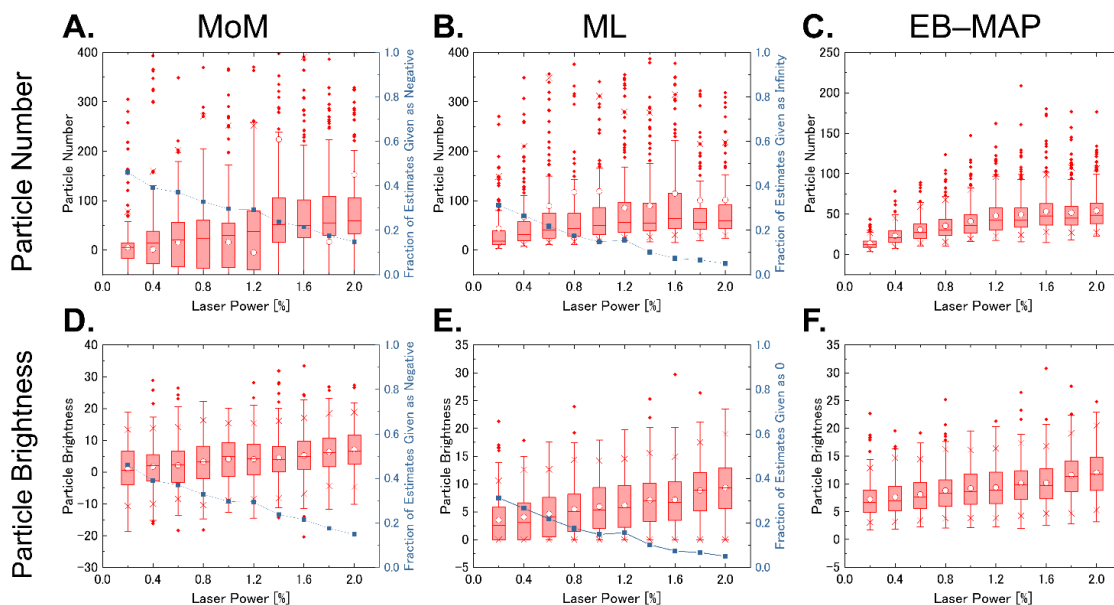


FIGURE S5.1: Variation in estimates for different laser powers

Two thousand images were obtained with different laser powers, and analyzed by MoM (A, D), ML (B, E), and EB-MAP (C, F). (A, B, C) Dependence of the estimated particle number on laser power. Figure S5.1A and S5.1B are shown in enlarged view (see Fig. S5.2 for broad view). (D, E, F) Dependence of the estimated particle brightness [kHz] on laser power. All figures are shown similarly in Fig. 2.

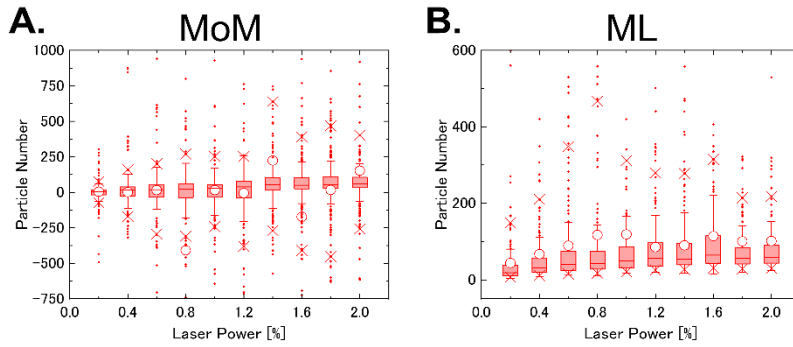


FIGURE S5.2: Broad view of estimated particle number in Fig. S5.1A and S5.1B

The view is adjusted to show the 5th and 95th percentiles of the particle number. The minimum and maximum values are listed in Table S5.1 and S5.2. (A) Broad view of Fig. S5.1A. (B) Broad view of Fig. S5.1B.

Laser Power [%]	Minimum	Maximum
0.2	-4.907×10^2	1.452×10^3
0.4	-2.592×10^3	2.023×10^3
0.6	-3.197×10^3	2.639×10^3
0.8	-1.090×10^5	1.831×10^3
1.0	-3.583×10^3	4.386×10^3
1.2	-6.125×10^3	4.618×10^3
1.4	-4.432×10^3	2.019×10^4
1.6	-4.189×10^4	5.072×10^3
1.8	-4.242×10^3	1.320×10^3
2.0	-1.317×10^4	3.506×10^4

TABLE S5.1: Minimum and maximum values of the estimated particle number in Fig. S5.1A

Laser Power [%]	Minimum	Maximum
0.2	3.666	6.474×10^2
0.4	8.691	1.153×10^3
0.6	1.180×10	1.303×10^3
0.8	1.082×10	2.768×10^3
1.0	1.749×10	3.255×10^3
1.2	1.884×10	5.013×10^2
1.4	1.657×10	9.492×10^2
1.6	1.538×10	2.017×10^3
1.8	1.920×10	2.701×10^3
2.0	2.423×10	3.165×10^3

TABLE S5.2: Minimum and maximum values of the estimated particle number in Fig. S5.1B

	Slope	Intercept
MoM	3.25 ± 0.17	0.37 ± 0.22
ML	3.11 ± 0.17	2.80 ± 0.19
EB-MAP	2.55 ± 0.14	6.62 ± 0.17

TABLE S5.3: Slope and intercept for the fitted line in Fig. 5B

Estimated value and standard error

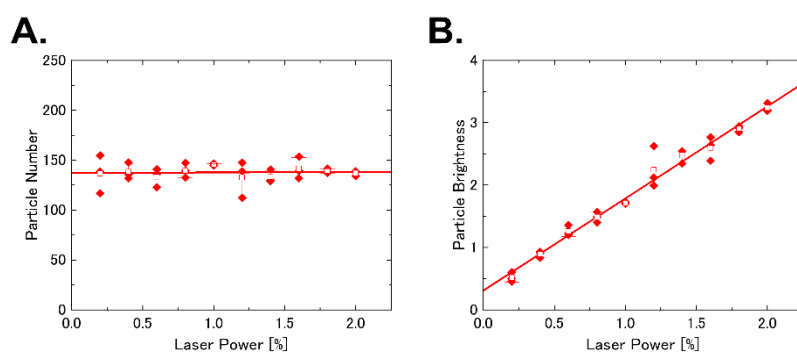


FIGURE S5.3: FCS measurements on EGFP solution with different laser powers

(A) Dependence of the estimated particle number on laser power. (B) Dependence of the estimated particle brightness [kHz] on laser power. In the plot, diamonds: results obtained from a single measurement, open squares: averages, and error bars: standard deviations. The solid lines are fitted lines obtained by the least squares method (see Table S5.4 for details on parameters of the lines).

	Slope	Intercept
Particle Number	0.6 ± 3.1	137.2 ± 3.8
Particle Brightness	1.477 ± 0.046	0.310 ± 0.057

TABLE S5.4: Slope and intercept for the fitted line in Fig. S5.3A and S5.3B

Estimated value and standard error

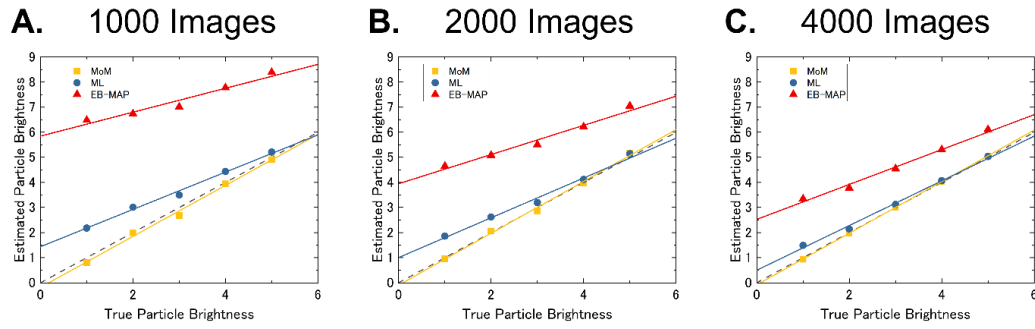


FIGURE S5.4: Simulations with different numbers of images

1000 (A), 2000 (B), and 3000 images (C) of size 34×34 were simulated with a fixed particle number of 10 and different particle brightness. (A, B, C) Dependence of the estimated particle brightness on true particle brightness. The symbols show the average of particle brightness. The dashed lines represent the true value. The solid lines are fitted lines obtained by the weighted least squares method (see Table S5.5 for details on parameters of the lines).

		Slope	Intercept
S5.4A	MoM	1.016 ± 0.043	-0.18 ± 0.14
	ML	0.744 ± 0.036	1.44 ± 0.11
	EB-MAP	0.477 ± 0.065	5.85 ± 0.21
S5.4B	MoM	1.034 ± 0.038	-0.09 ± 0.13
	ML	0.793 ± 0.048	1.00 ± 0.14
	EB-MAP	0.582 ± 0.056	3.95 ± 0.17
S5.4C	MoM	1.0292 ± 0.0048	-0.084 ± 0.016
	ML	0.891 ± 0.038	0.50 ± 0.11
	EB-MAP	0.696 ± 0.044	2.53 ± 0.13

TABLE S5.5: Slope and intercept for the fitted line in Fig. S5.4

Estimated value and standard error

Supplemental data for Fig. 6

Fig. S6.1 and S6.2 show the particle number and particle brightness in the experiments with EGFP tandem-oligomer in a living cell. The fluorescence intensity in the nucleus is lower than that in the cytoplasm for the EGFP dimer and trimer. This could have been caused by the higher molecular weight of the EGFP dimer and trimer than the monomer. The higher molecular weight species would be difficult to pass through nuclear pores. At the boundary between the nucleus and cytoplasm, the estimation of the particle number was markedly lower, and that of particle brightness was markedly higher than those in the nucleus and cytoplasm; this is remarkable in the EGFP trimer (Fig. S6.2D and S6.2F). This occurs due to the non-stationary change in fluorescence intensity by the movement of the nuclear membrane within the field of imaging. In actuality, the total measurement time is approximately 8 min to obtain 2000 images, and the cells migrate during the entire time period. We have previously reported that non-stationary changes cause artifacts, underestimation of particle number, and overestimation of particle brightness (6). Thus, we carefully placed the ROIs by avoiding the areas on which the pixel values would be biased by the artifact. Performing corrections for the non-stationary changes would improve the estimations.

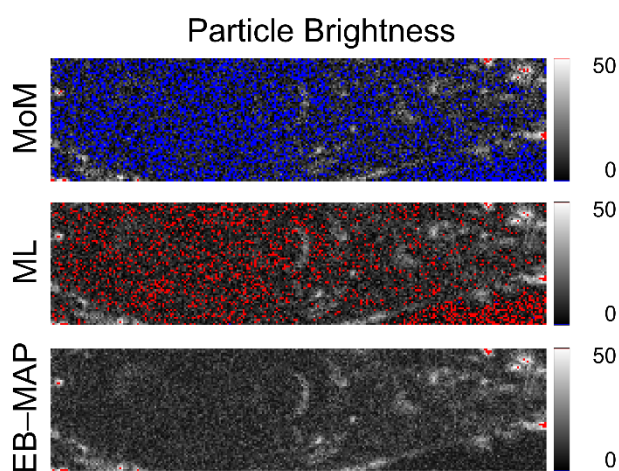


FIGURE S6.1: Particle brightness images of EGFP monomer

Estimated images of particle brightness [kHz]. Fluorescence intensity and particle number are shown in Fig. 6. The pixels below the range are colored in blue, and those beyond the range are colored in red. (Please view the digital version of this figure because the printed version could appear different.)

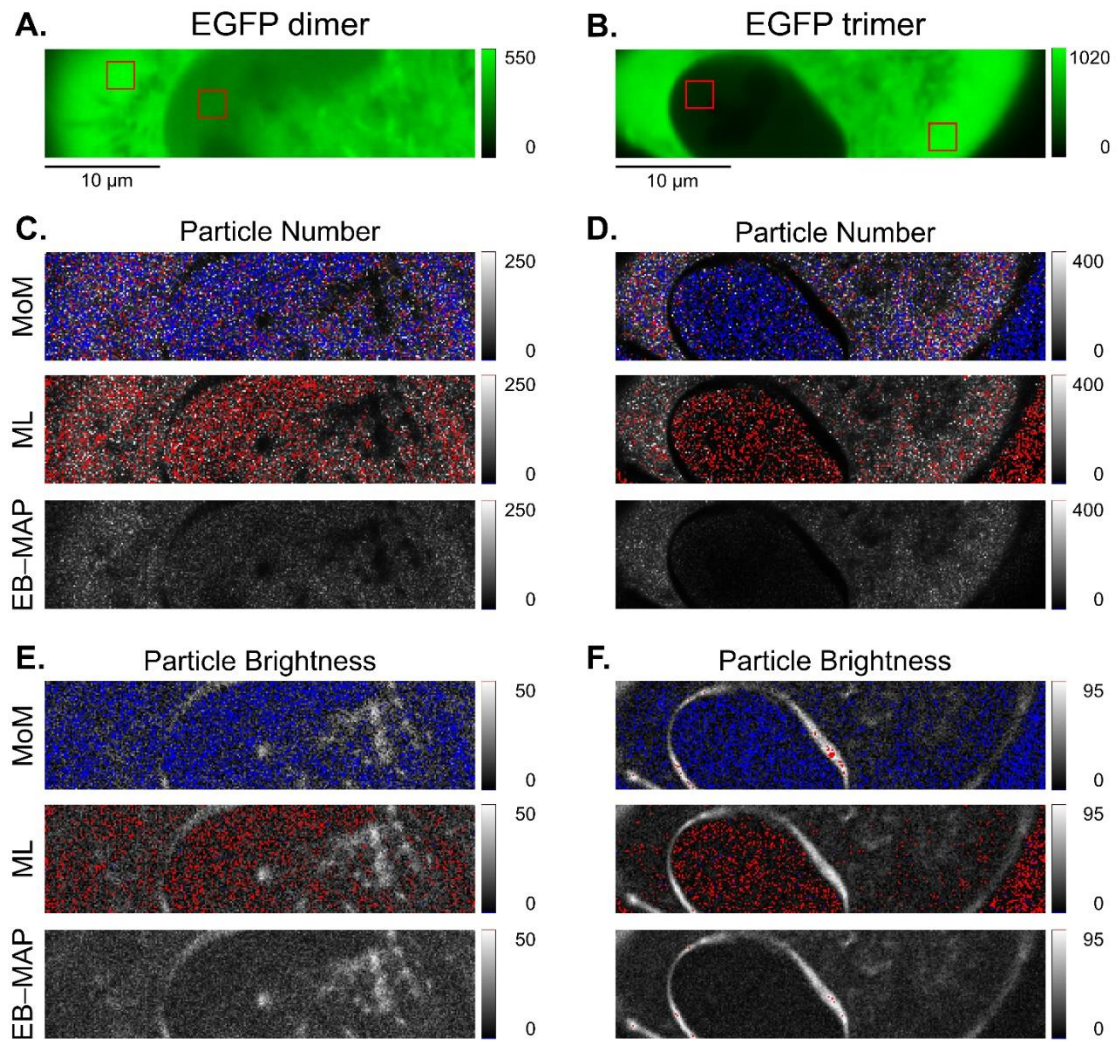


FIGURE S6.2: Estimated images for EGFP dimer and trimer

Experiments on EGFP dimer and trimer. Images of fluorescence intensity [kHz] for EGFP dimer (A) and trimer (B). Red squares represent the ROIs placed in the nucleus and cytoplasm. Estimated images of particle number for dimer (C) and trimer (D), and that of particle brightness [kHz] for dimer (E) and trimer (F). The pixels below the range are colored in blue, and those beyond the range are colored in red. (Please view the digital version of this figure because the printed version could appear different.)

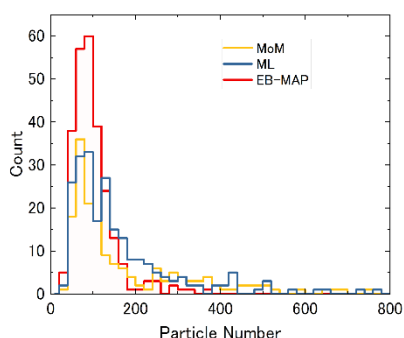


FIGURE S6.3: Histogram of particle number

The histogram was created from the particle number for EGFP monomer in the cytoplasm (ROI is shown in Fig. 6A).

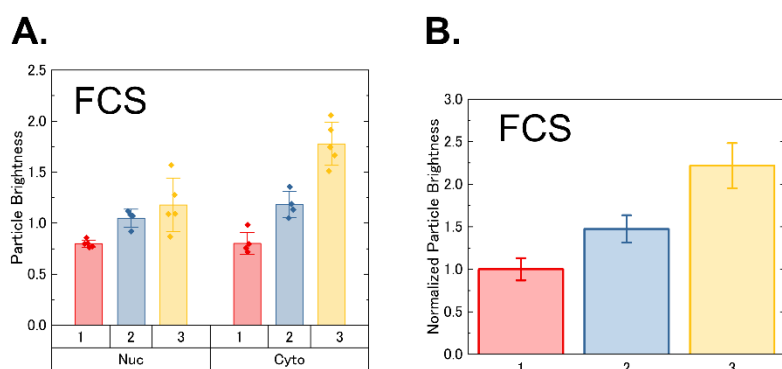


FIGURE S6.4: FCS measurements on EGFP tandem oligomers

(A) Dependence of the particle brightness [kHz] on the number of EGFP units in the nucleus (Nuc) and cytoplasm (Cyto). Dots: particle brightness, bar: sample average of particle brightness, and error bar: sample standard deviation of particle brightness. (B) Normalized particle brightness with respect to the particle brightness of the monomer in the cytoplasm. Bar: fold change in particle brightness (sample average of normalized particle brightness), error bar: sample standard deviation of normalized particle brightness.

Supplemental data for Fig. 6C–E and Fig. S6.4A**Verification of linearity in particle brightness of EGFP tandem oligomers**

In experiments with EGFP tandem oligomers, particle brightness is expected to proportionally increase (with intercept of 0) for the monomer, dimer, and trimer. Even if a non-fluorescent state of EGFP appears, the particle brightness linearly increases (with intercept of any value). In Fig. S6.4A, the average particle brightness seems to increase linearly in the cytoplasm for FCS. However, in Fig. 6C–E, the average of the average particle brightnesses does not seem to increase linearly in the cytoplasm for MoM, ML, and EB–MAP. One could consider that particle brightness of the trimer is positively biased.

We assume that the particle brightness for the monomer and dimer was estimated accurately, but that for the trimer was overestimated. To evaluate the uncertainty, we estimated credible intervals for the difference between actual and predicted particle brightness of trimer. The particle brightness is predicted by assuming linearity between particle brightness of the monomer and dimer. The aim of this evaluation is not to specify the cause resulting in the non-linear change of particle brightness in our experiments, but to provide a method to evaluate the uncertainty of results in readers' experiments. In a strict sense, we cannot specify the cause that resulted in the non-linear change of particle brightness because our experiment is conducted on three different oligomeric states. Other combinations of assumptions are possible: The particle brightness for the dimer and trimer were estimated accurately, but the particle brightness for the monomer was overestimated; the particle brightness for the monomer and trimer were estimated accurately, but the particle brightness for the dimer was underestimated. Naturally, the linearity of the particle brightness between the monomer, dimer, and trimer is lost if two of the three particle brightness are not estimated accurately. The following analyses do not determine whether a scientific assumption is true. In the interpretation of the following results, we referred to papers (12, 13).

Statistical Model

First, we predict the particle brightness of the trimer by assuming linearity between the particle brightness of the monomer and dimer. Let X be the EGFP subunit number for the monomer, dimer, and trimer ($X = 1, 2, 3$) and Y be the particle brightness. Note that variables used in this section are different from those used in the main text. We assume that particle brightness plotted as dots in Figs. S6.4A and 6C–E follow an independent normal distribution with average μ and standard deviation σ , and we assume that the average of the normal distribution is equal to $aX + b$ for the monomer and dimer, where a and b are the regression coefficient and intercept, respectively. In addition, we assume that the prior distribution of a and b follow a normal distribution, and the prior distribution of σ follows a half-Cauchy distribution. The joint probability distribution is given by

$$P(\mathbf{Y}_m, \sigma_m, \mathbf{Y}_d, \sigma_d, a, b) = P(\mathbf{Y}_m | a, b, \sigma_m) P(\mathbf{Y}_d | a, b, \sigma_d) P(a, b, \sigma_m, \sigma_d), \quad (\text{S28})$$

where

$$P(\mathbf{Y}_m | a, b, \sigma_m) = \prod_{i=1}^{I_m} \text{Nor}(Y_m^{(i)} | a + b, \sigma_m), \quad (\text{S29})$$

$$P(\mathbf{Y}_d | a, b, \sigma_d) = \prod_{i=1}^{I_d} \text{Nor}(Y_d^{(i)} | 2a + b, \sigma_d), \quad (\text{S30})$$

$$P(a, b, \sigma_m, \sigma_d) = \text{Nor}(a | \mu_1, \sigma_1) \text{Nor}(b | \mu_2, \sigma_2) \text{Cau}(\sigma_m | \varphi_1, \psi_1) \text{Cau}(\sigma_d | \varphi_2, \psi_2). \quad (\text{S31})$$

The subscripts m and d represent variables for the monomer and dimer, respectively. The superscript (i) represents the ordinal number of observations. For I_m times observation, $\mathbf{Y}_m = (Y_m^{(1)}, Y_m^{(2)}, \dots, Y_m^{(I_m)})$. Nor and Cau are normal and half-Cauchy distribution, respectively:

$$\text{Nor}(Y | \mu, \sigma) = \frac{1}{\sqrt{2\pi\sigma^2}} \exp\left(-\frac{(Y - \mu)^2}{2\sigma^2}\right), \quad (\text{S32})$$

$$\text{Cau}(\sigma | \varphi, \psi) = \frac{2}{\pi\psi} \left[\frac{\psi^2}{\psi^2 + (\sigma - \varphi)^2} \right]. \quad (\text{S33})$$

The hyperparameters are fixed as follows: $\mu_1 = \mu_2 = 0$, $\sigma_1 = \sigma_2 = 10^3$, $\varphi_1 = \varphi_2 = 0$, and $\psi_1 = \psi_2 = 25$. We believe that prior distributions with the hyperparameters would not be informative. In experiments with EGFP in the cells, the plausible values of particle brightness are in the range from 0 to 20 kHz, and a particle brightness of 40 kHz has a less likely yield than 20 kHz. For the hyperparameters, the prior distributions for $a + b$ and $2a + b$ are given by $\text{Nor}(a + b | 0, \sqrt{2} \times 10^3)$ and $\text{Nor}(2a + b | 0, \sqrt{5} \times 10^3)$, respectively. $\text{Nor}(a + b | 0, \sqrt{2} \times 10^3)$ is flat in the range from 0 to 100 kHz, while the probability density is 2.82×10^{-4} at $a + b = 0$ and 2.81×10^{-4} at $a + b = 100$. $\text{Nor}(2a + b | 0, \sqrt{5} \times 10^3)$ is flat in the range from 0 to 100 kHz. A plausible value of the standard deviation for particle brightness is less than 10 kHz. Particle brightness is a universal parameter under the same experimental conditions, where the change of particle brightness in different cells is small. $\text{Cau}(\sigma_m | 0, 25)$ and $\text{Cau}(\sigma_d | 0, 25)$ are weakly-informative (14–16). The posterior distribution of predicted particle brightness for the trimer is $\mu_t^{\text{pred}} = 3a + b$ by the posterior

distribution for a and b , where the subscript t represents variables for the trimer. Next, we estimate the average particle brightness of the trimer. We assume that the prior distribution of μ_t and σ_t follow normal and half-Cauchy distributions, respectively. The joint probability distribution is given as follows, with $\mathbf{Y}_t = (Y_t^{(1)}, Y_t^{(2)}, \dots, Y_t^{(I_t)})$:

$$P(\mathbf{Y}_t, \mu_t, \sigma_t) = \prod_{i=1}^{I_t} \left[\text{Nor}(Y_t^{(i)} | \mu_t, \sigma_t) \right] \text{Nor}(\mu_t | \mu_3, \sigma_3) \text{Cau}(\sigma_t | \varphi_3, \psi_3). \quad (\text{S34})$$

The hyperparameters are fixed similarly as follows: $\mu_3 = 0$, $\sigma_3 = 10^3$, $\varphi_3 = 0$, and $\psi_3 = 25$. $\text{Nor}(\mu_t | 0, 10^3)$ is flat in the range from 0 to 100 kHz; the probability density is 3.99×10^{-4} at $\mu_t = 0$ and 3.97×10^{-4} at $\mu_t = 100$. The difference between the actual and predicted particle brightness of the trimer is given by the posterior distribution of μ_t and μ_t^{pred} as follows:

$$\delta_\mu = \mu_t - \mu_t^{\text{pred}}. \quad (\text{S35})$$

Results

We evaluated the difference between the actual and predicted particle brightness of the trimer, δ_μ , using different methods: FCS, MoM, ML, and EB-MAP. We used Markov chain Monte Carlo (MCMC) to simulate random numbers drawn from the posterior distribution of δ_μ . The random numbers are a better approximation of the posterior distribution at the convergence to stationary distribution. We assessed the convergence using $\hat{n}_{\text{eff}}/(mn)$ and \hat{R} (17), where \hat{n}_{eff} is the effective number of the simulated draws, m is the number of multiple simulated sequence, n is the actual number of the simulated draws in each simulated sequence, and \hat{R} is the potential scale reduction factor. Fig. S7.1 shows the posterior distribution of δ_μ , and Table S7.1 shows the posterior mean and percentiles, assessment factors for convergence, and the probability for differences less and greater than 0. In Table S7.1, $\hat{n}_{\text{eff}}/(mn)$ for all methods ranged from 0.86 to 0.99, indicating minimal autocorrelation between the simulated draws, and \hat{R} for all methods ranged from 0.9999 to 1.0000, indicating the convergence of the simulated draws. In Fig. S7.1 and Table S7.1, FCS results suggest that the actual particle brightness of the trimer is 0.22 kHz higher than the predicted particle brightness on average. On the contrary, the 95% credible interval suggests that the difference in the particle brightness ranging from -0.58 to 1.02 kHz is compatible with our data, given our assumptions. From the credible interval, we infer the following: The difference of -0.58 indicates that the actual particle brightness of the trimer is 0.58 kHz lower than the predicted line, the difference of 0 indicates that the

actual particle brightness of the trimer is on the predicted line, and the difference of 1.02 indicates that the actual particle brightness of the trimer is 1.02 kHz higher than the predicted line. In Table S7.1, the posterior probability for δ_μ less and greater than 0 are 0.22 and 0.78, respectively, indicating that the probability for δ_μ greater than 0 is high compared with the probability for less than 0. In Fig. S7.1 and Table S7.1, MoM, ML, and EB-MAP showed a wider range of 95% credible interval, and the posterior mean was higher than FCS. The posterior probability for $\delta_\mu > 0$ increased to 0.95, 0.92, and 0.92 for MoM, ML, and EB-MAP, respectively. To show how suitable our statistical model for characterizing observed samples are, we calculated the posterior predictive p-value (17) (Chapter 6, Model checking, p. 141), using sample mean and standard deviation as test quantities. In Table S7.2, the posterior predictive p-value of the sample average for all methods ranged from 0.49 to 0.50, indicating the sample averages are similar for replicated and observed samples. In Table S7.3, the posterior predictive p-value of sample standard deviations ranged from 0.61 to 0.64, indicating the sample standard deviations of replicated samples are occasionally higher than that of the observed samples.

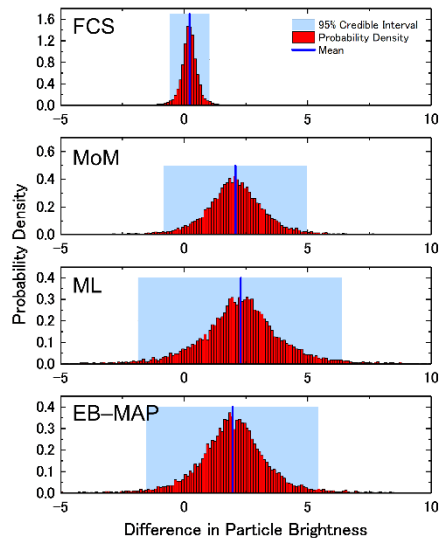


FIGURE S7.1: Uncertainty in linearity of particle brightness for EGFP trimer

Posterior distribution for the difference between actual and predicted particle brightness [kHz] of the trimer in the cytoplasm. The light blue shaded area represents 95% credible interval (interval between 2.5th and 97.5th percentiles), red histogram the posterior probability density, and solid blue line the posterior mean.

	Posterior Mean and Percentiles				Convergence Assessment		Posterior Probability	
	Mean and SE	Median	$Q_{2.5}$	$Q_{97.5}$	$\hat{n}_{\text{eff}}/(mn)$	\hat{R}	$P(\delta_{\mu} < 0)$	$P(\delta_{\mu} > 0)$
FCS	0.2181 ± 0.0024	0.2177	-0.5772	1.0243	0.8646	0.9999	0.217	0.783
MoM	2.0824 ± 0.0076	2.0780	-0.8228	4.9718	0.9027	1.0000	0.054	0.946
ML	2.2971 ± 0.0108	2.3213	-1.8680	6.3851	0.9880	0.9999	0.082	0.918
EB-MAP	1.9731 ± 0.0089	1.9744	-1.5325	5.4337	0.9798	1.0000	0.080	0.920

TABLE S7.1: Summary of posterior distribution in Fig. S7.1

		Test Quantity	Convergence Assessment	
		Sample Mean	$\hat{n}_{\text{eff}}/(mn)$	\hat{R}
FCS	Y_m	0.5026 ± 0.0022	1.0143	0.9999
	Y_d	0.4983 ± 0.0022	0.9997	1.0000
	Y_t	0.4995 ± 0.0023	0.9420	1.0000
MoM	Y_m	0.5000 ± 0.0022	1.0061	1.0000
	Y_d	0.4942 ± 0.0022	0.9928	1.0000
	Y_t	0.4976 ± 0.0022	0.9882	1.0000
ML	Y_m	0.5000 ± 0.0022	1.0048	1.0000
	Y_d	0.5012 ± 0.0023	0.9739	1.0000
	Y_t	0.5012 ± 0.0022	0.9934	1.0001
EB-MAP	Y_m	0.4980 ± 0.0023	0.9850	1.0001
	Y_d	0.4993 ± 0.0022	1.0092	1.0000
	Y_t	0.4995 ± 0.0022	0.9880	1.0000

TABLE S7.2: Summary of posterior predictive p-values estimated by sample mean for Fig. S7.1

		Test Quantity	Convergence Assessment	
		Sample Standard Deviation	$\hat{n}_{\text{eff}}/(mn)$	\hat{R}
FCS	Y_m	0.6138 ± 0.0022	1.0042	1.0000
	Y_d	0.6448 ± 0.0022	0.9885	0.9999
	Y_t	0.6194 ± 0.0022	1.0150	1.0000
MoM	Y_m	0.6168 ± 0.0022	0.9987	1.0000
	Y_d	0.6443 ± 0.0021	1.0058	1.0000
	Y_t	0.6157 ± 0.0022	0.9705	1.0000
ML	Y_m	0.6214 ± 0.0022	0.9789	1.0000
	Y_d	0.6437 ± 0.0021	0.9996	1.0000
	Y_t	0.6194 ± 0.0022	0.9614	1.0001
EB-MAP	Y_m	0.6131 ± 0.0022	1.0072	1.0001
	Y_d	0.6443 ± 0.0022	0.9556	0.9999
	Y_t	0.6160 ± 0.0022	0.9891	1.0000

TABLE S7.3: Summary of posterior predictive p-values estimated by sample standard deviation for Fig. S7.1

Discussions and Comments

We predicted the particle brightness of the EGFP trimer by assuming a linearity between the particle brightness of the monomer and dimer. The 95% credible intervals in Fig. S7.1 indicate a wide range of uncertainty; thus, we cannot make strong implications, such as whether the actual particle brightness of the trimer is higher than the predicted line or whether the actual particle brightness is on the predicted line, for all methods. We need to increase the sample sizes to distinguish whether the actual particle brightness is on the predicted line. The 95% credible interval in FCS has an important sense practically; the difference of -0.58 and 1.02 kHz between the actual and predicted particle brightness is not negligible, compared with the sample average of 1.78 kHz for the particle brightness of the trimer (Fig. S6.4A). The uncertainty of the difference between the particle brightnesses are also not negligible for MoM, ML, and EB-MAP. According to statistical hypothesis testing with a significance level of 0.05 , if the 95% credible interval does not contain a difference of 0 between the actual and predicted particle brightness, it is possible to mechanically make the decision that the actual and predicted particle brightness is significantly different. Note that we obtained these results using small sample sizes and our assumptions, and we should not place too much confidence on the exact numerical values of these results. This is because our statistical model is not perfectly true. Although we constructed our statistical model using normal and half-Cauchy distributions, we have no evidence that the model is true. However, we can show the suitability of our statistical model for characterizing observed samples through the posterior predictive p-value. If the statistical model is suitable to characterize the observed samples, replicated samples produced by posterior predictive distribution and observed samples would be similar. The results in Table S7.2 suggest that our statistical model is suitable to estimate the mean, but the results in Table S7.3 suggest that our statistical model tends to overestimate the standard deviation. However, we believe that the use of our statistical model for the observed samples do not cause serious problems. The posterior predictive p-value of approximately 0.6 indicates overestimated standard deviation in 60% of replicated samples among the multiple sets of replicated samples. We believe that the deviation between 0.5 and 0.6 is not significantly large.

Methods

Markov chain Monte Carlo (MCMC)

Posterior draws were simulated using R, version 4.0.3 (18), and Stan, version 2.21.2 (19). Five sequences of draws are simulated in parallel to assess convergence of the simulated draws. The total number of simulated draws for each sequence is $305,000$. The first $5,000$ draws were discarded, and the remainder of the sequence was thinned by keeping every 30th draw, resulting in $10,000$ draws for each sequence.

Supplemental data for Fig. 6F and Fig. S6.4B**Credible interval of fold change in particle brightness**

In experiments with EGFP tandem oligomers, Fig. 6F shows the normalized particle brightness, where the average of normalized particle brightness is the fold change. We estimated the credible interval of the fold change for FCS, MoM, ML, and EB-MAP. The credible interval is useful to compare results obtained by different methods and verify the compatibility of the results. Using the same notation from the previous section, we assume that the joint probability distributions are given by

$$P(\mathbf{Y}_m, \mu_m, \sigma_m) = \prod_{i=1}^{I_m} \left[\text{Nor}(Y_m^{(i)} | \mu_m, \sigma_m) \right] \text{Nor}(\mu_m | \mu_4, \sigma_4) \text{Cau}(\sigma_m | \varphi_4, \psi_4), \quad (\text{S36})$$

$$P(\mathbf{Y}_d, \mu_d, \sigma_d) = \prod_{i=1}^{I_d} \left[\text{Nor}(Y_d^{(i)} | \mu_d, \sigma_d) \right] \text{Nor}(\mu_d | \mu_5, \sigma_5) \text{Cau}(\sigma_d | \varphi_5, \psi_5), \quad (\text{S37})$$

$$P(\mathbf{Y}_t, \mu_t, \sigma_t) = \prod_{i=1}^{I_t} \left[\text{Nor}(Y_t^{(i)} | \mu_t, \sigma_t) \right] \text{Nor}(\mu_t | \mu_6, \sigma_6) \text{Cau}(\sigma_t | \varphi_6, \psi_6). \quad (\text{S38})$$

We fixed the hyperparameters as follows: $\mu_4 = \mu_5 = \mu_6 = 0$, $\sigma_4 = \sigma_5 = \sigma_6 = 10^3$, $\varphi_4 = \varphi_5 = \varphi_6 = 0$, and $\psi_4 = \psi_5 = \psi_6 = 25$. The fold changes in the particle brightness for the EGFP dimer and trimer are given as follows using the posterior distributions of μ_m , μ_d , and μ_t :

$$r_d = \frac{\mu_d}{\mu_m}, \quad (\text{S39})$$

$$r_t = \frac{\mu_t}{\mu_m}. \quad (\text{S40})$$

Results

Fig. S8.1 shows the posterior distributions of r_d and r_t for FCS, MoM, ML (+), and EB-MAP (+). We used MCMC to simulate the draws from the posterior distribution in the same way as the previous section. Table S8.1 summarizes the posterior mean, posterior percentiles, and the assessment factors for convergence. $\hat{n}_{\text{eff}}/(mn)$ for all methods ranged from 0.94 to 1.00, indicating minimal autocorrelation between the simulated draws, and \hat{R} for all methods ranged from 1.0000 to 1.0001, indicating the convergence of the simulated draws. In Fig. S8.1 and Table S8.1, FCS result

for the dimer shows that the 95% credible interval ranged from 0.98—indicating that the particle brightness of the dimer is equal to that of the monomer—to 2.12—indicating that the particle brightness of the dimer is approximately two times higher than that of the monomer. The 95% credible intervals of the fold change for the dimer in each method are within the range of 0.6 to 2.2 and overlapped each other, indicating that the results are compatible with each other. Similarly, the 95% credible intervals of the fold change for the trimer are compatible with each other. Tables S8.2 and S8.3 summarize the posterior predictive p-value calculated by the sample mean and standard deviation, respectively. In Table S8.2, the posterior predictive p-value of the sample averages for all methods ranged from 0.49 to 0.50, indicating that they were similar between replicated and observed samples. In Table S8.3, the posterior predictive p-value of sample standard deviations ranged from 0.62 to 0.65, indicating the sample standard deviations of the replicated samples are occasionally higher than that of the observed samples.

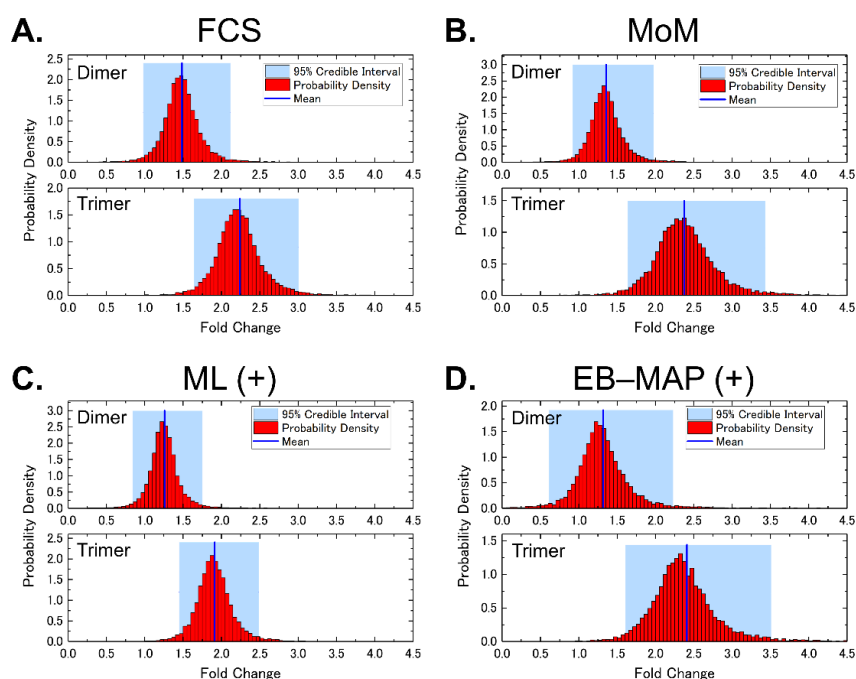


FIGURE S8.1: Uncertainty in fold change of particle brightness for EGFP dimer and trimer with respect to monomer

Posterior distribution for fold change in particle brightness in cytoplasm. The light blue shaded area represents 95% credible interval: interval between 2.5th and 97.5th percentiles, red histogram: posterior probability density, and blue solid line: posterior mean.

Discussions and Comments

In Fig. S8.1, the 95% credible intervals for FCS, MoM, ML (+), and EB–MAP (+) showed a wide range of uncertainty that was non-negligible. In Fig. 6F, particle brightness is divided by the sample average of particle brightness for monomer, which is the normalized particle brightness, and thus, the uncertainty in the population average of the particle brightness for the monomer is neglected. The credible interval is more useful than the standard deviation of the normalized particle brightness to estimate uncertainty. However, while useful to translate the uncertainty into numerical values, credible intervals must be interpreted with care. This is because the statistical model is not true, similar to the previous section. Tables S8.2 and S8.3 summarize the similarity between the observed and replicated samples. The statistical model introduced in this section is not the only model to estimate uncertainty, and other models can be used.

	Tandem Oligomer	Posterior Mean and Percentiles				Convergence Assessment	
		Mean and SE	Median	$Q_{2.5}$	$Q_{97.5}$	$\hat{n}_{\text{eff}}/(mn)$	\hat{R}
FCS	Dimer	1.4854 ± 0.0033	1.4728	0.9779	2.1153	0.9421	1.0000
	Trimer	2.2404 ± 0.0045	2.2164	1.6432	3.0051	0.9997	1.0000
MoM	Dimer	1.3544 ± 0.0118	1.3431	0.9200	1.9735	1.0005	1.0001
	Trimer	2.3773 ± 0.0200	2.3538	1.6383	3.4320	0.9979	1.0000
ML (+)	Dimer	1.2584 ± 0.0025	1.2497	0.8410	1.7530	0.9903	1.0001
	Trimer	1.9120 ± 0.0033	1.8971	1.4467	2.4853	0.9960	1.0000
EB–MAP (+)	Dimer	1.3184 ± 0.0106	1.2832	0.6109	2.2314	0.9934	1.0000
	Trimer	2.4101 ± 0.0277	2.3326	1.6109	3.5076	0.9989	1.0000

TABLE S8.1: Summary of posterior distribution in Fig. S8.1

		Test Quantity	Convergence Assessment	
		Sample Mean	$\hat{n}_{\text{eff}}/(mn)$	\hat{R}
FCS	Y_m	0.5027 ± 0.0022	0.9924	1.0000
	Y_d	0.4972 ± 0.0022	0.9907	1.0001
	Y_t	0.4974 ± 0.0022	0.9951	1.0000
MoM	Y_m	0.4971 ± 0.0022	0.9939	1.0000
	Y_d	0.5042 ± 0.0022	1.0091	1.0000
	Y_t	0.4992 ± 0.0022	1.0161	1.0000
ML (+)	Y_m	0.5001 ± 0.0022	0.9926	1.0000
	Y_d	0.4975 ± 0.0023	0.9812	1.0000
	Y_t	0.5018 ± 0.0023	0.9832	1.0000
EB-MAP (+)	Y_m	0.4993 ± 0.0022	0.9947	1.0001
	Y_d	0.5006 ± 0.0022	1.0016	0.9999
	Y_t	0.5027 ± 0.0022	1.0197	1.0000

TABLE S8.2: Summary of posterior predictive p-values estimated by sample mean for Fig. S8.1

		Test Quantity	Convergence Assessment	
		Sample Standard Deviation	$\hat{n}_{\text{eff}}/(mn)$	\hat{R}
FCS	Y_m	0.6183 ± 0.0022	0.9908	1.0000
	Y_d	0.6471 ± 0.0021	0.9903	0.9999
	Y_t	0.6194 ± 0.0022	0.9863	1.0000
MoM	Y_m	0.6185 ± 0.0022	0.9683	0.9999
	Y_d	0.6451 ± 0.0022	0.9947	1.0000
	Y_t	0.6181 ± 0.0022	0.9723	0.9999
ML (+)	Y_m	0.6224 ± 0.0022	1.0032	0.9999
	Y_d	0.6481 ± 0.0021	0.9873	1.0000
	Y_t	0.6160 ± 0.0022	0.9907	1.0000
EB-MAP (+)	Y_m	0.6219 ± 0.0022	0.9770	1.0000
	Y_d	0.6480 ± 0.0021	1.0018	1.0000
	Y_t	0.6178 ± 0.0022	0.9986	1.0000

TABLE S8.3: Summary of posterior predictive p-values estimated by sample standard deviation for Fig. S8.1

SUPPORTING REFERENCES

1. Bédard, G. 1967. Dead-time corrections to the statistical distribution of photoelectrons. *Proc. Phys. Soc.* 90.
2. Ackermann, J., and H. Hogueve. 2010. Small dead-time expansion in counting distributions and moments. *Nucl. Instruments Methods Phys. Res. Sect. A Accel. Spectrometers, Detect. Assoc. Equip.* 614:297–302.
3. Hillesheim, L.N., and J.D. Müller. 2003. The Photon Counting Histogram in Fluorescence Fluctuation Spectroscopy with Non-Ideal Photodetectors. *Biophys. J.* 85:1948–1958.
4. Hillesheim, L.N., and J.D. Müller. 2005. The dual-color photon counting histogram with non-ideal photodetectors. *Biophys. J.* 89:3491–3507.
5. Bishop, C.M. 2006. *Pattern Recognition and Machine Learning*. Springer, Germany.
6. Fukushima, R., J. Yamamoto, H. Ishikawa, and M. Kinjo. 2018. Two-detector number and brightness analysis reveals spatio-temporal oligomerization of proteins in living cells. *Methods.* 140–141:161–171.
7. Oura, M., J. Yamamoto, H. Ishikawa, S. Mikuni, R. Fukushima, and M. Kinjo. 2016. Polarization-dependent fluorescence correlation spectroscopy for studying structural properties of proteins in living cell. *Sci. Rep.* 6:31091.
8. Pack, C., K. Saito, M. Tamura, and M. Kinjo. 2006. Microenvironment and Effect of Energy Depletion in the Nucleus Analyzed by Mobility of Multiple Oligomeric EGFPs. *Biophys. J.* 91:3921–3936.
9. Takahasi, H., and M. Mori. 1973. Double exponential formulas for numerical integration. *Publ. Res. Inst. Math. Sci.* 9:721–741.
10. Müller, C.B., A. Loman, V. Pacheco, F. Koberling, D. Willbold, W. Richtering, and J. Enderlein. 2008. Precise measurement of diffusion by multi-color dual-focus fluorescence correlation spectroscopy. *Europhys. Lett.* 83:46001.
11. Culbertson, C.T., S.C. Jacobson, and J. Michael Ramsey. 2002. Diffusion coefficient measurements in microfluidic devices. *Talanta.* 56:365–73.
12. Amrhein, V., S. Greenland, and B. McShane. 2019. Scientists rise up against statistical significance. *Nature.* 567:305–307.
13. Johnson, D.H. 1999. The Insignificance of Statistical Significance Testing. *J. Wildl. Manage.* 63:763.
14. Lemoine, N.P. 2019. Moving beyond noninformative priors: why and how to choose weakly informative priors in Bayesian analyses. *Oikos.* 128:912–928.
15. Gelman, A. 2006. Prior distributions for variance parameters in hierarchical models (comment on article by Browne and Draper). *Bayesian Anal.* 1:515–534.
16. Polson, N.G., and J.G. Scott. 2012. On the Half-Cauchy Prior for a Global Scale Parameter.

- Bayesian Anal.* 7:887–902.
17. Gelman, A., J. Carlin, H. Stern, and D. Rubin. 2004. Bayesian data analysis. 3rd ed. Chapman & Hall/CRC, UK.
 18. R Core Team. 2020. R: A language and environment for statistical computing. R Foundation for Statistical Computing, Vienna, Austria. <https://www.r-project.org/>.
 19. Stan Development Team. 2020. RStan: the R interface to Stan. <http://mc-stan.org/>.

Chapter 6

Conclusions and Future Perspectives

I developed TD-, ML-, and EB-MAP-N&B analyses to accurately and precisely estimate the particle number and particle brightness, which reflect the concentration and oligomeric state, respectively, of fluorescently labeled proteins in cells. TD-N&B analysis is less affected by the dead time effect compared with the conventional method and produces a more accurate estimation. ML- and EB-MAP-N&B analyses provide more accurate and precise estimation than does TD-N&B analysis. In EB-MAP-N&B analysis, the statistical model effectively uses spatial information based on Bayesian statistics. We demonstrated that the developed methods are feasible and achieve higher accuracy and precision than the conventional method. Our methods have a wide range of applications in the field of fluorescence live cell imaging. Furthermore, these methods would contribute to the understanding of dynamic processes in protein oligomerization in cells.

To the best of our knowledge, this is the first study that applies Bayesian statistics to N&B analysis, and we have demonstrated the great potential of Bayesian statistics. The methods reported in this study create avenues for further research in this field. In this study, although we mainly focused on the pair of parameters that maximizes the joint posterior distribution, other estimators can be used. The MAP estimate can be determined by maximizing the marginal distribution of the joint posterior distribution. Additionally, the expected a posteriori estimate can also be determined. Evaluating the accuracy and precision of other estimators would widen the choice of estimators. We further note that EB-MAP can be applied to other FFS techniques, namely, scanning and imaging FCS, to improve accuracy and precision. These methods record the spatial distribution of fluorescence fluctuation, as with N&B analysis. Therefore, expecting a similarity between parameters at spatially close positions would be reasonable. The spatial similarity of parameters is typically not assumed if the parameters are estimated by analyzing the temporal fluctuation at a position. We demonstrated that assuming the spatial similarity of parameters is useful to effectively extract the information in fluorescence images.